

FULL-SCALE MEASUREMENTS AND SYSTEM IDENTIFICATION:

A TIME-FREQUENCY PERSPECTIVE

VOLUME II

A Dissertation

Submitted to the Graduate School
of the University of Notre Dame
in Partial Fulfillment of the Requirements
for the Degree of

Doctor of Philosophy

by

Tracy Lynn Kijewski-Correa, B.S.C.E., M.S.C.E.

Ahsan Kareem, Director

Department of Civil Engineering and Geological Sciences

Notre Dame, Indiana

April 2003

CONTENTS

VOLUME II

TABLES	xxxviii
FIGURES	xl
CHAPTER 9: OVERVIEW OF FULL-SCALE MONITORING PROGRAM	404
9.1 Introduction.....	404
9.2 The Need for Full-Scale Monitoring of Tall Buildings	405
9.2.1 Enhancing the Understanding of In-Situ Damping.....	406
9.2.2 Broader Impacts of Monitoring Program.....	408
9.3 Recent Full-Scale Monitoring Programs	409
9.4 Monitored Structures	412
9.4.1 Building 1.....	413
9.4.2 Building 2.....	413
9.4.3 Building 3.....	414
9.5 Primary Instrumentation System.....	414
9.5.1 Accelerometers	415
9.5.2 Data Loggers and Supporting Electronics	419
9.5.3 Installation and Placement	422
9.6 Anemometers	424
9.7 Data Transmission and Management.....	428
9.8 Example of Full-Scale Data	430
9.9 Summary	433
CHAPTER 10: INTRODUCTION TO GLOBAL POSITIONING SYSTEMS	434
10.1 Introduction.....	434
10.2 Origins of GPS Satellite Network.....	434
10.3 The GPS Concept.....	435
10.4 Anatomy of GPS Satellite Signals	438
10.5 Safeguards.....	442
10.6 Inherent GPS Errors and Corrective Configurations	442
10.6.1 Differential GPS (DGPS).....	443
10.6.2 Differential Phase Positioning	444

10.7 Residual GPS Errors	447
10.7.1 Dilution of Precision (DOP) Errors	448
10.7.2 Multi-Path Errors	451
10.8 Motivation for Structural Monitoring Applications.....	453
10.8.1 Recent Applications to Civil Engineering Structures	455
10.8.2 Insights from Previous Research	456
10.9 Summary	459

CHAPTER 11: OVERVIEW OF GLOBAL POSITIONING SYSTEM AND CALIBRATION TESTS.....

CHAPTER 11: OVERVIEW OF GLOBAL POSITIONING SYSTEM AND CALIBRATION TESTS.....	460
11.1 Introduction.....	460
11.2 GPS Components	460
11.2.1 GPS Receiver	461
11.2.2 GPS Antenna.....	462
11.2.3 Accuracy	463
11.2.4 GPS Hardware Configuration.....	464
11.2.5 Lightning Protection System.....	467
11.2.6 GPS Data Acquisition Software.....	469
11.3 Field Site for Experimental Validation	470
11.4 Test Configuration	470
11.5 Overview of Tests	474
11.5.1 Test 1a-c: Verification of Background Noise and Influence of Satellite Position	475
11.5.2 Test 2a-w: Verification of Amplitude Sensitivity.....	476
11.5.3 Test 3a-f: Verification of Ability to Track Complex Signals	477
11.5.4 Test 4a-c: Influence of Gas Capsule	479
11.5.5 Test 5: Coordinate Transformation Mock-Up	480
11.5.6 Test 6a-b: Influence of Antenna Mount.....	482
11.6 Post-Processing Protocol	483
11.6.1 Cutoff Angle	484
11.6.2 Baseline Limit.....	485
11.6.3 RMS Threshold.....	485
11.6.4 Solution Type.....	486
11.6.5 Ionospheric Modeling	486
11.6.6 Stochastic Modeling.....	488
11.6.7 Tropospheric Modeling.....	488
11.6.8 Single Point Processing.....	489
11.7 Interpretation of Results.....	490
11.8 Summary	491

CHAPTER 12: GLOBAL POSITIONING SYSTEM CALIBRATION TEST RESULTS AND DISCUSSION

CHAPTER 12: GLOBAL POSITIONING SYSTEM CALIBRATION TEST RESULTS AND DISCUSSION	492
12.1 Introduction.....	492
12.2 Verification of Background Noise and Influence of Satellite Position: Results.....	492

12.2.1 Probability and Spectral Structure of Background Noise	496
12.2.2 Additional Information from Static Component of Dynamic Tests	500
12.3 Accuracy Estimates.....	502
12.4 Data Preparation.....	508
12.5 Analysis of Dynamic Calibration Tests	510
12.5.1 Test 2a-w: Verification of Amplitude Sensitivity.....	513
12.5.2 Test 3a-3f: Verification of Ability to Track Complex Signals	523
12.6 Test 4a-c: Influence of Gas Capsule	531
12.7 Test 5: Coordinate Transformation Mock-Up	539
12.8 Test 6a-b: Influence of Antenna Mount.....	541
12.9 Recommendations for Full-Scale Application.....	545
CHAPTER 13: GPS MONITORING IN URBAN ENVIRONMENTS: DATA	
MINING AND INFORMATION PROCESSING.....	548
13.1 Introduction.....	548
13.2 Identification of Reference Site	548
13.3 Installation of GPS Components in Full-Scale	549
13.3.1 Antenna Mounts.....	549
13.3.2 Grounding	552
13.3.3 Receiver Cabinetry.....	553
13.4 Monitoring Program.....	554
13.4.1 Modifications to the Post-Processing Routine	557
13.4.2 Preliminary Baseline Position.....	558
13.5 Radio Frequency Interference.....	562
13.6 Multi-Path Interference and Identification.....	563
13.7 Assessment of System Performance in Full-Scale.....	574
CHAPTER 14: CONCLUSIONS AND FUTURE DIRECTIONS	576
14.1 Contributions of This Work.....	576
14.1.1 Wavelet Analysis Framework and Application to Civil	
Engineering Signals	577
14.1.2 Wavelet Analogs to Hilbert Spectral Analysis	578
14.1.3 Introduction of Full-Scale Monitoring and Advanced	
Instrumentation: Global Positioning Systems.....	579
14.1.4 Evaluation and Treatment of Uncertainty in Damping Estimation	
from Ambient Vibration Data.....	580
14.2 Future Directions	581
14.2.1 Extension of Framework to Other Wavelets.....	581
14.2.2 Enhancing Ridge Extraction Abilities	582
14.2.3 Window Separation.....	583
14.2.4 Enhancement of GPS Sensing Technologies.....	584
APPENDIX: OVERVIEW OF RESAMPLING THEORY: THE BOOTSTRAP	586
A.1 Motivation.....	586

A.2 Bootstrap Theory.....	587
A.3 Bootstrapping to Estimate Variance in RDS and PSD	588
WORKS CITED	593

TABLES

VOLUME II

9.1	Summary of accelerometer properties considered.....	417
9.2	Specifications of ultrasonic anemometer with heater	427
9.3	Specifications of interim wind sensor.....	428
10.1	Multiplication factors to generate coherent signals from P-code	441
10.2	Summary of inherent errors in GPS and proposed solutions.....	454
11.1	Accuracy levels for Leica RTK GPS	464
11.2	Environmental constraints on GPS equipment	466
11.3	Overview of calibration tests	478
12.1	Satellite conditions and DOP errors for static tests	493
12.2	Statistics of GPS static displacements	495
12.3	Comparison of 99.7th percentile confidence limits of GPS background noise with those of Gaussian distribution.....	499
12.4	Statistics of E-W (static) direction in dynamic tests.....	501
12.5	Standard deviation of GPS static displacements compared to average of standard deviation in GPS displacement estimate	504
12.6	Chebyshev filter cut-off frequencies.....	510
12.7	Statistics of σ_N and mean noise threshold.....	512
12.8	Accuracy of GPS tracking for Test 2.....	514
12.9	Accuracy of GPS tracking for Test 3.....	524
12.10	Statistics of GPS displacement estimates and associated errors for Test 4a-c.....	535

12.11	Estimates of motion along shifted axis for Test 5.....	541
12.12	Statistics of GPS displacement estimates and associated errors for Test 6	543
13.1	Monitored dates of interest	558
13.2	Preliminary baseline position determination	561

FIGURES

VOLUME II

9.1	Primary instrumentation system for full-scale monitoring program.....	415
9.2	Operational range of Wilcoxon sensor (courtesy of Wilcoxon).....	418
9.3	Columbia accelerometer (left) and accelerometer pair in enclosure ready for mounting.....	420
9.4	Data logger cabinet assembly installed in Building 1 (zoomed in for detail) and comparable logger assembly for Building 2 (inset at right)	421
9.5	Positions of accelerometers (1, 2) and data loggers (3) in Building 1 and Building 2.....	423
9.6	Mounted accelerometer housing in Building 1 (left) and Building 2.....	423
9.7	Photo of Viasala ultrasonic anemometer	426
9.8	Accelerometer data from Building 1 on 11/30/02 from 1:00 to 2:00: (a) alongwind component; (b) acrosswind component; (c) torsion-induced alongwind component at corner; (d) torsion-induced acrosswind component at corner.....	431
9.9	Fourier power spectra of accelerometer data from Building 1 on 11/30/02 from 1:00 to 2:00: (a) alongwind component; (b) acrosswind component; (c) torsion-induced alongwind component at corner; (d) torsion-induced acrosswind component at corner.....	432
10.1	GPS strategy for determining position.....	437
10.2	Relation of position in WGS84 coordinate system to latitude and longitude on Earth's surface (taken from Leica, 1999)	437
10.3	Schematic representation of GPS satellite signal structure.....	440
10.4	Schematic of elevation and azimuth measures for a GPS satellite at 135°azimuth and 60° elevation.....	449

10.5	Schematic representation of satellite configurations leading to low DOP (left) and high DOP (adapted from Leica, 1999).....	450
10.6	Errors in differential phase data manifesting long-period multi-path errors (taken from Axelrad et al., 1996)	453
11.1	Choke ring antenna (top, left), outfitted with protective dome covering (top, right) and GPS receiver (bottom)	462
11.2	Configuration of GPS data acquisition system installed in each building.....	466
11.3	Huber + Suhner lighting protector with gas capsule.....	468
11.4	Demonstration of 15° mask angle requirement limiting neighboring obstructions.....	471
11.5	GPS reference and rover antennas affixed to rigid mounts	472
11.6	Orientation of reference and rover station for Tests 1-4.....	473
11.7	Views in each direction of test site	474
11.8	Predicted availability of satellites and dilution of precision for Anderson Road site on January 22, 2002 (screen capture from Leica software)	476
11.9	Predicted availability of satellites and dilution of precision for Anderson Road site on April 17, 2002 (screen capture from Leica software)	480
11.10	Photo of gas capsule assembly I in Test 4a.....	481
11.11	Orientation of reference and rover stations for Tests 5-6	483
11.12	Sample SKI-Pro output (screen capture from Leica software).....	491
12.1	Portion of time history of GPS relative displacement for static tests Test 1b and Test 1c	495
12.2	Results from static tests and comparisons between observed RMS displacement (inner box) and manufacturer's prediction (outer box)	497
12.3	Probability density (compared to Gaussian function with same mean and standard deviation) with vertical bars denoting 1, 2 and 3 standard deviations of the mean, and power spectral density for each of the static tests in Test 1 series, E-W component.....	498
12.4	Probability density (compared to Gaussian function with same mean and standard deviation) with vertical bars denoting 1, 2 and 3 standard	

	deviations of the mean, and power spectral density for each of the static tests in Test 1 series, N-S component	499
12.5	Standard deviation of background noise along E-W direction, (static) for all tests, as a function of GDOP	502
12.6	Spectral structure of position quality measure for Test 1a and Test 2v, along with probability distribution for Test 1a	506
12.7	Average position quality as a function of GDOP	507
12.8	Examples of noise threshold levels (dotted) [cm] superimposed on GPS displacements [cm] for a series of static and dynamic tests	508
12.9	(a) Test 2a GPS displacement data; (b) Test 2a GPS displacement data after low-pass filtering; (c) Test 2e GPS displacement data; (d) Test 2e GPS displacement data after low-pass filtering	509
12.10	(a) PSD of Test 2a GPS displacement data; (b) PSD of Test 2a GPS displacement data after low-pass filtering; (c) PSD of Test 2e GPS displacement data; (d) PSD of Test 2e GPS displacement data after low-pass filtering	511
12.11	Comparison of shake table displacement (red) to GPS displacement estimate for Tests 2a-2f, mean noise threshold shaded in red	516
12.12	Comparison of shake table displacement (red) to GPS displacement estimate for Tests 2g-2l, mean noise threshold shaded in red	518
12.13	Comparison of shake table displacement (red) to GPS displacement estimate for Tests 2m-2r, mean noise threshold shaded in red	520
12.14	Comparison of shake table displacement (red) to GPS displacement estimate for Tests 2s-2w, mean noise threshold shaded in red	522
12.15	Comparison of shake table displacement (red) to GPS displacement estimate for Test 3a at various intervals in the test, mean noise threshold shaded in red	526
12.16	Comparison of shake table displacement (red) to GPS displacement estimate for Test 3b at various intervals in the test, mean noise threshold shaded in red	527
12.17	Comparison of shake table displacement (red) to GPS displacement estimate for Test 3c over the duration of the test (top) and zooming in at various intervals in the test, mean noise threshold shaded in blue	528

12.18	Comparison of shake table displacement (red) to GPS displacement estimate for Test 3d over the duration of the test (top) and zooming in at various intervals in the test, mean noise threshold shaded in blue	530
12.19	Comparison of shake table displacement (red) to GPS displacement estimate for Test 3e over the duration of the test (top) and zooming in at various intervals in the test, mean noise threshold shaded in blue	532
12.20	Comparison of shake table displacement (red) to GPS displacement estimate for Test 3f over the duration of the test (top) and zooming in at various intervals in the test, mean noise threshold shaded in blue	533
12.21	GPS displacements estimated during Tests 4a-c (left) and standard deviation of GPS displacement estimate.....	536
12.22a	Time histories of Test 4a-c GPS East-West displacement predictions and standard deviation of GPS displacement estimate	537
12.22b	Time histories of Test 4a-c GPS North-South displacement predictions and standard deviation of GPS displacement estimate	538
12.23	Generalized orientation of reference and rover stations for Test 5.....	540
12.24	Comparison of actual table displacement (red) and transformed GPS displacement estimates along E-W and N-S axes, using transformation angle of 45° and 50°	542
12.25	GPS displacement estimates for Test 6a-b and standard deviations of GPS displacement estimate.....	544
13.1	Reference and rover antenna mounts fabricated for full-scale application.....	551
13.2	Schematic of GPS antenna placement on rooftop frame of Building 1	552
13.3	Fully installed GPS antennas at Building 1/rover site (left) and reference site	553
13.4	In-line lightning protection with grounding wire (left) and installed in full-scale at reference site	554
13.5	Zoom of GPS cabinetry contents installed in full-scale program.....	555
13.6	GPS Instrumentation cabinet in place at reference site (left) and at rover site just below data logger cabinet in Building 1	556
13.7	Preliminary baseline position from monitoring on 11/14/2002 and comparison with displaced position on 11/13/2002.....	561

13.8	Fourier power spectra of relative displacements to the (a) north and (b) east: original data in black, filtered data in gray	566
13.9	Filtered displacement data for 11/30/02	567
13.10	Resonant displacement data for 11/30/02 with error thresholds (green)	568
13.11	Zoom of resonant displacement data for 11/30/02	569
13.12	East and north relative displacements on consecutive sidereal days (data for 1/08/03 has been shifted 4 minutes).....	571
13.13	Quasi-static east and north relative displacements on consecutive sidereal days (data for 1/08/03 has been shifted 4 minutes)	572
13.14	Resonant east and north relative displacements on consecutive sidereal days (data for 1/08/03 has been shifted 4 minutes).....	573
A.1	Schematic diagram of generalized bootstrap concept (adapted from Efron & Tibshirani, 1993).....	588
A.2	Bootstrapping scheme for system identification.....	590
A.3	Variance envelopes for (a) RDT and (b) PSD. Grey lines indicate variance envelope; black line indicates traditional RDT and PSD estimate; dotted lines indicate RDS decay and HPBW	591

CHAPTER 9

OVERVIEW OF FULL-SCALE MONITORING PROGRAM

9.1 Introduction

While the wavelet analysis tools introduced in Chapters 3-8 provide a very attractive analysis framework for a variety of Civil Engineering signals, these mean little in the identification of system characteristics without meaningful, reliable response data as input to the analysis. While scaled experiments are often useful, they are at times incapable of capturing the underlying characteristics of structural response and potential nonlinearities. The best venue for obtaining data completely representative of actual structural response is obviously in full-scale, particularly in light of the need to better understand tall building response and the illusive damping parameter discussed in Chapter 2. This chapter overviews the current trends in full-scale monitoring of tall buildings under winds, introduces an on-going, collaborative monitoring program developed as a component of this dissertation, and overviews the selection and installation of sensors for this study. It should be noted that this effort combines the resources and expertise of researchers at the University of Notre Dame with those of leading designers at Skidmore Owings and Merrill (SOM) in Chicago and the Boundary Layer Wind Tunnel Laboratory (BLWTL) at the University of Western Ontario, a

respected wind tunnel testing facility. This latter group is simultaneously overseeing the wind tunnel testing in the program and also assisted in assembling. SOM, while serving as a liaison with the building management, is conducting structural analyses and sensitivity studies for each of the monitored buildings. The team at Notre Dame in addition to coordinating this effort, was responsible for sensor and data acquisition system selection, GPS development (addressed in Chapters 10-13), ongoing data analysis and management through Internet technologies and comparison of wind tunnel data and design response estimates and full scale observations. The findings of this program will aid in evaluating the ability of current design practice in realistically predicting the performance of these structures.

9.2 The Need for Full-Scale Monitoring of Tall Buildings

Even though the performance of tall buildings affects the safety and comfort of a large number of people in both home and work environments, tall buildings are one of the few constructed facilities whose design relies solely upon analytical and scaled models, which, though based upon fundamental mechanics and years of research and experience, has yet to be systematically validated in full-scale. Understandably, since the development of full-scale models is not feasible, monitoring the performance of actual structures becomes paramount and must be undertaken following construction as a means for verification and improvement of current design practices and analytical models. Further, as high-rise dwellings gain more prominence worldwide, their impacts upon the global society and economy will become more pronounced, necessitating a new frontier

in tall building design fully equipped to address the emerging issues of performance, economy and efficiency.

As a result, this ongoing program forms a necessary bridge between the predicted response of structures, both via analyses performed as part of the design process and wind tunnel testing, with measured response. Not only will this give valuable insight into the design community's current ability to estimate the dynamic properties and response of a structure under the action of wind loads, but it will also uncover areas of deficiency and suggest modifications to current design approaches. The results of this effort will also provide much needed evaluation of the performance of common structural systems for tall buildings in real wind environments, identifying their mechanisms of energy dissipation and the dependence of damping upon response amplitude.

9.2.1 Enhancing the Understanding of In-Situ Damping

In order to limit the response of tall buildings under the action of wind, lateral stiffness may be increased, which will decrease the amplitude of the displacements, though it may not significantly affect the accelerations, which are the stimulus for motion perception. Furthermore, by stiffening the structure, the jerk component, or rate of change of acceleration, which is a contributing factor to the motion stimulus, may actually increase (Kareem, 1992). Thus, increasing stiffness alone may not be sufficient to insure the structure satisfies both serviceability and habitability criteria. However, by increasing the level of inherent damping, the acceleration response of the structure will be decreased. Unfortunately, inherent damping cannot be as easily engineered in a structure as mass and stiffness, since its mechanisms are complex and, as of yet, not fully understood. This

stems from the fact that, while inherent damping proves to be a governing parameter in limiting structural response, it still cannot be reliably estimated in the design stage, as discussed in Chapter 2, and its values are typically assumed based on limited apocryphal data in order to complete analyses. The uncertainty surrounding this parameter has motivated researchers to study its levels further using full-scale data.

Efforts to extract full-scale damping estimates have been undertaken by several investigators. A sampling of such studies can be found in Yokoo & Akiyama (1972), Trifunac (1972), Hart & Vasudevan (1975), Raggett (1975), Taoka et al. (1975), Hudson (1977), Jeary & Ellis (1981) and Celebi & Safak (1991). Information available from full-scale experiments has been assembled by Yokoo & Akiyama (1972), Haviland (1976), Jeary & Ellis (1981), Davenport & Hill-Carroll (1986), Jeary (1986), Lagomarsino (1993), and Tamura et al. (1994), among others. While these are important contributions to the better understanding of in-situ damping levels, these studies are strongly focused on mid-rise structures. As a result, there is a serious scarcity of data for high-rise buildings that are taller than 20 stories. More importantly, it is above this height that the wind-excited motions are dominated by the resonant response, which is strongly influenced by damping. In Davenport & Hill-Carroll (1986), a summary of damping estimates versus amplitudes clearly demonstrates the scarcity of available data. A similar lack of information exists in the data set reported by Lagomarsino (1993) for buildings with periods larger than 3 seconds. Jeary (1986) very carefully scrutinized this damping database and eliminated a majority of the measured damping data due to concerns such as a lack of documentation and an absence of variance errors and confidence intervals. This reiterates the concerns that the system identification performed on this existing data has

questionable reliability (see discussions in Chapter 2). The remaining database, which was used for developing the model, was again biased toward mid-rise buildings, with the exception of the Transamerica building, and displayed a significant level of scatter. This scatter is particularly concerning, as these estimated design values may provide damping estimates with a standard deviation of up to 70%, resulting in significant inaccuracies in the resulting response quantities, which are vital to guarantee that the structure satisfies occupant comfort criteria, particularly in the case of tall buildings.

Thus it is essential to expand this database to span the gamut of structural systems, materials, heights and foundation types representative of modern construction and under the action of wind loads of varying recurrence intervals. Further, considering the limitations and challenges associated with the estimation of damping, a considerable scatter has been observed in the data collected from these earlier studies, which can be remedied in the context of new and evolving system identification techniques and by accounting for the amplitude dependence of this parameter (Jeary, 1996). These discussions highlight the level of uncertainty that still remains in the design of one of the largest and most challenging products in society and the need for monitoring programs for tall buildings to provide some reliable measure of in-situ damping at a variety of amplitude levels.

9.2.2 Broader Impacts of Monitoring Program

Perhaps most importantly, this project will dispel the misconceptions and reservations which previously precluded full-scale monitoring of buildings in the United States, reassuring owners and occupants that the presence of monitoring devices in a structure is

not indicative of a troubled building, but rather is representative of a commitment on the parts of owners and the engineering community to improve the understanding of structures and thereby techniques for their design, thus improving the habitability of the built environment. It is only through such a commitment to full-scale monitoring and validation that the standards for high-rise construction can advance, resulting in more efficient, reliable designs and assuring the competitive edge for the US in high-rise developments, all the while fostering an environment conducive to the promotion of health monitoring initiatives.

9.3 Recent Full-Scale Monitoring Programs

Interestingly, this validation process has received a significant deal of attention in Japan and a host of full-scale monitoring programs have been initiated, particularly during the 1970's, concerned primarily with the measurement of pressures on building facades (Kanda & Ohkuma, 1990). An examination of most of the full-scale data being collected in Japan has resulted in a database of the dynamic properties of numerous buildings (Tamura, 1998). The database consists of high-quality, full-scale damping data on 268 buildings under various conditions from nearly 40 organizations, and literature reports since the 1970's. As more full-scale data becomes available, the database will be expanded. For example, some full-scale monitoring is currently underway for tall buildings in Hong Kong that has produced some additional information on in-situ damping levels (e.g. Li et al., 1998).

Much of the current full-scale monitoring projects in Japan are in conjunction with the design and/or validation of auxiliary damping devices (Kareem et al., 1999).

Such studies typically span several years, allowing for the observation of a few major wind events and earthquakes. As these studies are interested in validation of devices that have been installed, in the case of wind response control, to improve habitability, wind speed and direction and building accelerations are typically of interest, as well as damper properties such as stroke and displacement. Projects of this nature include the observations of the Sendagaya INTES building in Tokyo following the world's first application of an active mass damper (Yamamoto et al., 1998), the Riverside Sumida Building (Inaba et al. 1998), the Chiba Port Tower (Kitamura et al., 1988), the Shinjuku Park Tower (Koike et al., 1998), and the Hamamatsu ACT Tower (Miyashita et al., 1998). Since all of these studies have particular interest in validating the performance of a damper, triggering mechanisms are employed to record the response under significant events such as typhoons and earthquakes. Still, these studies are not concerned with the validation of structural design techniques or establishing inherent levels of structural damping, but rather with the confirmation of predicted response reduction for the modified structure. However, isolated comparisons between predicted response quantities and observed full-scale data have been undertaken by other authors (e.g. Evans & Lee, 1981; Littler, 1991). In addition, some limited work in Japan has used full-scale data from tall buildings in conjunction with occupant surveys to validate existing occupant comfort criteria (Ohkuma, 1996; Ohkuma et al., 1991). Instrumentation programs have also followed to monitor the response of one of China's tallest buildings, the Di Wang Building (Xu & Zhan, 2001). Unfortunately, there have been limited efforts to undertake similar investigations in North America, though the US efforts directed toward repairing and maintaining its aging infrastructure has advanced the fields of nondestructive testing

and condition assessment. Still, as in the case of tall buildings, few full-scale bridge studies actually seek to validate wind designs in light of in-situ data (Delaunay et al., 1999).

Despite the numerous health monitoring projects involving bridges in the United States, the initiative has not been fully extended to buildings, though promising efforts are developing for the case of low-rise construction for the quantification of local pressures (e.g. Wu et al., 1999) and overall frame loading. This has resulted in some validation of wind tunnel models based on acquired full-scale data (Surry, 1991; Tieleman et al., 1996). In addition, recent full-scale instrumentation of a residential unit has provided information on both pressures and strains under the action of hurricane-force winds (Porterfield & Jones, 1999). However, in the case of high-rise construction there have been limited full-scale monitoring projects, typically undertaken following suspect structural behavior. Although there have been some noteworthy full-scale monitoring projects (e.g. Hansen et al., 1979; Durgin & Hansen 1987; Durgin et al., 1990; Isyumov et al., 1984), the circumstances surrounding many of these studies prohibited the academic community's access to the measured data. As most of these studies were initiated as investigations on behalf of concerned building owners, there were no published correlations between predicted and observed behavior, leaving research in this area largely unfulfilled.

The ongoing monitoring program discussed in this chapter addresses deficiencies in these areas by correlating the actual performance of constructed buildings with predictions made during their design, thereby providing an important missing link

between predictions and actual behavior. A review of available literature on the subject indicates isolated instances of field measurements, usually uncorrelated with specific wind conditions. While state-of-the-art structural analyses and wind tunnel testing are advancing rapidly, the accuracy and validity of their results needs to be calibrated with respect to actual performance – a major objective of this program. The end result will be the first systematic validation of existing design practice for tall buildings in the US, followed by appropriate calibrations of existing wind tunnel and analytical models and modifications to current design practice, if necessary (Kijewski & Kareem, 1998; Solari & Kareem, 1998; Zhou et al., 2002). Furthermore, data from this project will contribute to existing international databases by providing valuable information on the dynamic characteristics of high-rise buildings over a range of amplitudes.

9.4 Monitored Structures

The monitoring program detailed in this chapter is focused on the instrumentation of three tall buildings in Chicago, in reasonable proximity, seeking to correlate the measured response characteristics of the buildings, under a wide range of wind environments, with predicted behavior. The buildings selected for this study represent a variety of typical structural systems employed in the design and construction of high-rise structures. Since a major component of the project was spent in building relationships with the building owners, engineers and legal advisors to allow access to the buildings and establish a working relationship for installation and maintenance of the equipment, their anonymity and privacy of the data must be assured to guarantee continued access for the life of the program. As a result, only limited details of the structures are provided herein and their

names are not disclosed. For the remainder of this dissertation, they will be referred to as Building 1, Building 2 and Building 3 and are among the tallest structures on the city's skyline and among the tallest of their respective types in the world.

9.4.1 Building 1

Building 1 relies on a steel tube comprised of the exterior columns and spandrel beams as its primary lateral load-resisting system, with additional stiffening elements. The lateral load of the structure is resisted primarily by cantilever action (80%) with frame action carrying the remainder of the load. This behavior is primarily a result of the diagonals insuring a near uniform distribution of load on the columns across the flange face, with very little shear lag. The structure features foundations of straight shaft reinforced concrete caissons to bedrock (CTBUH, 1995).

9.4.2 Building 2

Building 2 diversifies the material types in the program, as it is a concrete shear wall/outrigger system. Shear walls located near the core of the building provide lateral load-resistance. At two levels, the core is tied to the perimeter columns at two locations via reinforced concrete outrigger walls to control the wind drift and reduce overturning moment in the core shear walls. The structure's foundation utilizes reinforced concrete straight-shaft caissons extending to rock (CTBUH, 1995).

9.4.3 Building 3

The steel moment-connected, tubular system of Building 3 permits the structure to behave as a vertical cantilever fixed at the base to resist wind loads, with a skeleton comprised of a structural steel frame, pre-assembled in sections and bolted in place on site. Foundations for this structure are also comprised of straight shaft reinforced concrete caissons extending to bedrock (CTBUH, 1995).

9.5 Primary Instrumentation System

Each of the buildings is instrumented with the same primary instrumentation system, though in some of the buildings this is supplemented by additional sensors, e.g. global positioning systems. The primary instrumentation system, summarized in Figure 9.1, features four accelerometers to monitor the two fundamental sway modes and the fundamental torsional mode with the fourth serving as a back-up (Isyumov & Morrish, 1997). The data acquisition system for the buildings triggers automatically at a prescribed threshold indicative of significant motions of that structure to insure that noteworthy wind events are captured and recorded, meanwhile a log of ten-minute statistics of response is chronicled throughout. The data from this system is then uploaded to the World Wide Web for access by the geographically dispersed project team. Details of the components of this system are provided herein.

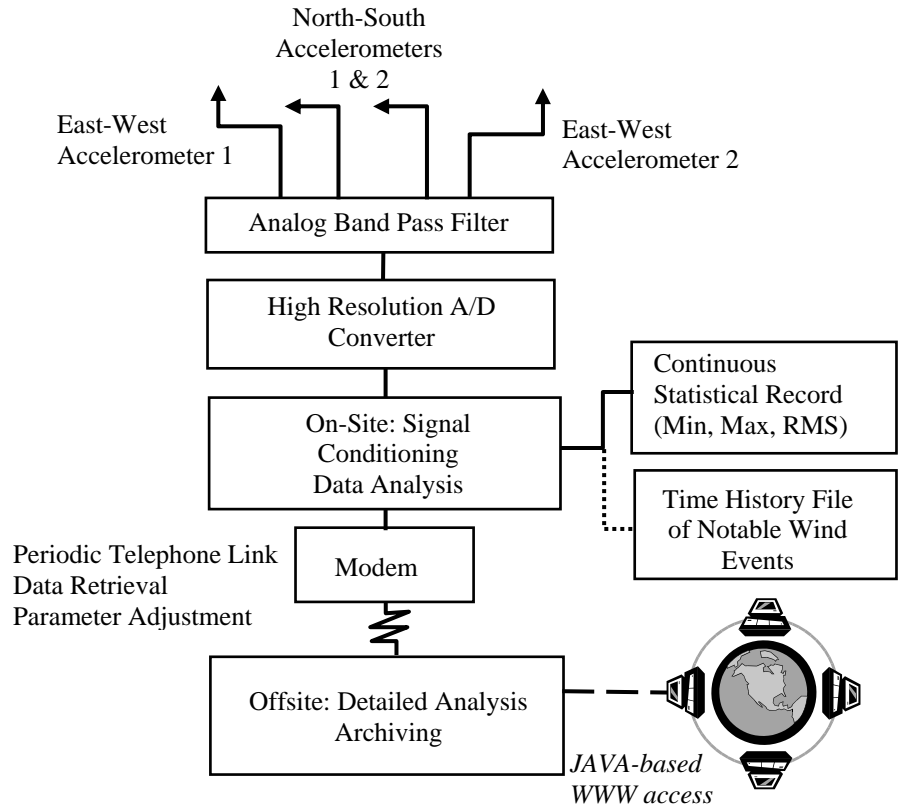


FIGURE 9.1. Primary instrumentation system for full-scale monitoring program

9.5.1 Accelerometers

Though a host of vendors were consulted for viable sensors, only a handful of those could generally meet the constraints of this application. These constraints arise from the fact that this project includes buildings that have fundamental frequencies in the range of 0.1-0.2 Hz, necessitating accelerometers capable of measuring responses from practically 0 Hz. Over the frequency range of interest, accelerations of 0-20 milli-g are expected and realistically nothing more than 50 milli-g is anticipated. Ideally, sensors with the highest

sensitivity possible are required considering the low levels of acceleration associated with wind-induced response. This sensor sensitivity is defined as

$$sensitivity = \frac{output \ voltage}{acceleration \ level}. \quad (9.1)$$

The noise level threshold becomes equally important in sensor selection, as it will dictate the minimal signal which can reasonable be discerned from noise. Assuming a desired signal to noise ratio of 10:1, an indication of the smallest signal discernable from noise can be determined according to

$$\min \text{ signal} = \frac{threshold \times 10}{sensitivity}. \quad (9.2)$$

These parameters, along with the frequency range of the sensors, were used in selection of accelerometers for the monitoring program. The sensors best meeting these constraints are summarized in Table 9.1.

The primary transducing system in most accelerometers is a spring-restrained seismic mass, however, the form of the secondary transducer, which converts the displacement and/or force associated with the seismic mass to an output voltage, varies. Two of the devices shown in Table 9.1 utilize a piezoelectric device for this purpose. The piezoelectric crystals (often quartz or ceramic) produce an electric charge when a force is exerted by the seismic mass under some acceleration. The quartz plates (two or more) are preloaded so that a positive or negative change in the applied force on the crystals results in a change in the electric charge. Though these devices have the ability to perform under a wide range of frequencies, they cannot provide a signal under static or pseudo-static

TABLE 9.1

SUMMARY OF ACCELEROMETER PROPERTIES CONSIDERED

Vendor	Model	Secondary Sensor Type	f_{\min} [Hz]	Sensitivity [V/g]	Min Signal [milli-g]
Kinometrics	EpiSensor	Servo	0	40	0.002
Columbia	SA-107LN	Servo	0	75	0.00013
Wilcoxon	731A	Piezoelectric	0.05 ¹	10	0.002
Industrial Monitoring Instrumentation (Div. of PCB)	626A04	Piezoelectric	0.03 ¹	10	0.005

¹Frequency response within +/- 3 dB. Sensor roll off initiates at 0.1 Hz.

conditions. In particular, the Wilcoxon model is a flexure-type piezoelectric accelerometer, with low-pass filter circuitry built in to protect the accelerometer from overload. This class of accelerometers' frequency response function (FRF) has a tendency to roll off at lower frequencies, as the low-end frequency performance is sacrificed to provide quicker recovery to changes such as a loss of power or overload. The operational range of this sensor is shown in Figure 9.2, noting the increase of the noise threshold of the sensor at the lower frequencies critical in this application. As the buildings in this study are unique, having periods much longer than most structures, their instrumentation must be unique as well, calling for sensors outside of what may be traditionally used.

This motivates the consideration of the servo class of accelerometers, where a position-sensing device detects the motion of the seismic mass and produces a signal that acts as the error signal in the closed-loop servo system. After the signal has been

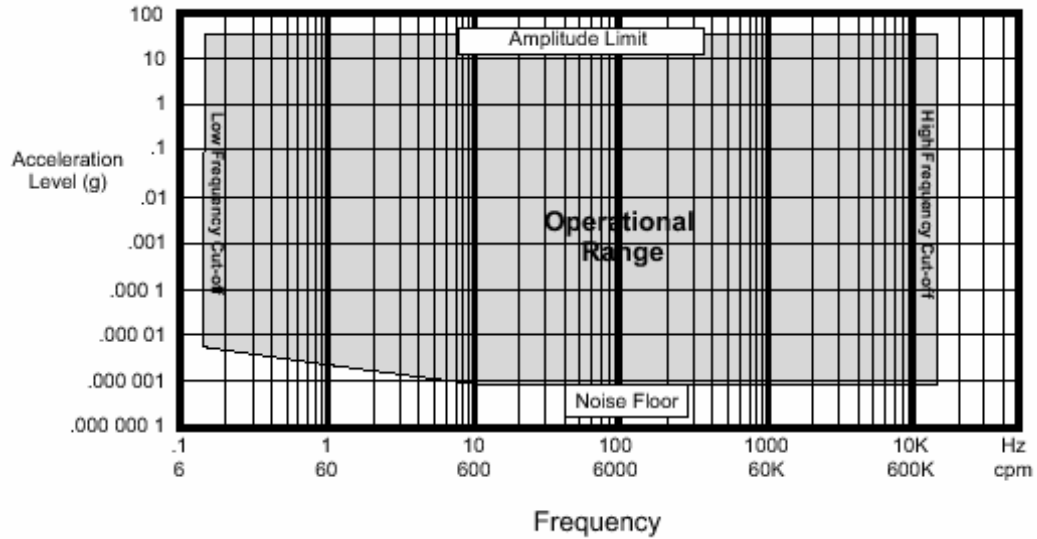


FIGURE 9.2. Operational range of Wilcoxon sensor (courtesy of Wilcoxon)

demodulated and amplified to remove the steady-state component, the signal is passed through a passive damping network and is applied to a torquing coil located at the mass's axis of rotation. The torque developed by the torquing coil is proportional to the current applied, and counteracts the torque acting on the seismic mass due to the acceleration, preventing further motion of the mass. Therefore, the current through the torquing coil is proportional to acceleration. Servo accelerometers provide high accuracy and a high-level output and can provide response measurements down to 0 Hz. In particular, the Columbia SA-107 LN force balance sensor was chosen for this application by virtue of ability to monitor low frequency acceleration measurements without compromising its noise threshold.

The selected Columbia sensor to its further credit has the highest available sensitivity of the sensors surveyed. The project team considered the Columbia sensors

with measurement ranges of ± 0.1 g and ± 0.5 g and ± 7.5 VDC output. It was decided to use the latter measurement range yielding a sensitivity of 15 V/g. Coupled with their ultra low-noise electronics, these high-level outputs certainly help to mitigate the noise associated with such low level, low frequency motion studies.

Understandably, internal displacements within any accelerometer will lead to inaccuracies and errors. This results from the fact that the sensing element must move some distance to produce a measurable change in output. However, force balance accelerometers limit these internal displacements to less than 1/10,000 of an inch, giving them the ability to minimize the static errors many traditional sensors experience. These drifts do surface to some extent, as the monitored data have thus far demonstrated in terms of mean acceleration components that are removed in the post-processing.

The Columbia accelerometer is shown in Figure 9.3. These accelerometers are mounted in pairs at two diagonal locations on the building floorplan to capture motion relative to the building's two perpendicular axes. The accelerometer pair, within its sealed mounting enclosure measuring 17 cm (W) x 15 cm (D) x 11 cm (H), is also shown in Figure 9.3.

9.5.2 Data Loggers and Supporting Electronics

Considering that supplementary sensor technologies in the form of anemometers and GPS units would be integrated into some of the monitoring systems, it was initially contemplated to use a data acquisition board and industrial computer. However, it was later decided to separate the GPS sensor, as discussed later in Chapter 11, and have all



FIGURE 9.3. Columbia accelerometer (left) and accelerometer pair in enclosure ready for mounting

other monitored data acquired by a data logger running on AC power. The selected logger was the Campbell CR23X-4M with internal 4 MB memory and external data storage modules adding another 16 MB of on-site storage capacity, providing 39 hours of data from the four accelerometer channels sampled every 0.12 seconds (at 8.33 Hz). The logger can accommodate up to 12 differential analog inputs with 15-bit resolution over five user-selectable voltage ranges, allowing the system to host the primary four accelerometers and accommodate future equipment expansions. For this application, the lowest voltage range, ± 10 mV, was selected. The overall resolution capabilities of the system are a function of the selected input voltage range and the number of bits in the A/D converter. According to the manufacturers, the resulting differential resolution is 0.00033 mV with accuracy of ± 0.01 mV under standard operating conditions. Considering the sensitivity of the accelerometers, this results in an overall system accuracy of 0.00133 milli-g. The logger system also has pulse-counting channels and digital input capabilities, which are important in the discussion of the anemometer sensor system in Section 9.6.



FIGURE 9.4. Data logger cabinet assembly installed in Building 1 (zoomed in for detail) and comparable logger assembly for Building 2 (inset at right)

The logger unit can be interfaced by a computer in the field through RS-232 connections to download data or upload changes to the logger software or data acquisition protocol. This interface can similarly be used to permit remote interrogation of the system through an industrial modem, which is the primary point of access to the system in this program. The data logger, the industrial modem, a rechargeable battery back-up system, 4 pole (20 dB octave) 1 Hz low pass, anti-alias filters and other supporting electronics for the accelerometers are all housed in a 61 cm (W) x 23 cm (D) x 61 cm (H), wall mounted metal enclosure shown in Figure 9.4.

9.5.3 Installation and Placement

Considerable interactions with the building representatives were necessary to arrange for a number of pre-installation site visits and the requisite support staff and equipment for installations. Particularly in light of the increased security in tall buildings after September 11th, additional considerations were required to permit installations in sensitive areas of the buildings, as well as in offices currently occupied by building tenants. Following these arrangements, the installation of the accelerometer units and data logger enclosures was completed on June 14 and 15, 2002 in Buildings 1 and 2, respectively. Installation efforts at Building 3 were being undertaken at the time this dissertation was submitted, in conjunction with plans for installation of a similar monitoring system in for a fourth tall building in Korea.

The accelerometer enclosures in Building 1 were clamped to exposed metal angles at the building's NE and SW corners, at approximately the ceiling level of its highest mechanical floor, essentially placing the sensors at roof level. The accelerometer enclosures in Building 2 were bolted directly to concrete spandrel beams within the suspended ceilings at that office level. Note the sensors were not mounted in a manner that would maximize the torsion arm along both building axes due to architectural and tenant restrictions. Building 2 is instrumented at the ceiling level on the second highest tenant floor, approximately three floors from roof level. This site was chosen due to superior cooperation afforded by the tenants occupying this floor. The positions of the accelerometer pairs are demarcated by the numbers 1 and 2 on the floorplans shown in Figure 9.5. Photos of their respective installation are shown in Figure 9.6.

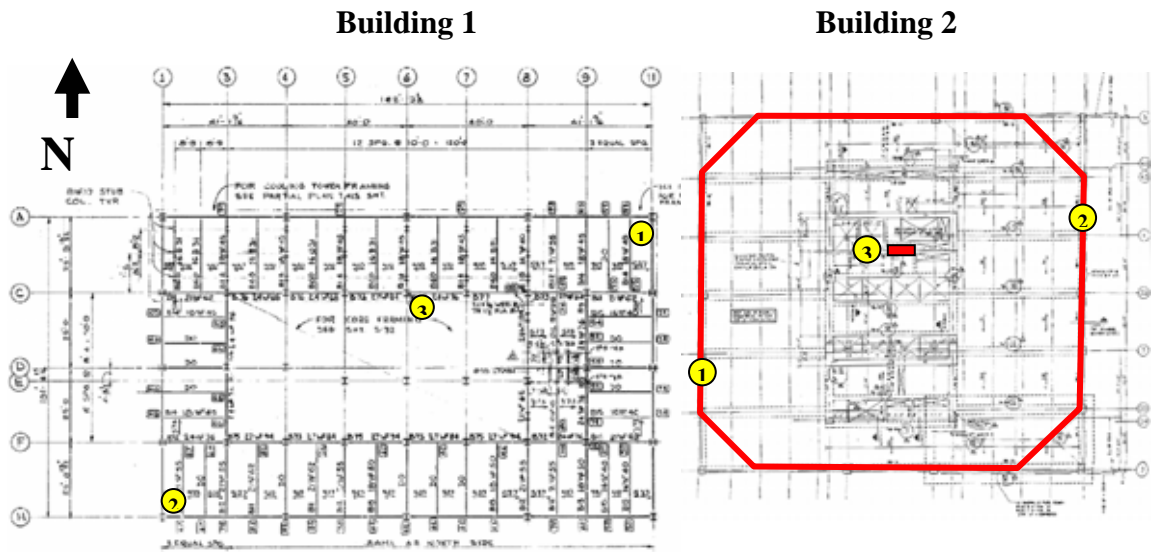


FIGURE 9.5. Positions of accelerometers (1, 2) and data loggers (3) in Building 1 and Building 2



FIGURE 9.6. Mounted accelerometer housing in Building 1 (left) and Building 2

In Building 1, the logger unit was wall-mounted near the cooling towers at a centralized position on the mechanical floor. In Building 2, the logger enclosure was wall mounted in a secured telephone closet near the elevator bank. These positions are shown by the number 3 in Figure 9.5.

The accelerometers are linked by twisted-pair, shielded instrumentation cable. As the installation in Building 1 is on mechanical floor, non-plenum cable was used and was fastened overhead to existing conduits. Out of concerns for fire safety Building 2, since the cable would be run inside a suspended ceiling of a tenant floor, a Plenum-rated cable, coated with fire-retardant Teflon, was used so that if a fire should reach the Plenum space, the cabling will not burn and give off toxic gasses and smoke. System operation was confirmed and official activation commenced on June 17, 2002, marking the beginning of the ongoing monitoring program.

9.6 Anemometers

While wind speed and directions are recorded at Chicago's surrounding airports, since wind-induced accelerations are typically proportional to the wind velocity cubed and uncertainties in wind speed are very much amplified by building response, it becomes essential to have a reliable measure of wind speed and direction in the downtown area. The team decided to establish a wind monitoring sensor pair atop the tallest building in the program, Building 3. The reference wind speed and direction for each event may be measured at this site and reliably converted to represent the wind speed at the full height of each of the instrumented buildings.

Both a heavy-duty propeller/vane and a sonic anemometer system were initially considered for this study. Due to its location, the anemometer selected had to be robust enough to withstand the harsh conditions at this elevation without requiring any repairs, as its installation point is not readily accessible. For this reason, an ultrasonic wind sensor by Vaisala was purchased, as it lacks any moving parts and does not suffer from minimum friction thresholds and delays of traditional propeller-type units. In the more traditional propeller units, the acceleration and deceleration of the moving parts is not instantaneous, leading to a delayed response which precludes reporting of wind speeds at higher sampling rates, e.g. wind speed is sampled every 10 seconds or more. In addition, moving parts have a tendency to wear with use, may become completely inoperable in icy conditions, and degrade in terms of performance in the presence of dust, salt and other pollutants. The sonic anemometers without the moving parts have accuracy that is inherently stable since it is dictated by the distance between its fixed sensors. These sensors rely on the propagation of the speed of sound between the transducer's three points, of known separation, to determine the speed and direction of the moving air mass. Since the physical construction of the sensor provides some obstacles to the airflow that modify the sensed velocity within the sample volume, the third transducer is required to serve as a redundant basis direction to perform validity checks on the velocity solutions estimated. This redundancy allows the sensor to "fill in holes created by turbulence at higher wind speeds," increasing the range of the sensor (Lockyer, 2000).

The unit's small size and fixed orientation allowed the inclusion of heaters at minimal power expense to limit the accumulation of ice and snow on the sensor, as shown in Figure 9.7. The specific properties of the ultrasonic wind sensor are provided in



FIGURE 9.7. Photo of Viasala ultrasonic anemometer

Table 9.2. Both measurements are acquired through the logger system discussed in Section 9.5.2, sampled in the same manner as the instrumentation framework in Figure 9.1, with 10-minute statistics logged throughout and continuous time histories captured during events triggered by the accelerometers.

It should finally be noted that lightning strikes to the sensors on the rooftop are of great concern, not only for the destruction of the sensor, but for the propagation of electrical surges down the instrumentation cable and to the logger enclosure where all the supporting electronics could also be destroyed. For this reason, the system is dually protected from surges through the appropriate grounding of the cabinetry and the inclusion of in-line surge protection. This latter form of lightning protection is discussed in Section 11.2.5. In addition, Building 3 employs streamer retardant structural lightning

TABLE 9.2

SPECIFICATIONS OF ULTRASONIC ANEMOMETER WITH HEATER

Wind Speed			Temperature Range
Range	Accuracy	Resolution	
0-144 mph ¹	±3% or 0.3 mph	0.1 mph	-67°F to 131°F
Wind Direction			Output Rate
Range	Accuracy	Resolution	
0° to 360°	±2°	1°	1 Hz

¹Using analog voltage or pulse: 0-125 mph.

protection to reduce the accumulation of static charge and retard the formation of lightning-completing streamers from the protected structure. This has greatly reduced the incidences of lightning strikes on the building's rooftop equipment.

An interim wind monitoring protocol was established while the final installation of the study's anemometer system is being coordinated at Building 3. This interim data is collected from a NOAA meteorological station in Lake Michigan, elevated 75 feet above lake level and located 3 miles offshore, directly north of downtown Chicago. The anemometer at this station is a Young 5103V, propeller-type sensor whose properties are listed in Table 9.3. A Campbell data logger (CR10X) similar to that described previously acquires data every 5 seconds and the averages the results over 5 minute intervals. The data is uploaded through an RF modem serving as a wireless IP and interrogated remotely using the same Campbell software as this study, discussed in Section 9.7. The statistics of wind speed and direction, as well as other meteorological data, is available for viewing online every 5 minutes at www.glerl.noaa.gov/metdata/chi, and ASCII files of the

TABLE 9.3

SPECIFICATIONS OF INTERIM WIND SENSOR

	Wind Speed		
Range	Accuracy	Resolution	Temperature Range
0-134 mph	0.67 mph	N/A	-58°F to 122°F
	Wind Direction		
Range	Accuracy	Resolution	Output Rate
0° to 360°	±3°	N/A	3 pulses/rev

monitored data for each calendar day from the current and previous year are archived for download at this site.

9.7 Data Transmission and Management

The data collected from at each logger are downloaded daily to the central data archiving computer housed at SOM offices in Chicago, minimizing phone expenses by using local calls to the modems at each site. The process of downloading the daily files is completely automated by PC 208W software from Campbell, which facilitates remote programming and operation of the logger. The use of commercial off-the-shelf software for a PC environment can greatly reduce the overall cost of a monitoring project. For these reasons, PC Anywhere is used for remote interrogation of this computer and to use this local hub to perform system checks of the instruments from the remote locations of the investigators at Notre Dame. The data is uploaded automatically from this computer through the Internet to an offsite FTP server where the data can be downloaded for further analysis and dissemination or merged with graphical user interfaces.

Internet technologies have emerged as promising solutions to the traditional challenges in large scale monitoring projects. Recent advancements not only facilitate the transmission of data from the remote computing stations to a host computer, but the emergence of Java-based applets (Ballard & Chen, 1997) now permit data retrieval and analysis by authorized users worldwide. Such secured access over the Internet becomes particularly attractive for the current project, as the data from the four instrumented buildings may be reviewed, downloaded, processed and analyzed with complete access to all applications on the host computer from any location by the research team at their respective locations worldwide. In particular, such use of Internet technologies and a simplified user interface facilitates the active involvement of building owners and management, as well. Since most users are already equipped with a working understanding of the Internet, as well as the appropriate hardware and software, internet-based monitoring becomes an inexpensive tool to facilitate long-term monitoring initiatives in the US. As a result, in this ongoing program, JAVA-based applets are being utilized to create graphical interfaces to view the acceleration time histories and measured wind speed and direction. These interfaces housed at the project website (www.nd.edu/~windycty) allow users equipped with the requisite username and password to select a given data file and view the sway and torsional acceleration time histories, wind speed and direction and relevant statistical measures. The development of these interfaces is discussed in greater detail in Kijewski et al. (2003).

9.8 Example of Full-Scale Data

The performance of the data acquisition system, discussed previously in the activities section, has been validated successfully through the collection of continuous time histories as well as 10-minute statistics for both Building 1 and Building 2. The data collected thus far affirm not only the performance of the data acquisition system but also the ability of the Columbia accelerometers to successfully capture low-amplitude, low-frequency response with minimal electronic noise. While the data processing and analysis associated with this larger full-scale investigation is the subject of on-going investigations by the project team, e.g. Kijewski et al. (2003), an excerpt of the data is shown here to give some indication of the resolution capabilities of the system. On this day winds were coming out of the north with a mean hourly wind speed of 24 mph, as measured by the NOAA sensor discussed in Section 9.6. Using a standard decoupling procedure, the sums and differences of the four accelerometers yields an estimate of the alongwind and acrosswind accelerations in sway, as well as the alongwind and acrosswind acceleration components associated with torsion at the corners of the building. These results are shown in Figure 9.8. Though one often expects acrosswind accelerations to dominate, since the acrosswind axis for this wind direction is stiffer than its alongwind counterpart, larger motions are detected in the alongwind data. The two torsional records are of varying amplitude, due to the fact that the torsional arm for the acrosswind component in Figure 9.8d is shorter. The sub-milli-g accuracy of the system is clearly demonstrated. Figure 9.9 provides the Fourier power spectra for the measured data. The extremely low frequencies of vibration become immediately apparent, as do the narrowbanded nature of the response. The alongwind response in Figure 9.9a is

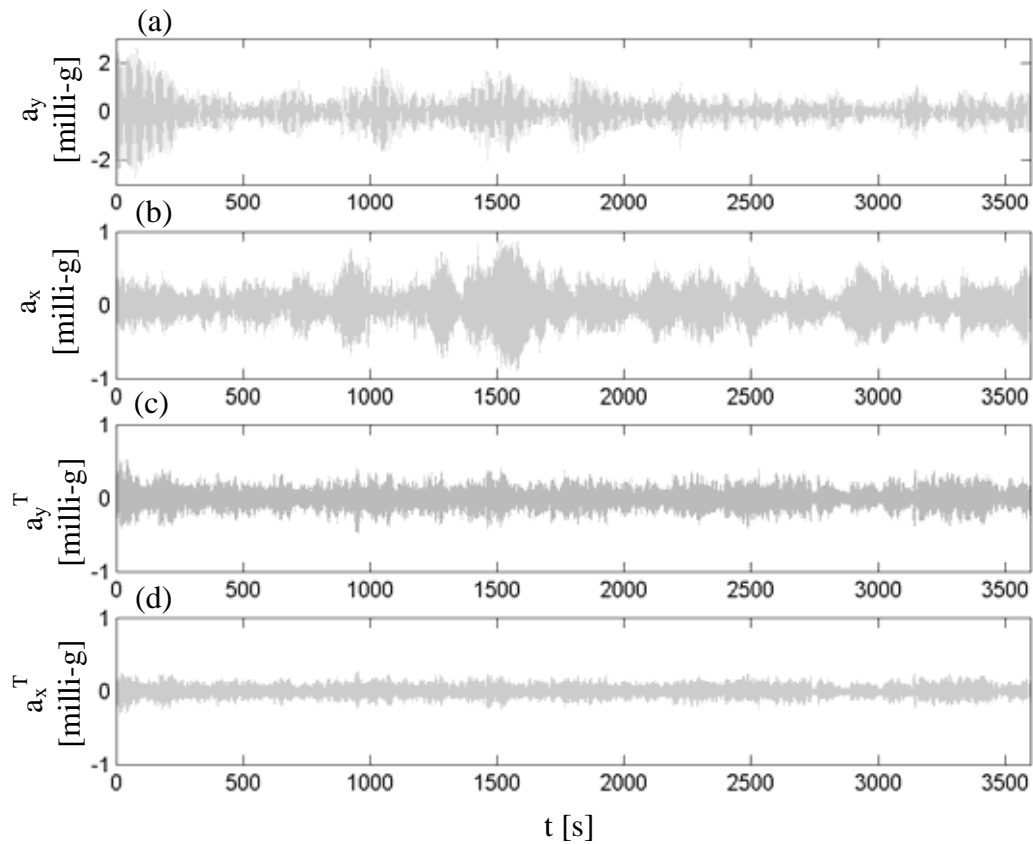


FIGURE 9.8. Accelerometer data from Building 1 on 11/30/02 from 1:00 to 2:00: (a) alongwind component; (b) crosswind component; (c) torsion-induced alongwind component at corner; (d) torsion-induced crosswind component at corner

characterized by a single sway mode at 0.143 Hz while the crosswind in Figure 9.9b is dominated by a single sway mode at 0.206 Hz and the trace of a higher sway mode at 0.568 Hz. The two torsional perspectives in Figures 9.9c and d demonstrate, in the jaggedness of the peaks, the difficulty in cleanly separating the torsional components by simple algebraic operations on the data. Still the fundamental torsional mode is identified in both at 0.505 Hz with higher modes present at 1.03 and 1.56 Hz. The agreement between the sensors in this regard affirms that the structure is responding in torsion uniformly over its plan.

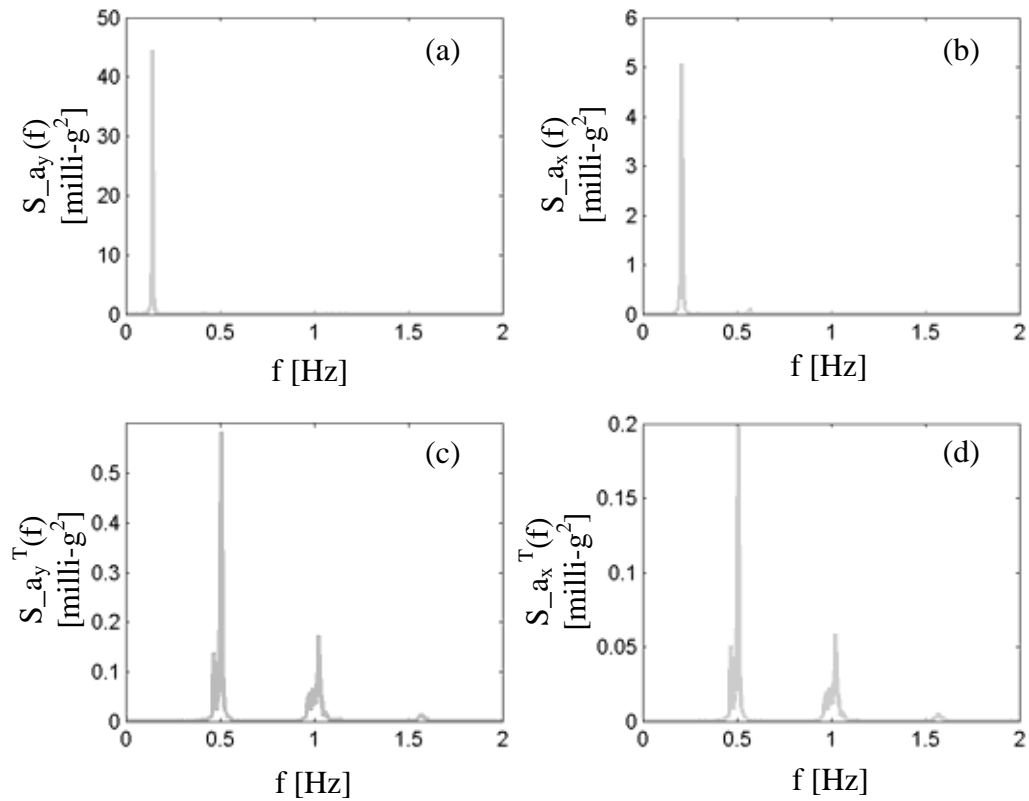


FIGURE 9.9. Fourier power spectra of accelerometer data from Building 1 on 11/30/02 from 1:00 to 2:00: (a) alongwind component; (b) acrosswind component; (c) torsion-induced alongwind component at corner; (d) torsion-induced acrosswind component at corner

Interestingly, wind-induced vibrations are not the only noteworthy responses detected by the sensors, as an unexplained spike in the 10-minute statistics of the response along the softer axis of Building 1 was ultimately traced to a magnitude 5.0 earthquake in southern Indiana near Evansville. This event, which was also felt in the Northern regions of the state, produced a minor excitation of this tall building in Chicago.

9.9 Summary

This chapter introduced a full-scale monitoring program in Chicago seeking to systematically validate the performance of tall buildings by comparing the observed response to the predictions from wind tunnel testing and analytic models developed in the design phase. The instrumentation systems employed in the three buildings in this study were overviewed: Building 2 features four accelerometers while Building 1 supplements the four accelerometer system with a high precision GPS sensor, which is the subject of Chapters 10-13. Building 3, whose instrumentation was being installed at the time of this dissertation's completion, will feature the four accelerometer package as well as a pair of rooftop anemometers. Through the program discussed herein, full-scale monitoring state-of-the-art is advanced via the development and introduction of advanced instrumentation systems, including GPS and automated data access and manipulation via a JAVA-based web interface, promoting the use of full-scale monitoring of tall buildings in the United States. Subsequent chapters will address further the development of the global positioning systems in this program, as they represent a relatively new technology for dynamic monitoring of Civil Engineering structures, particularly in urban environments.

CHAPTER 10

INTRODUCTION TO GLOBAL POSITIONING SYSTEMS

10.1 Introduction

Since the earliest journeys of man by land and sea, the heavens have served as the means by which positions were defined. Today, the rapid development of Global Positioning Systems (GPS) renews this ancient concept by providing a highly accurate and reliable means to determine exact positions on the earth's surface using a triangulation of satellites orbiting above (Leica, 1999). This chapter gives a historical overview of GPS and defines basic terminology and concepts relevant to discussions in subsequent chapters. More details on the theory of GPS positioning can be found in Seeber (1993). Inherent errors and their remedies also presented, followed by an overview of their applications for the monitoring of time-varying displacements in large Civil Engineering structures.

10.2 Origins of GPS Satellite Network

The global positioning network known as today's GPS was developed by the Department of Defense (DoD) to enable precise estimates of position, velocity and time in any

weather condition (Enge & Misra, 1999). The architecture was first approved in 1973, with the first satellite launched in 1978. By 1995, the entire system was fully operational; however, recognizing the potential threats to National Security, the government decided to limit the accuracy of GPS for civil users by introducing the Standard Positioning Service (SPS). In the meantime, military and authorized civilians were permitted to use the Precise Positioning Service (PPS) to obtain more accurate positioning information. Today the DoD continues to oversee both the space segment (satellites) and control segment (earthbound satellite control centers) of the GPS network for the benefit of the civilian user segment.

The network is comprised of 24 GPS satellites (actually approximately 30 satellites are currently in orbit, as older satellites are phased out and new replacements launched) in 6 orbital planes, each of the planes containing 4 satellites. Each satellite completes a single orbit of the earth in 12 hours, moving at 4 km/s. Spacing of satellites within these planes is intended to provide a minimum of 4-5 satellites orbiting at least 15° above the horizon at any location at all times, though 6-8 satellites are typically in view for most users.

10.3 The GPS Concept

GPS positions are calculated using the concept of triangulation, based on the known position of other objects to determine the desired unknown position. In this case, satellites serve as the known position points, much like the constellations that served the ancient sailors. Each satellite continuously transmits the current time, determined from their on-board atomic clocks, as well as information about their orbit. Each satellite's

distance to the unknown location on the face of the Earth, marked by a GPS receiver, is determined from the travel time of the transmitted electromagnetic signals, moving at the 290,000 km/s. A comparison of the time that the signal is received on Earth to the time when it was sent yields the *slant range* of the satellite. This concept is shown schematically in Figure 10.1. An equation for the slant range S_i of the i^{th} satellite in a constellation of N_{sat} satellites is simply given by

$$S_i = \sqrt{(x_i - x)^2 + (y_i - y)^2 + (z_i - z)^2} \quad i = 1, 2, \dots, N_{sat}. \quad (10.1)$$

This expression is a function of the satellite's position in orbit (x_i, y_i, z_i) , which is known, and the unknown position on earth (x, y, z) , defined in terms of the World Geodetic System 1984 (WGS84) coordinate system, which provides the position on the surface of an ellipsoid representative of the Earth. This position on this ellipsoid is defined in terms of a Cartesian coordinate system, yielding the distance along the x, y and z-axes from the origin of the spheroid, shown in Figure 10.2. As discussed later in Section 11.7, this position is projected onto a local coordinate system that defines a point on the Earth's surface in terms of the more familiar latitude, longitude and elevation or other local grid. Recall that since the slant range S_i can be determined for each satellite based on the signal's travel time, given a system of three satellites, a minimum of three equations ($N_{sat} \geq 3$) are required to solve for the three position unknowns on the face of the Earth.

However, this is an ideal scenario that requires very accurate timing and position information from the satellites in space. While the satellite position can be determined with sufficient accuracy, GPS technology is inherently constrained by the clocks upon which it is based. As radio waves travel one meter in 3 nanoseconds, accurate slant

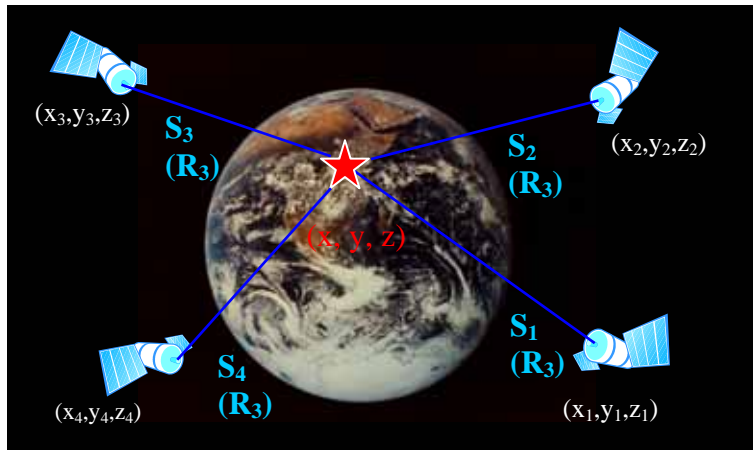


FIGURE 10.1. GPS strategy for determining position

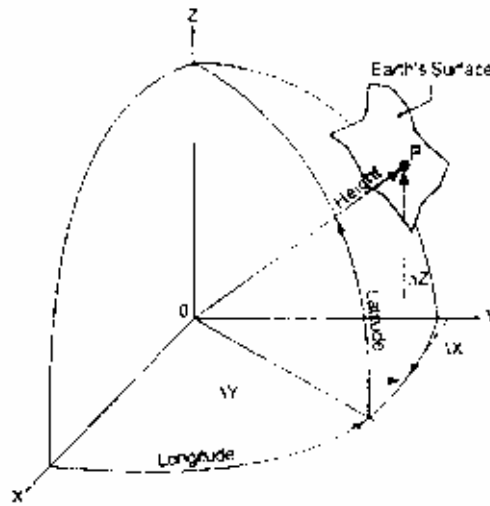


FIGURE 10.2. Relation of position in WGS84 coordinate system to latitude and longitude on Earth's surface (taken from Leica, 1999)

ranges can only be obtained if the time of day is known to the nanosecond. Understandably, atomic clocks are capable of providing this level of accuracy, however they are too expensive for civilian GPS receivers. Instead, less accurate quartz crystal clocks are used to determine *pseudoranges* based on an uncorrected time value. The inaccuracies introduced by this cost-effective technique can be corrected in subsequent calculations. To account for clock inaccuracies, the time bias b is then introduced into Equation 10.1, where slant range is replaced more appropriately by pseudorange, R_i , resulting in:

$$R_i = \sqrt{(x_i - x)^2 + (y_i - y)^2 + (z_i - z)^2} - b \quad i=1, 2, \dots N_{sat}. \quad (10.2)$$

Thus, the desired position of the GPS receiver (x, y, z) can be determined from the known position of N_{sat} satellites and pseudoranges estimated from the travel time of the transmitted signal, as long as $N \geq 4$. However, if only three satellites are available, the elevation z in Equation 10.2 can be assumed fixed, and a measure of latitude, longitude and time bias can still be achieved. It should also be noted that although each satellite has its own atomic clock, the time bias for all is the same as it is defined with respect to the same receiver clock. Typically, as more than four satellites are available, an over-determined set of equations can be generated using Equation 10.2 to obtain an even more accurate position for the receiver.

10.4 GPS Satellite Signals

GPS satellites transmit two carrier waves continuously at two L-band frequencies: 1.57542 GHz (L1) and 1.22760 GHz (L2). Just as in typical FM transmissions, the GPS

signal $s(t)$ possesses a carrier frequency f_{CR} as well as the modulating frequency $m(t)$ component carrying the actual message:

$$s(t) = \cos(2\pi(f_{CR}t + m(t))). \quad (10.3)$$

Each transmitted signal thus contains the carrier signal and the binary data message, as well as a *pseudo-random noise* (PRN) code.

The L1 carrier signal is actually modulated by two signals in quadrature, the Coarse/Acquisition or Clear/Acquisition (C/A) code and the Precision (P) code. Meanwhile, the L2 is also P-code modulated, in addition to carrying a navigation (Nav) message. A visualization of the transmitted GPS signals is shown in Figure 10.3. The Nav data is transmitted at 50 Hz and contains orbital elements, clock accuracy information, and time and satellite status. As the GPS time is kept within $1\mu\text{s}$ of Coordinated Universal Time (UTC) as defined by the master clock at the US Naval Observatory, the difference between the GPS satellite's clock and the master clock is included in this navigation message.

The C/A code transmits data at 1.023 MHz and provides the SPS available for use by all civilian receivers, with satellite horizontal position gauged to 100 m and vertical position to 156 m. Meanwhile, the PPS is sent at 10.23 MHz and provides a horizontal satellite positioning accuracy of 22 m and a vertical accuracy of 27.7 m. This translates to a general accuracy of about 10 cm in determining the position of the GPS receiver. Interestingly the atomic clocks on board the GPS satellites operate at a fundamental frequency of 10.23 MHz, which is used to generate all the transmitted signals including

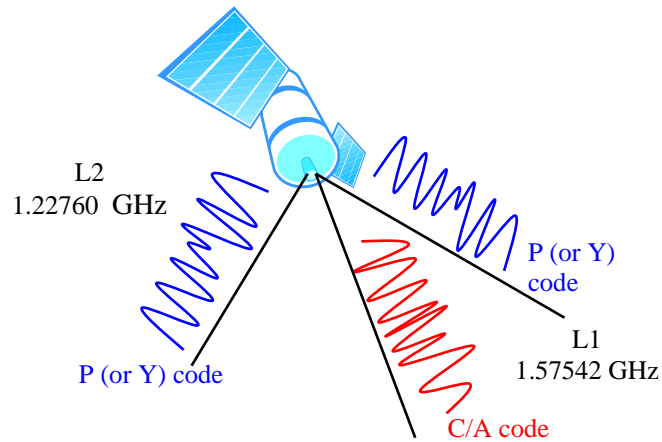


FIGURE 10.3. Schematic representation of GPS satellite signal structure

the P-code, the base for all GPS timing. As shown by Table 10.1, all the carrier frequencies and the C/A data transmission rate are multiples of the P-code frequency, generating *coherent signals*. In doing so, the number of unknowns in the equations is minimized.

The navigation signals (codes) carried on both of these frequencies are modulated based on the *spread spectrum* technique. As the name indicates, this approach spreads the signal content over a wide band with the spreading modulation based upon a PRN code. Although GPS signals have the same strength as TV signals, it is impractical to use the same large satellite dishes to receive the signals for the purposes of portable GPS units. Thus this spread spectrum modulation technique is used so that GPS signals can be detected using smaller antennas and pulled readily from the background noise. In radio signals, the modulation sidebands are hardly wider than the data they contain, so that each radio station transmission is concentrated at the center frequency of the carrier

TABLE 10.1

MULTIPLICATION FACTORS TO GENERATE COHERENT SIGNALS FROM P-CODE

P-Code Frequency*	Multiplication Factor	Resulting Frequency	
10.23 MHz	0.1	1.023 MHz	C/A Code
10.23 MHz	154	1575.42 MHz	L1
10.23 MHz	120	1227.60 MHz	L2
10.23 MHz	0.1	1.023 MHz	C/A Code
10.23 MHz	154	1575.42 MHz	L1

*Also fundamental frequency of atomic clock.

signal. In spread spectrum signals, the energy is purposely spread over a broad range of frequencies so that it is harder to detect and jam.

The spread spectrum signal can only be received if the receiver knows the spreading code ahead of time. The receiver, possessing the PRN code, generates a replica of the code in time. This signal is shifted in time until there is some correlation or synchronization with the satellite code. When the two signals line up slightly, some signal power is detected. When they line up completely, the spread-spectrum carrier signal is despread and the signal's full power is detected. The necessary time shift to obtain full correlation is a measure of signal travel time between the satellite and the receiver, and this is used to determine the pseudorange, as discussed in Section 10.6.2. This is called *code phase observation*. This use of phase is necessary for precise geodetic tracking because phase measurements have much better resolution (Seeber, 1993).

10.5 Safeguards

Understandably, the GPS satellite system is tremendously powerful. Its manipulation by terrorists groups or other enemies of the United States is of serious concern to the Department of Defense. Thus, certain safeguards have been implemented over the brief history of GPS to protect the network. As the C/A code is available to all users, the accuracy of the L1 carrier signal was purposefully degraded for National Security, limiting the receiver to the aforementioned 100 and 156 m under the 1990 Selective Availability (SA) policy. However, as the civilian demand for accurate GPS has grown, this Selective Availability policy is being phased out and should be completely eliminated by 2006 (Leica, 1999). Civilian manufacturers that currently offer P-code-grade accuracy must design their receivers to shutdown if the data processing moves above a certain speed, limiting its usefulness to the enemy. As an added protection to the user, an encrypted Y-code often replaces the P-code when anti-spoofing (AS) is desired. This 1994 AS policy calls for the encryption of the P-code to protect against fake transmissions of the satellite, which may be used to spoof the receiver.

10.6 Inherent GPS Errors and Corrective Configurations

The transmission of GPS signals over great distances leave this approach vulnerable to a variety of errors that can alter the rate of transmission and introduce errors into pseudorange estimates. These are primarily the result of atmospheric effects. The upper atmosphere or ionosphere is an envelope of electrically charged gas (plasma) that surrounds the Earth at altitudes between 70 and 1000 km above the Earth's surface. This atmospheric level can affect the time of receipt by slowing down the signal, thus

distorting pseudorange estimates. Further, as x-rays and UV solar radiation comprise the ionosphere, its effects increase during periods of high solar activity. The result can be a 0.15-50 m error in the pseudorange. Radio signals slow down as they pass through the ionosphere at a rate proportional to their frequency. Hence, if the arrival time of two signals of different frequencies is compared, an estimation of the ionospheric delay can be made. By using these *dual frequency* GPS units, which compare the delays between L1 and L2 signals, the ionospheric delays can be appropriately corrected. Modeling for this and other atmospheric effects is discussed later in Chapter 11. Meanwhile, the troposphere, the lower part of the atmosphere up to a height of about 40 kilometers, causes a delay in the propagation of electromagnetic waves such as those used in GPS. These delays amount to about 1 m and are due to changes in temperature, pressure and humidity during weather fluctuations. The presence of these errors limits the position accuracy of an *autonomous* or stand-alone GPS receiver to 20-100 m (Leica, 1999).

10.6.1 Differential GPS (DGPS)

It became evident that the use of two receivers, termed a reference and rover, could minimize some of the errors inherent to GPS. The reference station serves as a stationary checkpoint with a known position and constantly records the difference between its known position and the position calculated from the satellite data. The differences it detects are indicative of the errors from the satellite hardware and more importantly, lower atmospheric delays. To capture these errors, GPS receivers require adequate sampling rates, which have currently advanced to 10 Hz for some models. The rover, who is the GPS receiver whose position is being tracked, uses this error information to

improve its accuracy. The overall accuracy of DGPS (shown later in Table 11.2) is proportional to the *baseline*, or distance between the rover and the receiver, but in general arrives at errors of 0.5-5 m in determining a position on the face of the Earth (Leica, 1999). As the lower atmospheric errors tend to be the same within a limited spatial region, the reference station should be as close to the rover as possible, e.g. ideally less than a 10 km baseline separation.

10.6.2 Differential Phase Positioning

As mentioned in Section 10.6, ionospheric errors can be reconciled using the phase of the two carrier frequencies. Combining DGPS with this technique provides a way to increase the overall accuracy of the GPS, through so-called *Differential Phase Positioning*. A phase-based approach is used in this framework to determine the pseudorange. The use of carrier phase is far more accurate to measure the satellite pseudorange than the P-code or C/A code itself. As detailed in Leica (1999), the receiver determines a set of possible pseudoranges to each satellite by calculating the integer number of wavelengths in the carrier signal between the receiver and the satellite, a process called *ambiguity resolution* (Teague et al., 1995).

Though the process is discussed in further detail in Seeber (1993), some of the basic relations are provided herein. The observable in the process is the difference between the transmitted carrier phase $\phi_{CR}(T_t)$, which leaves the satellite at time T_t defined in the satellite time frame, and the phase of the reference signal $\Phi_0(t_r)$ it is being

compared to within the receiver, measured in the receiver time frame. The “observed” relative phase is defined as

$$\varphi_m(t_r) = \varphi_{CR}(T_t) - \Phi_0(t_r). \quad (10.4)$$

The carrier phase can be written as

$$\varphi_{CR}(T_t) = \varphi_m(t_r) + \Phi_0(t_r) = \varphi_m(t_r) + t_r f_0 \quad (10.5)$$

where f_0 is the reference signal frequency. When the carrier phase transmitted from the satellite is detected by the receiver at time t_r , the carrier phase is shifted by an integer number of cycles, as described by

$$\Phi_{CR}(T_t) = N_{cyc} \cdot 360^\circ + \varphi_{CR}(T_t) \quad (10.6)$$

with N_{cyc} as the integer ambiguity, the unknown number of complete wavelengths between the satellite and receiver. Since $\Phi_{CR}(T_t) = T_t f_{CR}$, an expression for the epoch of transmission of the carrier phase signal, in the satellite time frame, is given by

$$T_t = \frac{\Phi_{CR}(T_t)}{f_{CR}} = \frac{\varphi_{CR}(T_t) + N}{f_{CR}} = \bar{T}_t + \frac{N}{f_{CR}}. \quad (10.7)$$

The pseudorange from carrier phase measurements is given by

$$R_{CR} = c(t_r - \bar{T}_t) \quad (10.8)$$

where c is the signal propagation velocity. With the ambiguity term

$$c \cdot \frac{N}{f_{CR}} = N \cdot \lambda_{CR} \quad (10.9)$$

the observation equation for carrier phase measurements, becomes

$$R_{CR} = S + c(dt_u) + c(dt_a) + c(dt_s) + c\left(\frac{N}{f_{CR}}\right) + \varepsilon_R \quad (10.10)$$

where ε_R is the observation noise, S again is the slant range, dt_s is satellite clock error with respect to GPS system time, dt_u is clock synchronization error, dt_a is the atmospheric propagation delay, which can be separated into ionospheric and tropospheric components.

Initially, much of the error in GPS positions is introduced by imperfections in the receiver and satellite clocks. By having two receivers, in close proximity, estimating pseudoranges from two satellites or *double differencing*, clock offsets in the receivers and satellites and atmospheric propagation delays drop out of the expression in Equation 10.10. By this approach, the position of the rover station can be determined within millimeters. To accomplish this, a statistical process is undertaken whereby the pseudorange sets for all the available satellites are considered, and the ambiguity N_{cyc} is resolved to produce the most probable solution. A variety of methods for ambiguity solution are discussed in Seeber (1993). The successful solution of the ambiguity problem is difficult if the data quality is poor, e.g. corrupted by multi-path effects (see 10.7.2), if four or fewer satellites are available, if the ionosphere is disturbed, or if the observation time is short (less than 30 minutes). In this process, the two receivers must be within 30 km to solve for the ambiguity and minimize ionospheric delays, ideally even closer to truly resolve tropospheric errors.

As discussed later in this chapter, it is the preferred GPS configuration for Civil Engineering monitoring and, as detailed in Chapter 11, is also used in this study. When using the dual frequency, carrier phase information and in a DGPS configuration, the additional error (E_d) induced by the baseline separation, d , is 1 to 2 ppm (ppm: parts per million, determined by dividing baseline distance in km by 1,000,000). This error is in addition to the underlying errors (E_0) in the displacement calculations due to other error sources that are not position dependent, yielding an overall limit on GPS accuracy of

$$E = E_0 + E_d d . \quad (10.11)$$

In general, these systems can achieve accuracy of 0.5-20 mm (Leica, 1999). Note that this Differential Phase Positioning technique is often used for Real-Time Kinematic (RTK) GPS monitoring, which integrates a radio data link to transmit satellite data from the reference to the rover, enabling coordinates to be calculated at the rover in real-time. As will be discussed later in Section 11.2.2, the success of this approach is completely reliant upon the radio link, which is prone to interference from other radio sources and line of sight blockage (Leica, 1999). If contact is lost, ambiguities can no longer be resolved and the estimated positions will lose accuracy.

10.7 Residual GPS Errors

Even though the RTK GPS configuration discussed in Section 10.6.2 is capable of achieving tracking down to the millimeter level, there are still residual sources of GPS errors that cannot be fully corrected for. For example, there are a number of errors that are inherent to current satellite technology and the reliability of state-of-the-art GPS

receivers. Errors associated with the satellite clocks and the receivers themselves are anticipated to diminish as these technologies continue to advance. In the same manner, the *ephemeris* errors, mistakes the GPS satellites make in predicting their current position based on their orbits, will also reduce from the current level of about 1 m as GPS advances. However, Dilution of Precision (DOP) errors and multi-path errors are perhaps the most significant and persistent sources of error.

10.7.1 Dilution of Precision Errors

While the number of satellites available overhead is important, their position in the sky also dictates the accuracy with which positions on Earth can be determined. This position is identified by an elevation and azimuth coordinate. The azimuth dictates the aerial position of the satellites in terms of the four quadrants of the sky above the antenna, taking on values from 0° to 360° . The elevation dictates the angle formed by the satellite position and the ground plane and will not exceed 90° . A schematic of the elevation and azimuth is provided in Figure 10.4.

All GPS positions are determined by the surveying concept of resection. Given the pseudorange to one satellite, the position of the receiver is known to be at some point on the surface of an imaginary sphere with its origin at the satellite. With each additional satellite that is considered, an additional imaginary sphere intersects the first. With each resection, the position is narrowed to a smaller and smaller area. When the satellites involved in this resection are well-spaced, the position of the receiver can be determined to be within the shaded region shown in Figure 10.5 and the margin of error is small. When satellites are too close together, the size of the shaded area increases.

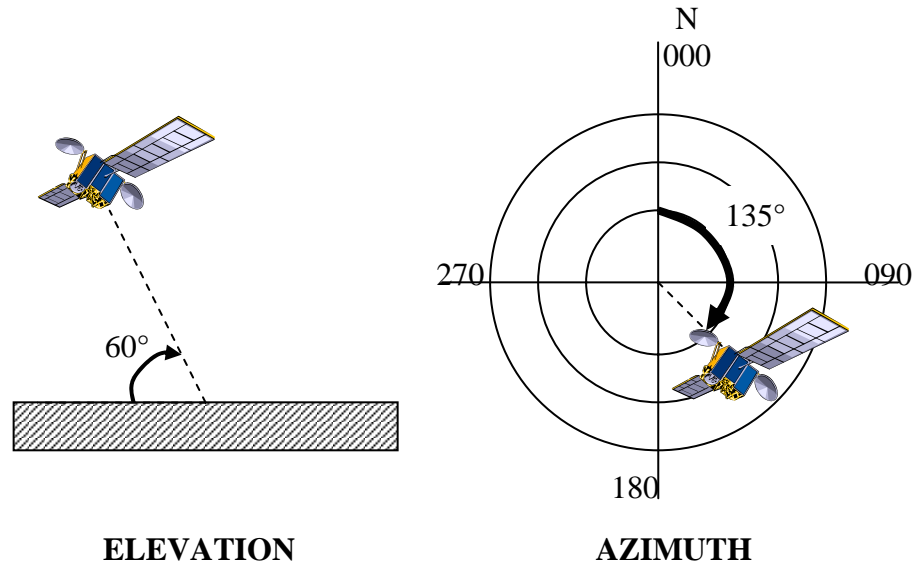


FIGURE 10.4. Schematic of elevation and azimuth measures for a GPS satellite at 135° azimuth and 60° elevation

The position dilution of precision (PDOP) can be viewed as the volume V of a tetrahedron that is formed between the satellites and the user position on Earth

$$PDOP = \frac{1}{V}. \quad (10.12)$$

The best solution is obtained when this volume is maximized. PDOP quantifies the size of the shaded region in Figure 10.5, reflecting the accuracy of the three position ordinates and time. It is at a minimum when 3 satellites are spaced at 120° in plane and a fourth satellite is directly overhead. For quality tracking via GPS, PDOP should be no greater than 3.

The accuracy of GPS positioning depends on the accuracy of a single pseudorange measurement, quantified by its standard deviation σ_r , and the geometric

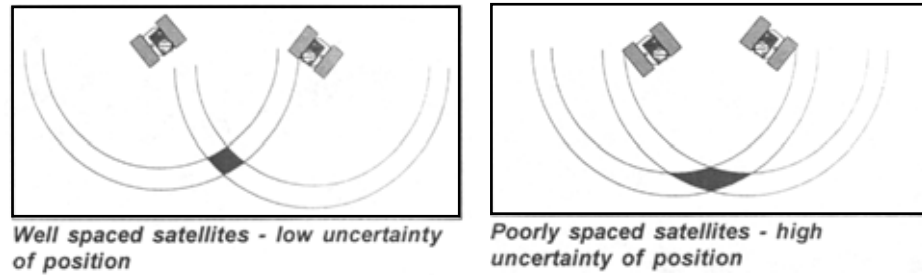


FIGURE 10.5. Schematic representation of satellite configurations leading to low DOP (left) and high DOP (adapted from Leica, 1999)

configuration of the satellites. The relation between the standard deviation of pseudorange and the associated standard deviation of the desired position or time estimate σ^* is described by the appropriate DOP factor

$$\sigma^* = DOP \sigma_r . \quad (10.13)$$

Substituting in HDOP (Horizontal Dilution of Precision), σ_H is obtained; substituting VDOP (Vertical Dilution of Precision), σ_V is obtained; substituting PDOP (Position Dilution of Precision), the standard deviation σ_P of the 3D position is obtained; and substituting TDOP into Equation 10.13, the standard deviation of the time ordinate σ_T is obtained. The geometric dilution of precision is related to the position and time precision measures by

$$GDOP = \sqrt{(PDOP)^2 + (TDOP)^2} . \quad (10.14)$$

GDOP should be kept under 4 for reasonable accuracy. With 24 satellites now in orbit, variations in DOP are less critical than in the early stages of the GPS program, and PDOP remains usually below 3.

10.7.2 Multi-Path Errors

As phase tracking leads to better accuracy, it is the preferred technique for high-precision GPS. As DGPS can reduce many significant errors, multi-path (Axelrad et al., 1996) then assumes the role as primary error source, particularly in urban areas. This error is analogous to the ghosts observed on television when a signal is directly received from the station and the same signal arrives shortly thereafter following a reflection off of one or more objects. These reflected signals, having a longer path, are delayed, resulting in a faint ghost beside the image on the screen. This delayed signal impacts the GPS receiver in a similar way. Although spread spectrum receivers lock in on the strongest signals, the interference due to multi-path errors can still be present and prevent the satellite from being accurately tracked. As cities with large buildings present more reflective objects, these errors can be concerning in urban areas. Though the effects on satellite position errors are about 0.5 m, they can cause code measurements to be 100 times noisier.

Multi-path also causes a phase shift in carrier phase observations, introducing a significant periodic bias in the range observations. The direct A_D and reflected A_R signals can be represented by a simplified model

$$A_D = A \cos \Phi_D \quad (10.15)$$

$$A_R = \alpha_D A \cos(\Phi_D + \Phi) \quad (10.16)$$

where α_D is a damping factor between 0 and 1, with 0 implying no reflection and 1 implying strong reflection. Φ_D is the phase position of the direct signal and Φ is a phase

shift of the reflected signal relative to the direct signal phase. Superimposing these two signals yields a resultant multi-path error Θ in the observed carrier phase

$$\Theta = \arctan\left(\frac{\sin \Phi}{\alpha^{-1} + \cos \Phi}\right), \quad (10.17)$$

taking on a maximum value of 90 degrees. Due to changing satellite geometry, the multi-path effect on carrier phases shows a period on the order of 30 minutes.

The ground reflections leading to multi-path errors can cause problems for phase tracking systems as discussed above. To prevent errors in phase calculations, multi-path contamination must be rejected as the signal is acquired. Fortunately, this can be largely achieved through the use of choke ring antennas, which reject reflected signals as they arrive at the receiver antenna. In terms of their design, the use of flush-mount antennas with reflective surfaces composed of concentric conductive choke rings of various radius and depths, connected to a ground plane, has been found to be effective (Tranquilla et al., 1994; Counselman, 1999). These antennas are designed to reject radio waves coming from below the horizon, while accepting signals from directly above. More detail on these antennas will be discussed in Chapter 11. Although choke-ring antennas offer the best defense against multi-path contamination, some residual effects may still infiltrate the signal. As a result, manufacturers of GPS receivers are now working toward developing analysis frameworks that can identify, isolate and remove the traces of multi-path errors in the satellite data, thereby removing it directly from the output displacement estimates (e.g. van Nee, 1995) or incorporating hardware features to prevent the false lock points associated with the multi-path problem (see www.javadgps.com). This

however is an area of research that has not fully materialized in current receiver technologies, though making progress. In the meantime, the residual multi-path effects in GPS displacement data can be distinguished by recognizing that they manifest themselves as long period trends in the data, as shown in Equation 10.17 and Figure 10.6, which can be removed via filtering approaches (Chen et al., 2001) and other strategies discussed in Chapter 13. A summary of all the sources of GPS error, and available remedies, are tabulated in Table 10.2.

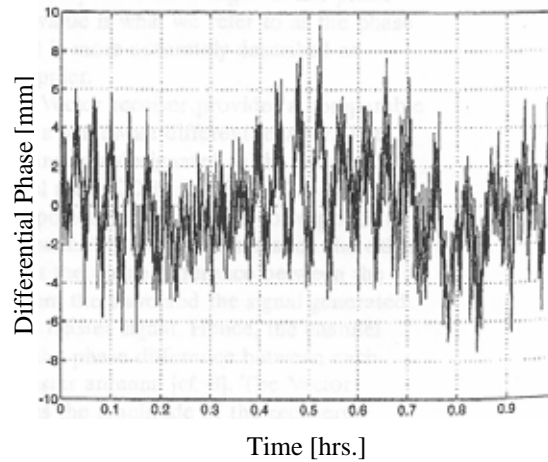


FIGURE 10.6. Errors in differential phase data manifesting long-period multi-path errors (taken from Axelrad et al., 1996)

10.8 Motivation for Structural Monitoring Applications

As the previous sections have detailed, the available GPS configurations and receiver sampling capabilities currently provide the ability to track dynamic displacements of objects with high-accuracy (on the order of millimeters). Though accelerometers previously provided the standard by which global motions of a large Civil Engineering

TABLE 10.2
SUMMARY OF INHERENT ERRORS IN GPS AND PROPOSED
SOLUTIONS

GDOP	→	No remedy
Ionosphere Errors	→	Dual Frequency Calculations
Troposphere Errors	→	DGPS
Ephemeris Errors	→	Minimized as technology advances
Satellite Clock Errors	→	Minimized as technology advances
Multi-path errors	→	Choke Ring Antennas, high pass filtering
Receiver Errors	→	Minimized as technology advances

structure were tracked, they were incapable of recovering complete displacement information, as static displacement due to thermal heating, settlement, or mean wind loads could not be recovered via integration. Further, the recovery of any displacement information from accelerations is difficult to achieve in real-time due to the integration involved. Prior to the advancement of GPS systems, there were limited options for accurately measuring these displacements, e.g. laser interferometer, and many of these were not feasible for unattended, continuous operation, particularly in a range of weather conditions, nor could they produce streaming real-time information. Further, in seismically-active regions, permanent displacement of the ground following strong shaking results in significant inaccuracies in traditional surveying techniques, as pre-established benchmarks critical in construction of civil infrastructure are distorted (Stein et al., 1997). However, the move to surveying technologies based on satellite information allows these offsets to be readily determined and corrected to permit continued use of the markers after significant events. Further, this information on permanent offsets of land markers can be beneficial in post-disaster damage assessment. For example, RTK GPS has been used by structural engineers in Japan and California to assess how much a

bridge or highway has permanently displaced following an earthquake or landslide (Turner, 2002). Now the available technologies make GPS feasible for development as a new technology for Civil Engineering health monitoring.

10.8.1 Recent Applications to Civil Engineering Structures

The early work in GPS monitoring of Civil Engineering structures can be traced back to static and pseudo-static monitoring of settlements, thermal expansion and other long-period displacement trends in bridges and dams. For example, in January 1995, GPS was used for a one-day test of France's Normandy Bridge under controlled traffic loading to verify that performance was consistent with design specifications (Fairweather, 1996). Later that year, in a permanent application, three continuously operating GPS units were dispatched to monitor the static displacements of the Pacoima Dam in California, sampling displacements every 30 seconds (Hudnut & Behr, 1998). Analysis techniques for identifying outliers in the data collected over three years at this site is provided in Behr et al. (1998). The following year, Applied Research Laboratories at the University of Texas temporarily implemented their Bridge Deformation Monitoring System (BDMS) at the Blackwater Bridge in Florida to conduct a similar static settlement survey. By averaging their displacement measurements, they enhanced their 1 cm instantaneous accuracy down to 1 mm (Hyzak et al., 1997). Later that year, they performed a four-day dynamic monitoring program on the Fred Hartman Bridge in Texas. The Humber Bridge in England was similarly instrumented with five GPS units in early 1998 during a controlled loading experiment (Roberts et al., 1999). In addition, suspension bridges in Japan, the Akashi-Kaikyo Bridge (Kashima et al., 2000) and Hakucho Bridge

(Nakamura, 2000), and Hong Kong (Wong et al., 2001), the Tsing Ma Bridge, Kap Shui Mun Bridge and Ting Kau Bridge, have recently also utilized GPS for health monitoring studies and bridge operation and maintenance. Similar proposals are being considered for the Vincent Thomas Bridge in Los Angeles and the Golden Gate and Bay Bridges in the San Francisco area (Celebi & Sanli, 2002). In particular, the static displacements of the girder of Akashi-Kaikyo Bridge measured by GPS were used to validate the ability of current analytical approaches to predict gust responses (Toriumi et al., 2000).

Specifically, in the context of tall structures, the Calgary Tower in Alberta, Canada (160 m) (Lovse et al., 1995) and the Di Wang building in China (384 m) were monitored briefly to explore the efficacy of GPS for determining wind-induced response. The Di Wang building was first studied in September 1996 under the action of a typhoon (Guo & Ge, 1997) and revisited later by Chen et al. (2001). Meanwhile, the movement toward continuous monitoring for extended periods of time is now being promoted by Celebi and his collaborators (1999, 2000, 2001), for 34 and 44-story buildings in California, and Tamura (2002) for health monitoring, as well as the full-scale monitoring project for tall buildings in Chicago (Abdelrazaq et al., 2000), introduced in Chapter 9, involving the GPS system detailed in Chapter 11 and calibrated in Chapter 12.

10.8.2 Insights from Previous Research

Tamura (2002) has advocated the potential of GPS for health monitoring and urban disaster response, following a number of experiments, including dynamic calibration tests for a number of sine waves simulated via shaker for varying frequencies and amplitudes (Tamura et al., 2001). Their findings indicate that the tracking ability for signals less than

2 Hz and with amplitudes greater than 2 cm were quite accurate. These researchers also observed good correlation between measured accelerations and GPS displacements of a 1.6 m flexible tower model and a 108 m steel tower, when PDOP was less than 2.5. In the full-scale steel tower, the researchers were able to recover both components of wind-induced response, including a static displacement of 4 cm, overlaid by the fluctuating component at the fundamental frequency of the tower. The detection of static displacement due to thermal effects and the mean wind components were discussed in more detail in Tamura (2002).

The work of Celebi and his various collaborators (1999, 2000, 2001) on GPS monitoring of buildings in Los Angeles and San Francisco have similarly motivated its permanent use in health monitoring applications in seismic zones. These applications integrate traditional accelerometer-based monitoring systems with three GPS units: two on the structure being monitored in order to capture translational and torsional motions, and a third on a nearby reference structure. Celebi et al. (1999) discuss the results of their first monitoring project on a 44-story building in Los Angeles. Their findings suggested that even at low amplitudes of response and with low signal to noise ratio, the GPS measurements were able to extract the frequencies of the system, indicating that under larger displacements, results are anticipated to only improve. The subsequent application of a similar system to a 34-story building in San Francisco proved to be equally effective, despite the low amplitude motions observed thus far (Celebi et al., 2002).

Temporary installations have also provided great insights into the successes and challenges of GPS monitoring, such as in the case of many of the bridge monitoring

programs mentioned in the previous chapter. Lavose et al. (1995) instrumented the Calgary Tower for 15 minutes on a windy day, using DGPS over a 1 km baseline. During this abbreviated monitoring period, eight satellites remained in view to insure a GDOP of 2-3. Under these optimal DOP conditions, the authors confirmed that multi-path errors were the primary error source, contributing a few centimeters at times and revealing a periodicity of a few minutes. Following the removal of these long period trends, the standard deviation in the GPS displacements was below 5 mm, affirming the accuracy of the system. Multi-path errors and satellite shielding due to cable stays and towers were also noted by Hyzak et al. (1997) for the Fred Hartman Bridge as well as by Roberts et al. (1999) in their study of the Humber Bridge. Similarly, Chen et al.'s (2001) two-day monitoring of the DiWang Building in China again affirmed the presence of multi-path errors in urban zones, introducing a wavelet-based scheme to filter out their effects. Nakamura's (2000) 3 week continuous GPS study of the Hakucho suspension bridge deck employed a configuration acquiring data at 1 sample per second (sps) with an RMS error in horizontal displacement of 1 cm + 2 ppm. Though multi-path errors were not a problem in this open environment, the system occasionally could not collect data due to a lack of satellites. Still the findings revealed that GPS could identify natural frequencies with same accuracy as accelerometers and was able to capture pseudo-static trends in displacements due in part to daily thermal trends that were not recovered by double integration of acceleration data. Further, these measured static displacements were found to compare well with finite element model and wind tunnel predictions.

10.9 Summary

The DoD established the existing GPS network in theory back in 1973, bringing it to full functionality in 1995. Since then, GPS technologies have rapidly advanced to a level where real-time kinematic GPS configurations can track displacements of a body to millimeters at up to 10 samples per second (sps). As newer satellites are launched in the next 10-20 years, the errors inherent to the satellites themselves will continue to diminish and accuracy levels may improve even further. Further, as more satellites become available, DOP errors can reduce even further. This may be achieved through the use of receivers capable of tracking not only original GPS satellites but also satellites belonging to other international satellite systems, such as the former Soviet Union's GLONASS (Global Navigation Satellite System) (Seeber, 1993) and the European Space Agency's Galileo program (Davis, 2003), increasing the number of simultaneously visible satellites at a given location to possibly twenty. As a result, now is an opportune time to begin the development of RTK GPS for Civil Engineering applications to monitor global static displacements of large structures that previously could not be recovered from accelerations. The next chapter will discuss the specific hardware and software necessary to develop a high-precision GPS for application in a long-term, full-scale monitoring project in Chicago, as well as a series of tests that were conducted to validate its accuracy.

CHAPTER 11

OVERVIEW OF GLOBAL POSITIONING SYSTEM CONFIGURATION AND CALIBRATION TESTS

11.1 Introduction

With the rapid development of GPS hardware, current accuracy levels and available sampling rates now enable the use of GPS for high-precision, dynamic monitoring, prompting the introduction of these technologies in the current research effort. This chapter overviews the GPS software and hardware configurations that were adopted in this study and introduces a testing protocol that was developed to verify the performance of the system for a variety of signals and scenarios.

11.2 GPS Components

The GPS required for the low-amplitude tracking anticipated in this project necessitated a unit with high precision, coupled with a sampling rate adequate to track the dynamic motions of Civil Engineering structures. The Leica line of receivers, at the time of purchase, offered sampling rates and resolution superior to its competitors and became the choice for this study. Tamura et al. (2001) and other researchers have also used

systems from this line, namely the MC1000. Ultimately, the Leica Continuously Operating Reference Station (CORS) configuration was adopted. The system features two hardware components: Leica MC500 receiver, the newest generation receiver following the MC1000, and a choke ring antenna, which are discussed herein.

11.2.1 GPS Receiver

The Leica MC500 receiver has the capability of tracking satellites from horizon to horizon on both L1 and L2. As discussed in the previous chapter, this is essential, since high accuracy receivers must utilize dual frequency measurements, i.e. the L1 & L2 carrier phase P-Code, which is tracked via 12 parallel channels, each channel continuously tracking a particular satellite using ClearTrack™ On-board, a tracking technique patented by Leica. The flexibility of the system allows any number of configurations, i.e. the receiver can be configured for real time broadcast of data or ring buffer log the data on internal 96 MB PC cards for post-processing. The aluminum unit's four sealed LEMO power ports and communications connectors (shown in Figure 11.1) permit RS232 serial interface and provide the ability to use varying supporting instrumentation, e.g. tilt sensors, meteorological sensors, etc., which can be directly powered through the GPS receiver. These interfaces also permit the integration of communications devices to broadcast real time GPS positions using three different message formats: Radio Technical Commission for Marine Services (RTCM), Compact Measurement Record (CMR) or Leica binary (LB2). Coupling these communications capabilities with an advanced processor, this receiver can broadcast and receive data at up

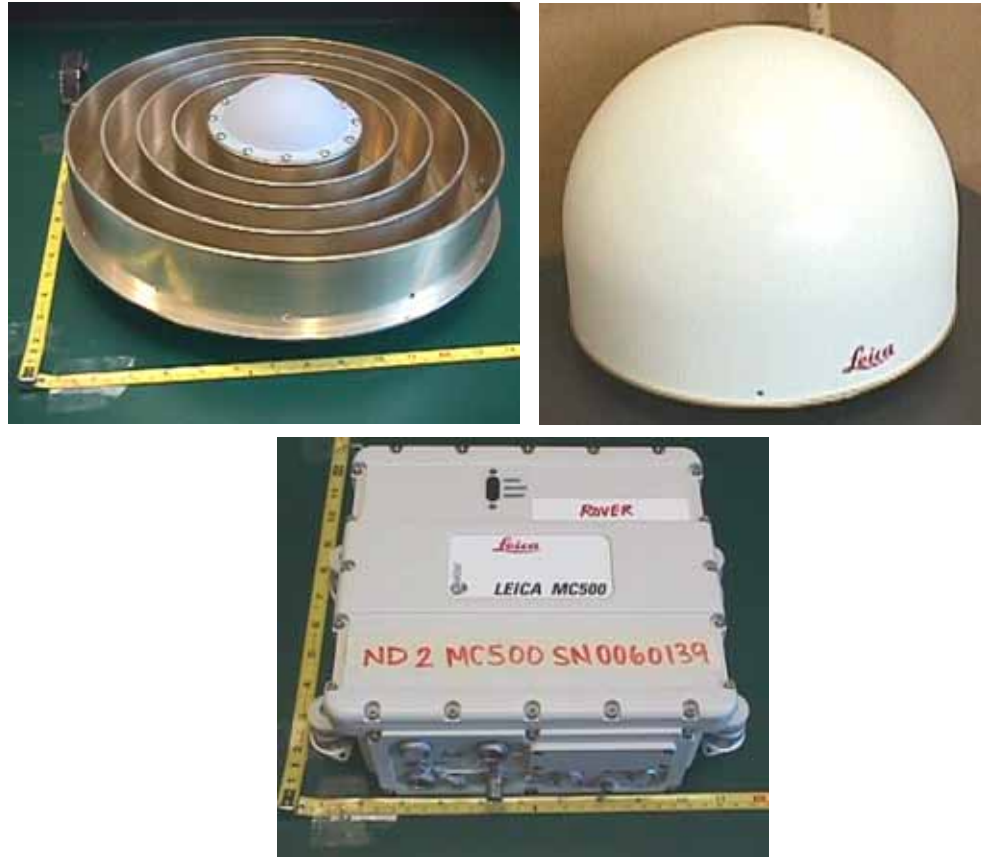


FIGURE 11.1. Choke ring antenna (top, left), outfitted with protective dome covering (top, right) and GPS receiver (bottom)

to 10 positions per second, an adequate sampling rate for most Civil Engineering applications in dynamic monitoring.

11.2.2 GPS Antenna

To maximize the accuracy of the system, an International GPS Service (IGS), gold anodized choke ring antenna, precision machined from a solid aluminum block and designed by Jet Propulsion Laboratory (JPL), was purchased. The antenna incorporates a ground plane, or circular disk base approximately 50 cm in diameter, that prevents low

elevation signals from reaching the antenna. The four concentric choke rings encircle the antenna, trapping any indirect signals (see Figure 11.1). While larger than other antennas types on the market, this antenna is uniquely designed to minimize the effects of multipath errors, discussed more fully in Chapter 10, by rejecting the reflected signals out right. Recall that these errors prove to be one of the major degraders GPS measurements in urban environments (Lovse et al., 1995; Chen et al., 2001). The antenna is also resistant to RF jamming, another important consideration in urban applications. The Leica antenna and receiver are shown in Figure 11.1, along with the protective dome designed to shield the antenna from the elements.

11.2.3 Accuracy

Table 11.1 lists Leica's reported accuracy levels for a DGPS system employing the receiver and antenna described above. The L1 and L2 Code accuracy levels are 5 cm, in comparison to the L1 and L2 Carrier Phase, indicating the increased accuracy that can be obtained by using phase information for position calculations. Also note that the P code and C/A code have identical accuracy levels since SA restrictions have no influence on DGPS users. However, the final two rows of Table 11.1 are most critical to gauge the tracking ability of the system. The RTK and static accuracy levels provided in these two rows reflect the dependence of the error upon the distance between the rover and reference stations in a DGPS configuration, though Leica indicates that the RTK distance-dependent component of the error is more like 1 ppm in practice.

TABLE 11.1

ACCURACY LEVELS FOR LEICA RTK GPS

L1 Carrier Phase	0.2 mm (RMS)
L1 C/A Code	<5 cm (RMS)
L2 Carrier Phase	0.2 mm (RMS)
L2 P Code	<5 cm (RMS)
RTK Accuracy	5 mm + 2 ppm
Static Accuracy	3 mm + 0.5 ppm

NOTE: ppm = parts per million, determined by dividing baseline distance in mm by 1,000,000.

11.2.4 GPS Hardware Configuration

While the Leica GPS hardware is capable of streaming displacements in real time, this requires constant communication between the reference and rover receivers via radio modems, cellular telephones or some other wireless communications link (Celebi, 2000; Tamura, 2002). As the final application of the system being developed in this study requires installation in the downtown Chicago area on a building that houses a number of radio and television communications sources, there were concerns for interference and even occasional loss of this vital communications link. If contact is lost, ambiguities can no longer be resolved and the estimated positions will lose accuracy. It turns out that this communications link is the most difficult component of the system to configure (Leica 1999). In the RTK monitoring of the Humen suspension bridge in Guangdong province of China, the potential for signal loss was similarly noted and the reference and rover were linked by a fiber optic communications system (Xu et al., 2002). However this

option was not feasible for this application so a more conservative approach was adopted in which each GPS receiver logs its data to an internal PC card, uploaded to a laptop computer on site, and then downloaded via modem to an analysis portal where the data could be post-processed. The adoption of the post-processing option is also attractive in that it allows the flexibility to specify and change processing parameters after the data has been acquired, an option not available using a fully RTK scheme. Thus the user can vary the solution strategy, ionospheric model, stochastic model and tropospheric model to observe their influence on the measured positions.

This results in the final configuration shown in Figure 11.2, held within an elevated metal enclosure on the highest mechanical floor of each host building. The enclosure contains the GPS receiver, laptop and an APC Battery BackUp 500 VA uninterruptible power supply (UPS) sufficient to run the system in the event of temporary power outages of approximately 15 minutes or less. The laptops being used are DELL Latitude C600s with 1 GHz Pentium III processors, 256 MB of RAM and 10 GB Hard Drive, running Windows NT v. 4.0. As the enclosures are being housed indoors, the environmental conditions should be well within the operating limits of each of the components, listed in Table 11.2, provided that adequate ventilation is present. A mock-up of the system illustrated that the temperature within the enclosure rose 8°F during the continuous operation of the receiver and laptop. The inclusion of two 4.7" Muffin fans and vents provided sufficient ventilation to maintain approximate room temperature within the enclosure during extended operation of the system. The GPS receiver is linked to its antenna on the rooftop by less than 200 feet of LMR 400 coaxial cabling, terminated by TNC connections. Note that coaxial cabling connecting the choke ring

Choke Ring Antenna on Roof

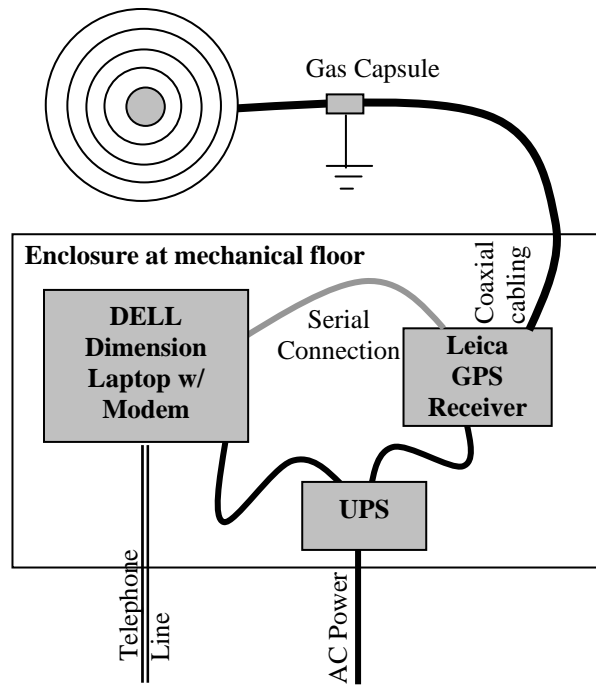


FIGURE 11.2. Configuration of GPS data acquisition system installed in each building

TABLE 11.2

ENVIRONMENTAL CONSTRAINTS ON GPS EQUIPMENT

	Temperature		Humidity
	Operating	Storage	
Dell Latitude Laptops	32°F - 95°F	-40°F - 149°F	10% - 90%
GPS Receiver	-4°F - 131°F	-40°F - 167°F	Sealed
GPS Antenna	-40°F - 167°F	-40°F - 167°F	Sealed
PC Card Memory	-4°F - 167°F	-40°F - 167°F	Sealed
Power Supply	32°F - 104°F	5°F - 113°F	0% - 95%

antenna to the GPS receiver is interrupted by a grounded gas capsule for the purposes of in-line lightning protection, as explained in the following section.

11.2.5 Lightning Protection System

The threat of surges infiltrating the enclosure and damaging the electronics within is a reality that must be addressed in the design of the complete monitoring system. While the units are protected from surges in the AC power supply and modem line, as contact with both of these external sources is filtered through the UPS, complete with its own lightning and surge protection system, surges resulting from direct or indirect lightning strikes or other electromagnetic fields can still enter through the coaxial cabling feeding the antenna signal down to the receiver. To minimize the threat of a direct lightning strike, it is in general recommended that the antenna be located within the protection zone of an external lightning protection system. This insures that the antenna itself is protected from direct strikes, however, the potential for electromagnetic pulses (EMPs) is still prevalent.

Even if lightning only strikes nearby, an interference current may flow toward the equipment. An in-line fuse or gas-filled surge protection device (SPD) must be installed to prevent voltage surges from penetrating the enclosure. The in-line SPD is installed outside of the building on the rooftop to prevent unwanted surges from venturing indoors. The device, shown in Figure 11.3, features the lightning protector assembly that threads into the coaxial cabling from the receiver enclosure at the protected side and links via a second length of coaxial cabling to the antenna. The assembly features a screw-cap chamber that houses the small gas capsule, comprised of two electrodes insulated by

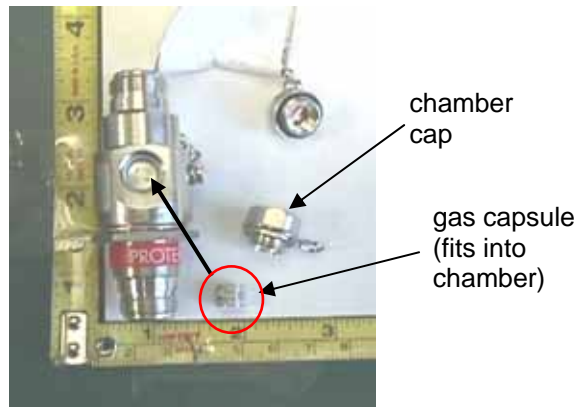


FIGURE 11.3. Huber + Suhner lighting protector with gas capsule

small ceramic tube. When a surge enters the assembly, the voltage across the surge protection capsule rises rapidly until it reaches its dynamic sparkover voltage, at which time capsule will ignite and become conductive. When this occurs, the energy is diverted from its path along the coaxial cabling, as the current will follow the path of least resistance through the surge protection capsule and to the ground, necessitating that the gas capsule be sufficiently grounded. Though a small part of the residual pulse still reaches the equipment, it is within the acceptable tolerances. Once the interference subsides, the system will revert to its original operation.

Though there are other strategies for surge protection available, gas capsule protectors are the only viable solution for this application, as they allow DC/AC power to be carried through the coax line, feeding power to the rooftop antenna. The selected EMP protector is the Huber+Suhner 3402.17.K featuring the 73 Z-0-0-48 gas capsule. The 3402 series is well-suited for this application due to its broadband operating range, DC to 2 GHz. Note that each capsule model has unique sparkover properties dictated by its gas

properties, pressure and electrode gap, with this particular model having a dynamic sparkover voltage of 800 V. The gas capsules are easy to replace if service becomes necessary or they are damaged in a lightning strike.

11.2.6 GPS Data Acquisition Software

The operation of each GPS unit was accomplished via Leica's ControlStation (v. 4.2) windows-based software, developed to interface with the system 500 dual frequency GPS sensors. The software permits completely automated data acquisition, making it attractive for remote, unattended monitoring projects. While the programming of a GPS receiver can be complex, the user interfaces in ControlStation allow a number of site scenarios and data logging options (logging direct to PC, logging internally to sensor, sampling rate, duration of logging, etc.) to be readily defined and uploaded to the sensor, minimizing set up time. Interfaces within the software display receiver and satellite tracking, data logging status, transmission of real-time RTK or DGPS data and site scenario configurations. ControlStation also has menus for sensor configuration to broadcast and receive RTCM, CMR or LB2, providing flexibility to adapt to a real-time transmission protocol in the future.

Each laptop, in addition to running ControlStation (v. 4.2), is equipped with a copy of Symantec PC Anywhere (v. 9.2) to permit remote access to the units for activation and data download. PC Anywhere allows users to remotely access and control any host PC running the software. For this application, the post-processing PC at Notre Dame, also running PC Anywhere, remotely accesses a PC located at a Skidmore Owings and Merrill in downtown Chicago via the Ethernet. This downtown computer serves as a

local data hub from which the laptops at the monitored structures are accessed using PC Anywhere via modem to display their desktop on the remote computer, allowing the remote user to monitor the GPS acquisition process, initiate or terminate a data acquisition session or download data files for post-processing. Note that applications are still executed on the host PC and only keyboard, mouse and screen information are transferred between the remote PC and the host PC, minimizing the amount of information that must be transferred via phone line. Built-in security features provide a secure and virtual means to control the GPS in its full-scale application.

11.3 Field Site for Experimental Validation

In order to identify the best possible performance of the system, calibration tests were conducted in an open field location sufficiently free from potential sources of multi-path error and free from obstructions that may block lower elevation satellites from view. In general, there should be no obstructions above a 15° -mask angle measured with respect to the antenna base, as shown in Figure 11.4, in all directions. An open field test site was secured: the 118-acre Anderson Road property of the St. Joseph's County Park Department, located on Anderson Rd., 0.6 mi west of the intersection of Anderson Road and Ash Road in Granger, IN.

11.4 Test Configuration

A series of tests were conducted to verify the GPS performance quantified through the static background noise and the accuracy in dynamic tests simulated by moving the rover antenna according to a prescribed displacement trajectory using a small shake table. The

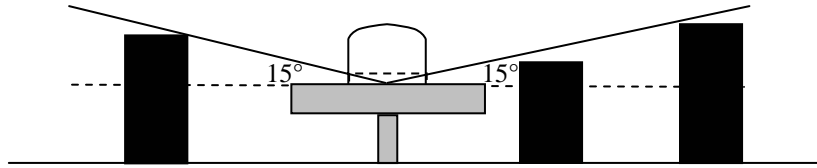


FIGURE 11.4. Demonstration of 15°-mask angle requirement limiting neighboring obstructions

two GPS receivers (reference and rover) and their supporting laptop computers were housed in the storage shed on the Anderson Road property, which supplied power to the experimental setup. This complete experimental set up included the shake table and a third computer that supports it. Each GPS receiver was linked to its respective choke-ring antenna in the adjacent field by 30 m of the aforementioned coaxial cabling. This length of cabling was sufficient to place the antennas approximately 27 m west of the shed (approximately 4.5 m tall), a sufficient distance to preserve the 15°-mask angle requirement.

The two GPS antennas were mounted on wooden platforms to elevate them above the surrounding terrain and to ensure they were not shielded by the shake table's supporting equipment or its operator. The mount for the rover unit, which was excited by the shaking table, was designed in a more rigid fashion than the stationary reference mount, so as not to induce any additional dynamics in the data. The rover unit mount was firmly clamped the shake table, so as to rigidly link the antenna and shake table. The shake table in essence embodies the roof of a building being monitored. The rover and reference antennas are shown on their respective mounts in Figure 11.5. Note that the rover mount was slightly taller, standing 126.7 cm, while the reference mount was 125.1

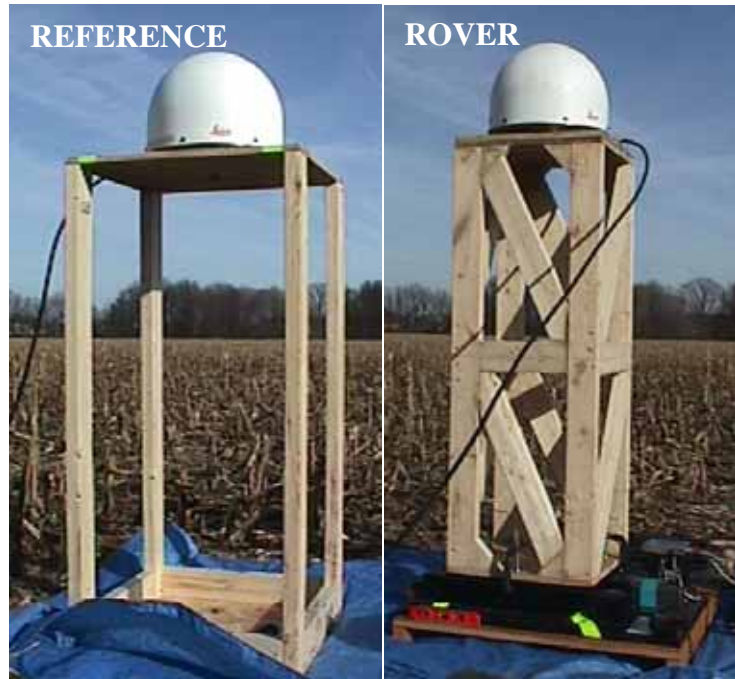


FIGURE 11.5. GPS reference and rover antennas affixed to rigid mounts

cm. So that the domed antennas do not shield one another, the assemblies must be a minimum of 1.25 m apart. For the purposes of testing, the two antennas were placed approximately 2.5 m apart along a north-south (N-S) axis.

The rover antenna mount was firmly clamped to the shake table oriented for motion along a N-S axis, as shown schematically in Figure 11.6. An *eTrex Summit* handheld GPS was calibrated in the field and used to establish true North and was compared to the prediction of a traditional compass. Once the orientation of the reference and rover were established, a self-survey was conducted by each of the GPS receivers for 10 minutes. During this period, the two units continuously updated estimates of the static position of each antenna in terms of latitude, longitude and elevation, using a least squares methodology to arrive at a “best” estimate of their location prior to testing. As

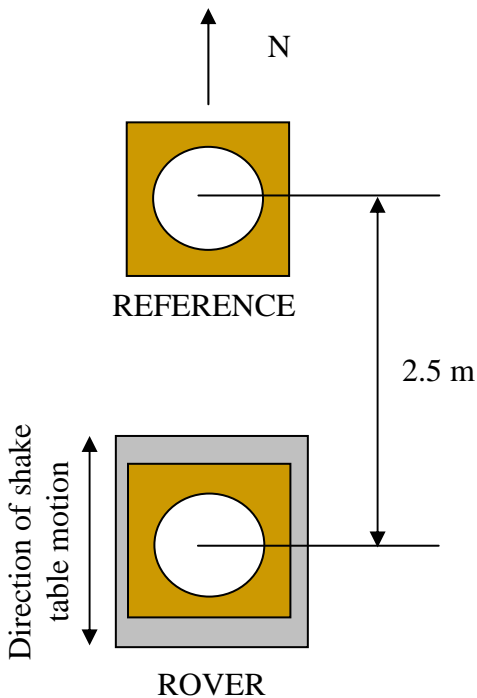


FIGURE 11.6. Orientation of reference and rover station for Tests 1-4

shown in Figure 11.7, the orientation of the GPS units was free from obstructions within the 15° mask angle requirement in all four directions to permit optimal views of the satellites in orbit.

Though the GPS antennas themselves are equipped to handle inclement conditions by virtue of the protective domes shown in Figure 11.5, the shake table and supporting electronics used in the calibration could not be exposed to extreme cold or moisture. This constraint limited testing to days free from the threat of precipitation and freezing temperatures. As a result, the first tests were conducted on a mild winter day, January 22, 2002. Additional tests were deemed necessary and were conducted on April 17, 2002.

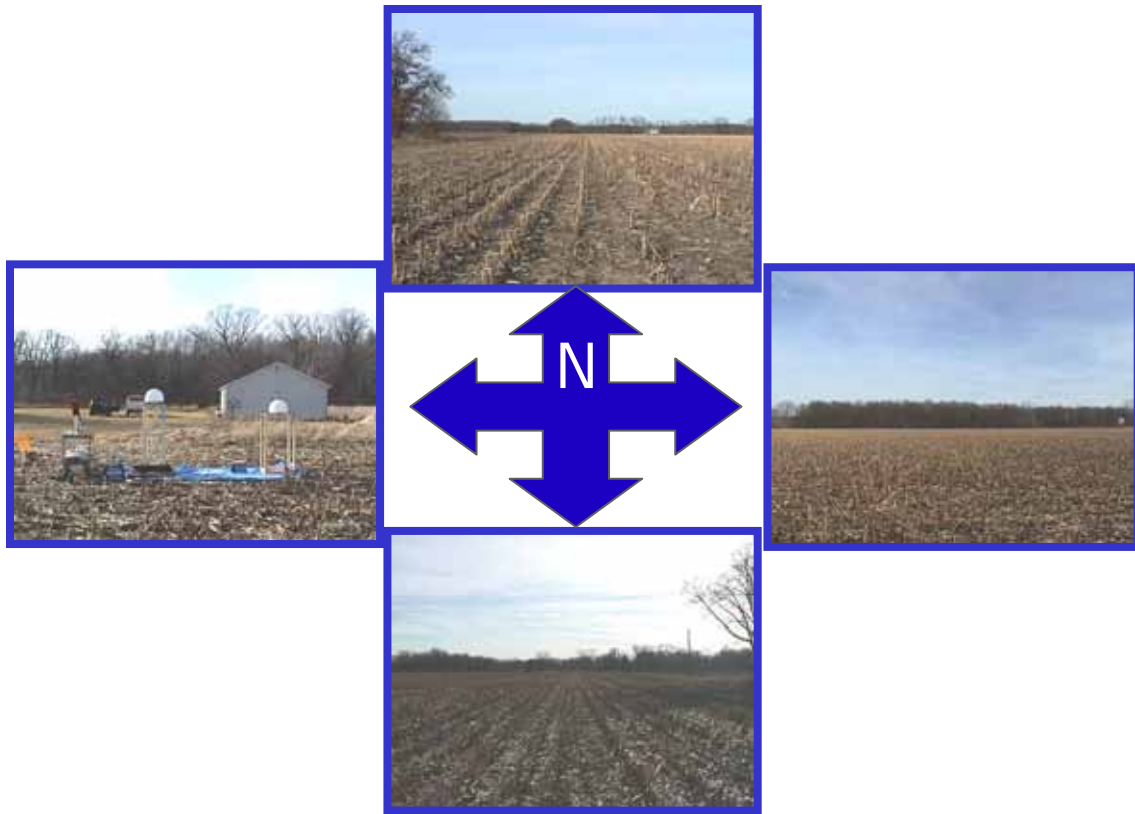


FIGURE 11.7. Views in each direction of test site

11.5 Overview of Tests

As the shake table is displacement-controlled, the physical rotation of the ball screw driving the table can be recorded via the encoder, providing a simple means to recover the actual displacements of the GPS antenna. These motions of the table were recorded from the output of the table's controller board manufactured by WinCon and saved for comparison to the GPS predictions of position. For each test, the receivers were activated via ControlStation, which had pre-defined site scenarios with relevant equipment parameters and the most recent self-survey information. These scenarios were uploaded to each receiver on the morning of the tests. For each test, data was logged directly to the

GPS receivers, sequentially filling their 10 internal ring buffers using the 96 MB PC cards to store the test data. Though the GPS receivers may also log data directly to the laptop computer, ring buffer logging is the only option that can realize the highest available sampling rate of the system, 10 Hz. That data is then downloaded to the laptops, where it is permanently archived after all ten buffers are filled. During ring buffer logging, the rover GPS unit is flagged as kinematic and the reference GPS unit is flagged as static to establish which of the two should be interpreted as stationary in the post-processing regimen.

11.5.1 Test 1a-c: Verification of Background Noise and Influence of Satellite Position

Not only the orientation but also the availability of satellites dictates the quality of the GPS predictions, quantified by the aforementioned DOP errors. Test series 1 explores this characteristic influencing GPS performance by conducting three static tests at different times of day. Figure 11.8 shows the satellite availability and DOP predicted for the testing date. Acceptable DOP values should range between 2 and 4. Test 1a was conducted during a time of degrading satellite availability, while Test 1b represents the transition from high to low DOP values and Test 1c represents period of relatively good DOP. These static tests will reflect the accuracy level of the GPS system, as a stationary rover should produce zero relative displacements and any detected displacement is a result of inherent GPS error. The limitations of GPS accuracy will be reflected by the level of motion “detected” in the stationary system, quantifying the background noise. For each test the rover and reference antennas remained on their elevated mounts, with

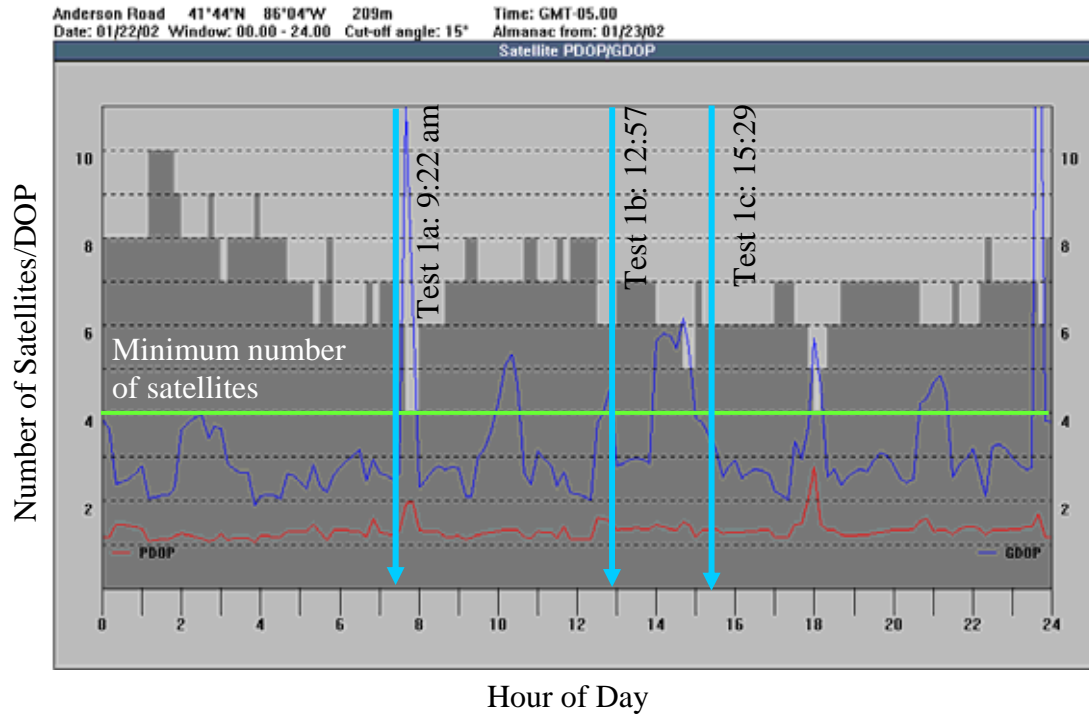


FIGURE 11.8. Predicted availability of satellites and dilution of precision for Anderson Road site on January 22, 2002 (screen capture from Leica software)

the rover mount secured on the centered shake table. Both units were held completely still and 10 minutes of data was collected.

11.5.2 Test 2a-w: Verification of Amplitude Sensitivity

The next series of tests was designed to quantify the range of frequencies and amplitudes that can be successfully tracked by the Leica MC500 system. Based on the manufacturer's specifications in Table 11.1, the system's RMS dynamic accuracy is estimated at 5 mm (baseline in this case is negligible). Therefore, sinusoids with amplitudes ranging from this lower limit of ± 0.5 cm up to ± 3 cm were used with frequencies of 0.1, 0.125, 0.15, 0.2, 1 and 2 Hz. The primary focus toward low frequency

signals was intentional, as they were selected to represent the fundamental sway frequencies common in the buildings that the system was designed to monitor. Unfortunately the shake table used in this study has inherent limitations in the tracking of large amplitude, high frequency signals constraining the high frequency, large amplitude tests to those listed in Table 11.3, which provides an overall quick reference for the various tests executed. Each of these tests was run for approximately 30 seconds.

11.5.3 Test 3a-f: Verification of Ability to Track Complex Signals

The next series of tests was designed to insure that the GPS system could sufficiently track complex signals, including those that realistically would be generated by the swaying of a tall building under wind. The first of these tests (Test 3a) simulated a quadratic chirp with frequency increasing from 0.1 to 2 Hz over 1 minute. A more random signal was generated in Test 3b using random, bandlimited, Gaussian-distributed, zero mean, white noise with peak amplitudes of ± 2 cm. The time step for the generation of the random signal was 0.2 s, thereby constraining the frequency content beneath 2.5 Hz. The signal was simulated for the duration of 60 seconds.

The next four tests simulated the response of a multi-degree-of-freedom oscillator to zero mean, Gaussian white noise, mimicking the response of building under the action of wind. The mass and stiffness matrices were selected so as to achieve natural frequencies similar to those observed in typical buildings. For Test 3c and 3d, a three degree-of-freedom (3DOF) system with frequencies at 0.12, 0.35 and 0.53 Hz was created, assuming each mode to have a critical damping ratio of 0.01. The system was engineered to respond dominantly in its highest mode, creating 5 minutes of a synthetic

TABLE 11.3
OVERVIEW OF CALIBRATION TESTS

Test	Description	Phenomena being monitored	Date
1a	Static	influence of DOP	1/22/02
1b	Static	influence of DOP	1/22/02
1c	Static	influence of DOP	1/22/02
2a	±0.5 cm, 0.1 Hz sine	amplitude, frequency limitations	1/22/02
2b	±0.5 cm, 0.125 Hz sine	amplitude, frequency limitations	1/22/02
2c	±0.5 cm, 0.15 Hz sine	amplitude, frequency limitations	1/22/02
2d	±0.5 cm, 0.2 Hz sine	amplitude, frequency limitations	1/22/02
2e	±0.5 cm, 1 Hz sine	amplitude, frequency limitations	1/22/02
2f	±0.5 cm, 2 Hz sine	amplitude, frequency limitations	1/22/02
2g	±1.0 cm, 0.1 Hz sine	amplitude, frequency limitations	1/22/02
2h	±1.0 cm, 0.125 Hz sine	amplitude, frequency limitations	1/22/02
2i	±1.0 cm, 0.15 Hz sine	amplitude, frequency limitations	1/22/02
2j	±1.0 cm, 0.2 Hz sine	amplitude, frequency limitations	1/22/02
2k	±1.0 cm, 1 Hz sine	amplitude, frequency limitations	1/22/02
2l	±1.0 cm, 2 Hz sine	amplitude, frequency limitations	1/22/02
2m	±2.0 cm, 0.1 Hz sine	amplitude, frequency limitations	1/22/02
2n	±2.0 cm, 0.125 Hz sine	amplitude, frequency limitations	1/22/02
2o	±2.0 cm, 0.15 Hz sine	amplitude, frequency limitations	1/22/02
2p	±2.0 cm, 0.2 Hz sine	amplitude, frequency limitations	1/22/02
2q	±2.0 cm, 1 Hz sine	amplitude, frequency limitations	1/22/02
2r	±2.0 cm ¹ , 2 Hz sine	amplitude, frequency limitations	1/22/02
2s	±3.0 cm, 0.1 Hz sine	amplitude, frequency limitations	4/17/02 ²
2t	±3.0 cm, 0.125 Hz sine	amplitude, frequency limitations	1/22/02
2u	±3.0 cm, 0.15 Hz sine	amplitude, frequency limitations	1/22/02
2v	±3.0 cm, 0.2 Hz sine	amplitude, frequency limitations	1/22/02
2w	±3.0 cm, 1 Hz sine	amplitude, frequency limitations	1/22/02
3a	Chirp	ability to track complex signals	1/22/02
3b	random noise	ability to track complex signals	1/22/02
3c	MDOF, 0.53 Hz ³ , σ =0.66 cm	ability to track building motions	1/22/02
3d	MDOF, 0.53 Hz ³ , σ =1.12 cm	ability to track building motions	1/22/02
3e	MDOF, 0.12 Hz ³ , σ =1.01 cm	ability to track building motions	4/17/02
3f	MDOF, 0.12 Hz ³ , σ =1.19 cm	ability to track building motions	4/17/02
4a	static with gas capsule I ⁴	influence of gas capsule	4/17/02
4b	static with gas capsule II ⁴	influence of gas capsule	4/17/02
4c	static without gas capsule ⁴	influence of gas capsule	4/17/02
5	±2.0 cm, 0.2 Hz sine	coordinate transformation	4/17/02
6a	static with mount	influence of elevated mount	4/17/02
6b	static without mount	influence of elevated mount	4/17/02

¹Table actually only realized sinusoid with approximately ±1.5 cm due to inherent limitations.

²Data originally acquired on 1/22/02 had slight ambiguity problem. Test repeated.

³Dominant frequency in response.

⁴Only these tests featured in-line lightning protection.

building response primarily at 0.53 Hz, sampled at 10 Hz. For Test 3c, the amplitude of the synthetic building response ranged from -2.23 cm to +2.20 cm, with zero mean and 0.6635 cm standard deviation, while for Test 3d, the simulated response had amplitudes from -2.28 cm to +3.29 cm, with zero mean and 1.12 cm standard deviation.

For the final two tests of this series, the scenario was identical except that the simulated 3DOF system had frequencies of 0.1156, 0.2135, 0.2790 Hz, responding dominantly in the first mode to parallel what may be observed in the full-scale application. For Test 3e, the amplitude range of the synthetic building response was -2.58 cm to +2.64 cm, with zero mean and 1.01 cm standard deviation. Test 3f featured the same system with a slightly larger amplitude response ranging from -3.23 cm to +3.22 cm, with zero mean and 1.19 cm standard deviation.

11.5.4 Test 4a-c: Influence of Gas Capsule

In order to protect the GPS receivers and their laptops on site from the risk of lightning, each GPS antenna was equipped with in-line surge protection in the form of a gas capsule, discussed previously. A series of tests was developed to investigate if the GPS signal degrades in any way by passing through the in-line protection. It was important to insure that DOP was not the reason for any detected degradation, so the tests were conducted over a window of time for which DOP held relatively constant for approximately 45 minutes. The predicted satellite availability and DOP for the April 17, 2002 testing date is provided in Figure 11.9 with the red box indicating the time over which the three tests were conducted. For Test 4a, the capsule assembly labeled I was

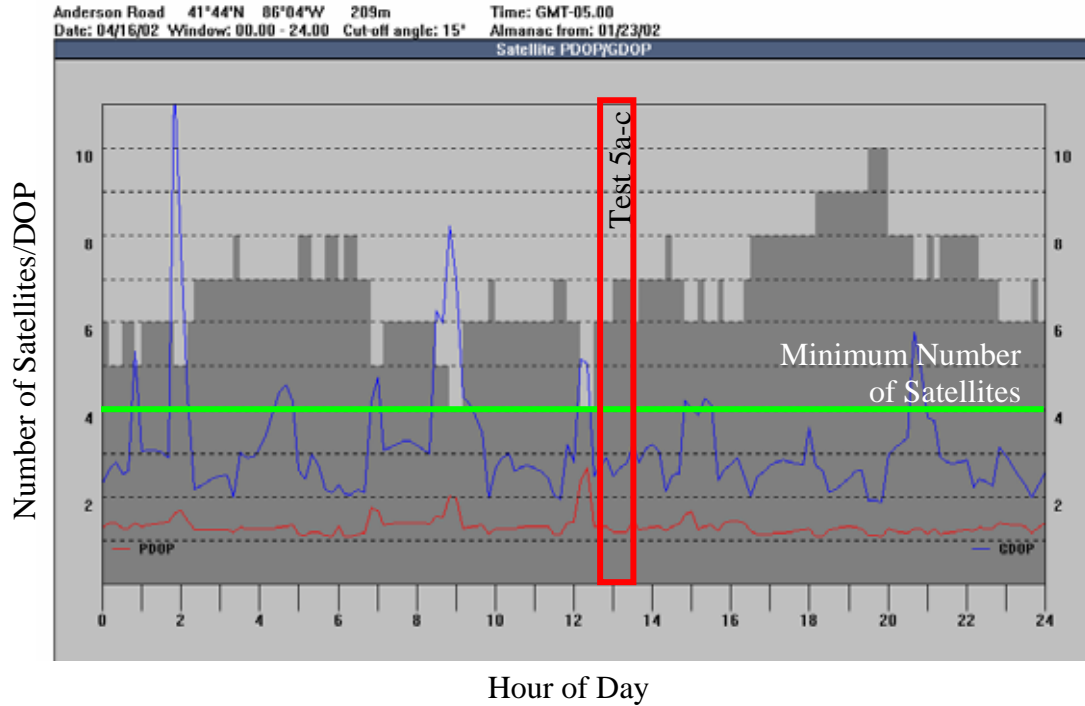


FIGURE 11.9. Predicted availability of satellites and dilution of precision for Anderson Road site on April 17, 2002 (screen capture from Leica software)

attached to the antenna line of the rover system, as shown in Figure 11.10. Static data was acquired for 10 minutes. Test 4b repeated this exercise with gas capsule assembly II. Finally, a 10-minute static test at a similar DOP level was conducted without any lightning protection for comparison.

11.5.5 Test 5: Coordinate Transformation Mock-Up

The GPS positions are typically viewed in terms of a local coordinate grid, yielding displacements along the N-S and east-west (E-W) axes. Often, the axes of the structure being monitored will not align with this natural coordinate system. While a new local coordinate system can be defined in the post-processing software, it is often easier to

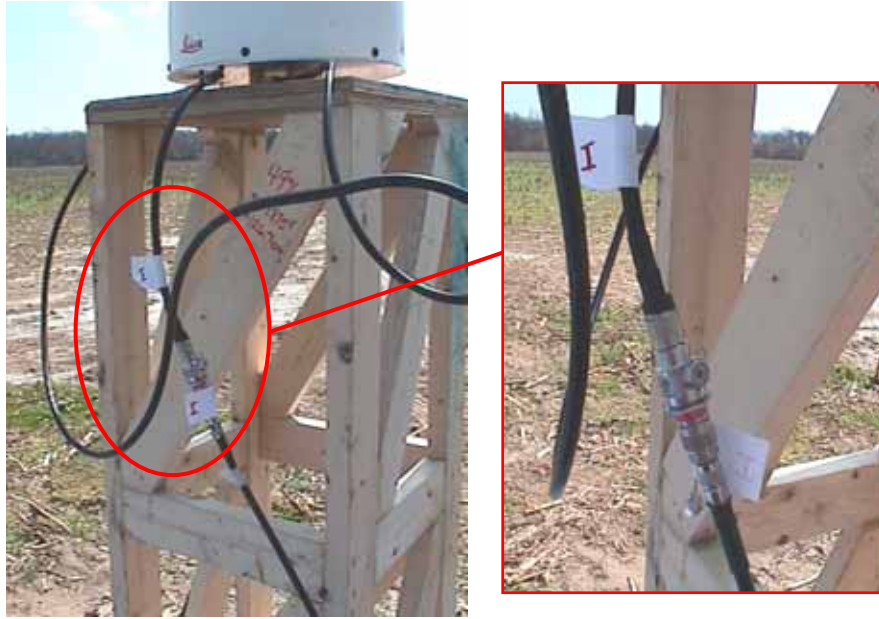


FIGURE 11.10. Photo of gas capsule assembly I in Test 4a

simply estimate the angle of deviation from the N-S axis and use basic trigonometry to identify the motion of the building along its major axes from their projections onto the N-S and E-W axes used in the GPS monitoring system. Test 5 simulated such a scenario by the rotating the shake table's axis of motion by approximately 45° counterclockwise from the N-S axis, using the handheld *eTrex Summit* GPS compass. The reference unit remained approximately the same distance, 2.4 m, from the shifted rover unit, as shown in Figure 11.10. The GPS system was then enabled and allowed to collect static data for a few minutes, after which the table was excited with a 0.2 Hz sine at ± 2 cm for 2 minutes. After the dynamic phase of the test was concluded, the table was zeroed and the GPS unit was allowed to take a few more minutes of static data. The data would then be analyzed to determine, first the ease of coordinate transformation and second the accuracy of the handheld *eTrex Summit* compass in determining the exact angle of rotation of the axis of

motion for full-scale applications and a methodology to better quantify the angle of deviation from the N-S axis.

11.5.6 Test 6a-b: Influence of Antenna Mount

Previous work in the area of GPS monitoring revealed that mount dynamics can pose serious problems for the accuracy of GPS monitoring (Ashkenazi & Roberts, 1997), potentially leading to a mount whose motions relative to the structure exceed the structural displacements themselves. For these reasons, a very rigid mount was designed for the rover antenna to insure that there was no motion of the antenna relative to the shake table surface. Though care must be taken in their design, the antenna mount is a necessary component of the GPS system as it helps to eliminate interferences that would occur if the antenna were merely fixed directly to the structure being monitored. The mounts used in the full-scale application are discussed in Chapter 13. Further, the potential for neighboring obstructions is markedly increased for antennas that have little to no elevation relative to their surroundings. It is typically suggested to elevate the antenna a minimum of 3 feet on a rigid mount, such as a tripod or pillar, to minimize these effects.

To validate the effects of the antenna mount on GPS performance, 10 minutes of GPS static data was collected with the rover unit its elevated mount, as shown previously in Figure 11.5. Note that the antenna units remained in the configuration shown in Figure 11.11 to avoid the need for a second self-survey. As this is a static test, the shifted orientation should be of little consequence. The antenna was then mounted directly to the

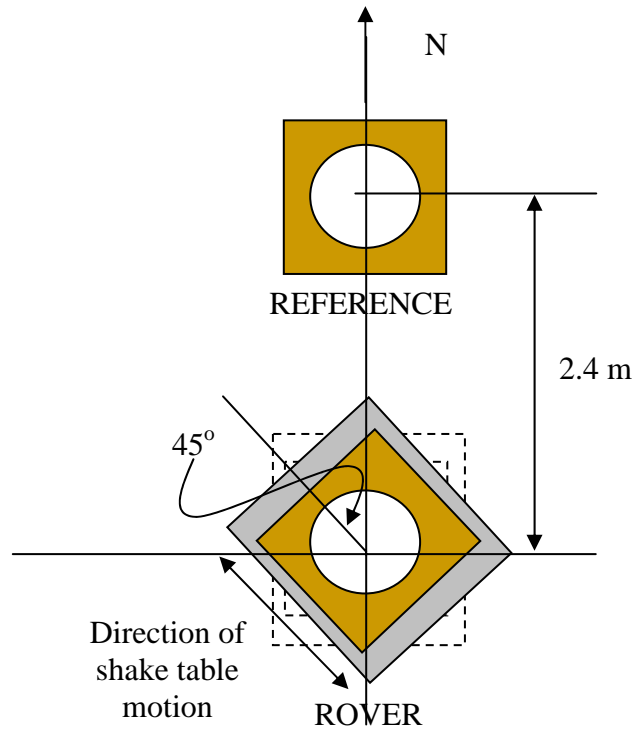


FIGURE 11.11. Orientation of reference and rover stations for Tests 5-6

shake table and 10 more minutes of static data were acquired. The reference station, during the course of the tests, remained on its elevated platform.

11.6 Post-Processing Protocol

After completion of tests, all GPS raw Leica binary data files from reference and rover units were transferred to an analysis PC (DELL Dimension 4100, 1 GHz Pentium III Processor, 256 MB RAM, 40 GB hard drive, Windows 98 OS) located in the NatHaz lab on the campus of the University of Notre Dame. This computer will serve as the post-processing station for the study where all raw GPS data is downloaded and processed using Leica's SKI-Pro Software, v. 2.1. The SKI-Pro software has a number of

capabilities (Leica, 2000) beyond the interests of this study; therefore, only parameters relevant to the post-processing of dual-frequency, differential GPS, dynamic surveys will be discussed herein. Note that for all processing options that are not immediately relevant to this application were set to their pre-defined defaults. In all cases, dual frequency output from all satellites satisfying the cutoff angle restrictions were considered. The post-processing parameters defined in this study are detailed in the following sections.

11.6.1 Cutoff Angle

Observations from low elevation satellites can be problematic, as transmitted data can sometimes be lost and these satellites are more susceptible to ionospheric delays, necessitating the specification of a cutoff angle beneath which a satellite will no longer be considered a viable transmission source. In the post-processing for the tests listed in Table 11.3, a 15° cutoff angle was selected. This implies that all surrounding obstructions will be beneath the cutoff angle and only satellites above this angle, free from obstruction and interference, are considered. The flexibility of the post-processing regimen allows this parameter to be adjusted if ambiguity checks on the processed data fail, in which case the angle can be increased and the data reprocessed. By neglecting more of the noisier, low-elevation satellites, the overall phase noise can often be improved. However, too much selectivity in this parameter reduces the number of viable satellites and can sacrifice GDOP, another important consideration. Observations indicated that with the exception of one test, this cutoff angle was sufficient.

11.6.2 Baseline Limit

There is practical limit on the baselines over which ambiguities in the GPS data can be resolved. The maximum value for this distance is conservatively specified as 8 km, well above the separation distance in this study's full-scale application. Note that the baseline for the calibration tests in Table 11.3 is essentially zero (0.0024 km), so this parameter has little consequence for the current discussion. The default value is normally taken as 20 km. For practical purposes, 30 km is the maximum reasonable value, since the signal delay through the ionosphere is different for the L1 and L2 frequencies, and this lag will pose a problem over larger baselines, necessitating a different protocol beyond the scope of this study.

11.6.3 RMS Threshold

This value represents a threshold for the noise in the phase measurements. In the case where the phase noise of the actual measurements exceeds this value, no attempt is made to resolve ambiguities. By default, this is set to automatic so that the system takes the duration of the observations into consideration when setting the threshold value. This may be set to manual in order to increase the threshold value and allow for more ionospheric or other noise and thereby force an ambiguity resolution, which may lead to significant errors when observations are over short durations. As most of the tests in Table 11.3 spanned only a number of minutes, the RMS threshold was set to automatic to insure that reasonable RMS thresholds were defined. The same practice is retained in full-scale application.

11.6.4 Solution Type

SKI-Pro provides the flexibility to choose a standard solution type or iono free fixed solution. The latter allows for backward processing to remove ionospheric disturbances over longer baselines. However, since the baselines in the calibration tests are virtually zero, the standard solution will be used. In the full-scale application, the selection of the iono free fixed solution is warranted to reduce ionospheric disturbances. The resulting solutions will be flagged to verify if ambiguities were successfully resolved: “yes” indicating that they were, “yes*” indicating that they were resolved but there may be some residual uncertainty, or “no” indicating that the resolution was not successful. Note that only data flagged as “yes” are retained for analysis.

11.6.5 Ionospheric Modeling

As discussed previously, the ionosphere causes a signal path delay, which can sometimes amount to errors of several tens of meters in the estimate of pseudorange. During periods of even minimal solar activity, baseline errors of up to several parts per million (see Table 11.1) are attributed to the delay experienced by the signal as it passes through the ionosphere. Therefore, an appropriate ionospheric model must be chosen to correct for these errors. The following models for the ionosphere are available in SKI- Pro:

1. **Automatic (Default):** SKI-Pro is allowed designate one of the five model choices automatically, based on the duration of data and availability of almanac files.
2. **No model:** Whether chosen automatically or manually, this implies a period of low atmospheric activity for which no corrections are needed.

3. **Standard:** This model is more representative of a period with increasing ionospheric activity, which follows an 11-year cycle with its last peak in 1991. The standard model is a single layer model with specific assumptions on the total amount of electrons and their distribution within this layer. Based on this model, an ionospheric path delay is computed at each epoch for each satellite.

4. **Computed model:** SKI-Pro calculates a customized ionospheric model when at least 45 minutes of dual frequency data are available at the reference station. Selection of this model is advantageous, since it is computed in accordance with conditions prevalent at the time and position of observation. This strategy is attractive for full-scale applications when at least 45 minutes of data is available.

5. **Global / Regional model:** An imported regional model may also be used, if available.

6. **Klobuchar model:** Whenever less than 45 minutes of observation data are available at the reference, this model can be used as an alternative to the standard model. It reflects the 11-year cycle of solar activity particularly well and can be advantageous during the time of high solar activity. The Klobuchar model should only be selected if raw observation data from Leica receivers is being used in the post-processing strategy, since this kind of data contains the necessary almanac files used in this model.

Thus, a number of issues must be considered when choosing an ionospheric model, including the level of high solar activity and the duration of the observation period. Since the data imported into SKI-Pro will always be in raw LB2 format, the

necessary almanac files for the Klobuchar model will always be available. In the case of the calibration tests in Table 11.3, the short duration of the observations and the negligible baseline eliminate the need for ionospheric modeling, warranting the selection of “No Model.” However, in full-scale applications, baseline separation may require some ionospheric modeling, especially since the monitoring period falls within the peak interval for solar activity. Therefore, the computed model will be used when sufficient amounts of data are available. Otherwise, the Klobuchar model is appropriate.

11.6.6 Stochastic Modeling

This step supplements the ionospheric modeling by assessing the ionospheric impact at each time step. This added measure may be useful for ambiguity resolution when the ionosphere is quite active and the baseline distance is considerable. This strategy can be problematic over shorter baselines, since low quality data, influenced by multi-path or obstructions, may be misinterpreted as being influenced by ionospheric noise and inappropriately corrected. To insure that short baselines are not stochastically modeled, the default value for the minimum distance set to 10 km and the level of ionospheric activity is set to medium. As the baselines at both the Anderson site and in the full-scale application will not exceed this value, stochastic modeling is never used.

11.6.7 Tropospheric Modeling

As discussed in Chapter 10, the lower atmosphere also causes a delay in the receipt of signals from the satellites. To compute this delay, the behavior of the refractive index for the troposphere must be known. Various models exist (all based on information of

pressure, temperature and relative humidity of the reference station) to allow computation of this path delay. If a model is desired, one of the following may be chosen: Hopfield (default), Simplified Hopfield, Saastamoinen and Essen & Froome. The differences that result from using different models are minor, though it is recommended that the same model be adopted uniformly for all measurements taken in a given area. The Hopfield model is retained in this study.

11.6.8 Single Point Positioning

Similar to the self-survey discussed previously, single point positioning (SPP) option can be selected to use the measurements collected at a single station during one or more occupations to process an absolute position in the WGS84 coordinate system. This serves as a reliable technique to determine the absolute position of the reference or rover station prior to monitoring. While the self-survey is sufficient for the tests listed in Table 11.3, a true position may be processed in this way prior to dynamic monitoring. However, due to the flexibility of the rover structure, a static position is difficult to obtain through single point processing, therefore, a baseline position is obtained by determining the mean of numerous observations collected at night, when static displacements due to thermal effects are not prevalent, and during times of low wind speeds, in order to get a reference, static position of the structure. This baseline position can then be subtracted from the displacement outputs from the GPS to identify the relative displacements.

11.7 Interpretation of Results

Following post-processing using the aforementioned parameters, the output of the SKI-Pro system is translated automatically from the global WGS84 coordinate system and into a local coordinate system for the area. The Transverse Mercator Projection, discussed in more detail in Leica (1999) was used in this study to transform the Anderson test site data into the local coordinate system: Indiana West NAD 83. The displacements can then be viewed in terms of motion relative to the North-South and East-West axes. An example of the processed output is provided in Figure 11.12. Note that the coordinates are defined in terms of absolute north and east positions in units of meters. In order to easily track relative motions, the coordinates in columns 4 and 5 of Figure 11.12 are subtracted from the baseline position described in Section 11.6.8, or more simply by subtracting the mean of the static component of the GPS data before the shake table was set into motion. The elevation data in column 6 was of no interest in this study.

Note that the SKI-Pro output also contains estimates of errors in the GPS data at each epoch. Columns 7-8 provide an estimate of the standard deviation of the GPS position estimate at that point in time based on the uncertainty in the satellite data (see Equation 10.13). This can be used to assess the quality of the position data. The data shown in this sample demonstrate that the uncertainty assigned to each position ordinate is on the order of 1-2 mm. The SRSS combination of these measures yields the overall position quality measure in column 10. Similar reliability measures are also provided for the elevation. In addition, a log file summarizes the parameters of the GPS data and

Point Id	Epoch	Arb. Status	E [m]	N [m]	Elev. [m]	Sd.N [m]	Sd. E [m]	Sd. Elev. [m]	Posn. Qty [m]	Elev. Qty [m]
ROVR0122_1819507	01/22/2002 13:19:51	yes	983160.69	721387.27	657.7595	0.0018	0.0013	0.0044	0.002	0.004
ROVR0122_1819508	01/22/2002 13:19:51	yes	983160.69	721387.27	657.7624	0.0023	0.0017	0.0056	0.003	0.006
ROVR0122_1819509	01/22/2002 13:19:51	yes	983160.69	721387.27	657.7624	0.0018	0.0014	0.0044	0.002	0.004
ROVR0122_1819510	01/22/2002 13:19:51	yes	983160.69	721387.27	657.7573	0.0013	0.001	0.0032	0.002	0.003
ROVR0122_1819511	01/22/2002 13:19:51	yes	983160.69	721387.26	657.7556	0.0013	0.0009	0.003	0.002	0.003
ROVR0122_1819512	01/22/2002 13:19:51	yes	983160.69	721387.27	657.758	0.0018	0.0013	0.0043	0.002	0.004
ROVR0122_1819513	01/22/2002 13:19:51	yes	983160.69	721387.26	657.7579	0.0021	0.0016	0.0051	0.003	0.005
ROVR0122_1819514	01/22/2002 13:19:51	yes	983160.69	721387.26	657.7563	0.0018	0.0013	0.0044	0.002	0.004
ROVR0122_1819515	01/22/2002 13:19:51	yes	983160.69	721387.26	657.7583	0.0014	0.001	0.0034	0.002	0.003
ROVR0122_1819516	01/22/2002 13:19:52	yes	983160.69	721387.26	657.7537	0.0021	0.0016	0.0051	0.003	0.005
ROVR0122_1819517	01/22/2002 13:19:52	yes	983160.69	721387.26	657.7557	0.0013	0.001	0.0032	0.002	0.003
ROVR0122_1819518	01/22/2002 13:19:52	yes	983160.69	721387.26	657.7549	0.0017	0.0013	0.0042	0.002	0.004

FIGURE 11.12. Sample SKI-Pro output (screen capture from Leica software)

tracks the PDOP and GDOP as well as the position of each satellite being tracked at each epoch.

11.8 Summary

This chapter overviewed the hardware and software components and the configurations necessary to perform a series of calibration studies for a Leica MC500 GPS system. The following chapter will discuss in more detail the analysis of the acquired data and the performance of the system as determined through the aforementioned tests in Table 11.3.

CHAPTER 12

GLOBAL POSITIONING SYSTEM CALIBRATION TEST RESULTS AND DISCUSSION

12.1 Introduction

In the previous chapter, a Global Positioning System configuration was overviewed and a series of calibration tests were discussed. The results of these tests will be summarized in the subsequent sections, in which the relative displacements measured by the GPS units along the N-S axis are defined as ΔN and those along the E-W axis are defined as ΔW .

12.2 Verification of Background Noise and Influence of Satellite

Position: Results

The examination of static data gives an indication of the background noise in GPS measurements, as any displacement detected for a stationary body is representative of the background noise in the GPS data and a direct indicator of the accuracy limitations of the system. As discussed in Section 11.5.1, three sets of static measurements were conducted at three different times of day, resulting in variable PDOP and GDOP. These values are provided in Table 12.1. As shown previously in Figure 11.7, 6 satellites were anticipated

TABLE 12.1

SATELLITE CONDITIONS AND DOP ERRORS FOR STATIC TESTS

Test	Test Duration	No. Satellites	GDOP	PDOP
1a	9:22 - 9:33	7	2.9-3.1	2.5-2.6
1b	12:57 - 13:07	7	2.7-2.8	2.3-2.4
1c (I)	15:29:17 - 15:32	7	2.0	1.7-1.8
1c (II)	15:32 - 15:41	6	2.6-2.7	2.3

to be in view at the Anderson Road site for the duration of Test 1c, when in actuality, 7 satellites were initially in full view above the mask angle condition. Midway through the test, this additional satellite was lost and the six satellites predicted to be available remained. Though predictive tools are certainly helpful in determining the quality of satellite conditions throughout the day, these only approximately estimate the visibility of satellites at a given location. A comparison of Table 12.1 and Figure 11.7 for each test reveals that the predicted satellite availability and DOP errors are not always consistent. In fact, the predicted PDOP values for these static tests were quite lower than what was observed in the field.

As discussed in Chapter 10, satellite configuration has some influence on the accuracy of GPS systems. This is demonstrated in Table 12.1 for Test 1c, which experienced an increase of both PDOP and GDOP after one of the satellites was lost from view. The significance of the increased DOP can be determined by examining the statistics of the static time histories for each case, provided in Table 12.2. First examining Test 1a and 1b, the mean values were found to be approximately zero (on the order of 10^{-7} to 10^{-6} cm), with standard deviations between 1.5 and 2 mm. According to the manufacturer's specifications, shown earlier in Table 11.1, static accuracies of the system

should be 3 mm for near zero baselines, illustrating that the system was found to perform better than expected. The variability in the background noise of the system was capable of producing spurious displacements from 6 to 9 mm. The standard deviation of Test 1c did not experience a marked increase as a result of the loss of a satellite. In fact, referring back to Table 12.1, even for Test 1c (II), despite the loss of a satellite, the overall GDOP is smaller than Tests 1a and 1b, reiterating that satellite orientation quality and not quantity is most critical in defining DOP values. However, the standard deviation (std) of the static test data in Test1c, despite the superior GDOP for this test, is slightly larger, between 2 and 2.5 mm but still within the manufacturer's specifications. Thus it is apparent that for reasonable GDOP values between 3 and 4, satellite orientation does not have a significant influence on GPS accuracy.

However, examining the means of Test 1c in Table 12.2, it is evident that a slight mean offset is detected, more significantly in the first phase of the test. In general, GPS static tests can have low-frequency drifts of relatively small amplitude, as evident by a closer inspection of the time histories in Figure 12.1. In the case of Test 1b, a slight bias toward the positive East in the first 30 seconds, is apparent, though in the average, the mean of the signal tends to zero. This is more marked in the case of Test 1c (I) where the GPS data manifests a positive eastern bias through the first 100 seconds, followed by a general negative bias in the later stages of the time history. Similarly, there is a marked positive northern bias later in the signal, resulting in the non-zero means in Table 12.2. The potential for low frequency, low amplitude trends in GPS data is apparent from these time histories, indicating that any static or pseudo static relative displacements of under ± 0.5 cm may not be physically meaningful, but a consequence of this phenomenon. Note

TABLE 12.2

STATISTICS OF GPS STATIC DISPLACEMENTS

Test	ΔE [cm]				ΔN [cm]			
	min	max	mean	std	min	max	mean	std
1a	-0.638	0.612	0.000	0.156	-0.672	0.808	0.000	0.193
1b	-0.700	0.810	0.000	0.186	-0.745	0.895	0.000	0.208
1c*	-0.991	0.819	0.000	0.202	-0.720	0.870	0.000	0.229
1c (I)	-0.991	0.819	0.029	0.242	-0.660	0.870	0.065	0.256
1c (II)	-0.681	0.669	-0.010	0.190	-0.720	0.740	-0.026	0.211

*Based on total duration of Test 1c.

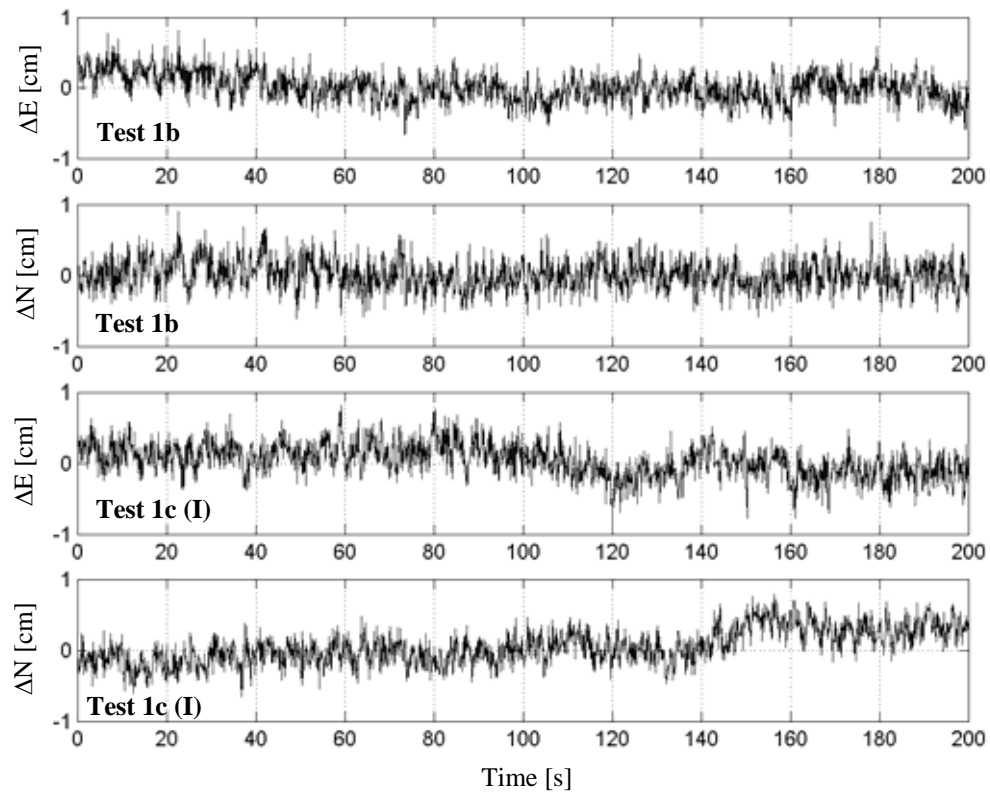


FIGURE 12.1. Portion of time history of GPS relative displacement for static tests Test 1b and Test 1c

it assumed that these low frequency trends are not the result of multi-path error, since no reflective surfaces and significant neighboring buildings in the field test site. As shown in Figure 12.2, the positions are plotted to reveal any directional bias in the data. Test 1a and Test 1c (II) demonstrate a classical circular shape, indicating that equivalent accuracy levels in both directions. However, Test 1b and 1c (I) manifest an elliptical shape indicating the biases resulting from the low frequency trends discussed previously. These figures also display the standard deviations predicted by the manufacturer in comparison to those observed in testing, reiterating that even in the noisiest of the three tests (Test 1c (I)), the standard deviation of the background noise was within the accuracy limits defined by Leica.

12.2.1 Probability and Spectral Structure of Background Noise

Figures 12.3 and 12.4 display the probability density function (PDF) and power spectral density (PSD) of the N-S and E-W displacements obtained from the measured background noise for each of the three static tests. Using the mean and standard deviation listed Table 12.2, the resulting Gaussian distribution is also shown by the thin lines on the PDFs in Figure 12.3. The vertical dotted lines mark 1, 2 and 3 standard deviations of the mean. The PDFs reveal that although the distribution of the background noise is symmetric about a zero mean, it is non-Gaussian in nature. However, in the tail regions, the Gaussian distribution provides a conservative measure of the spread of the background noise, capturing the majority of the background noise levels within 3 standard deviations of the mean. This is verified by examining the upper and lower 99.7th percentile confidence limits on the GPS displacement data and comparing those to a

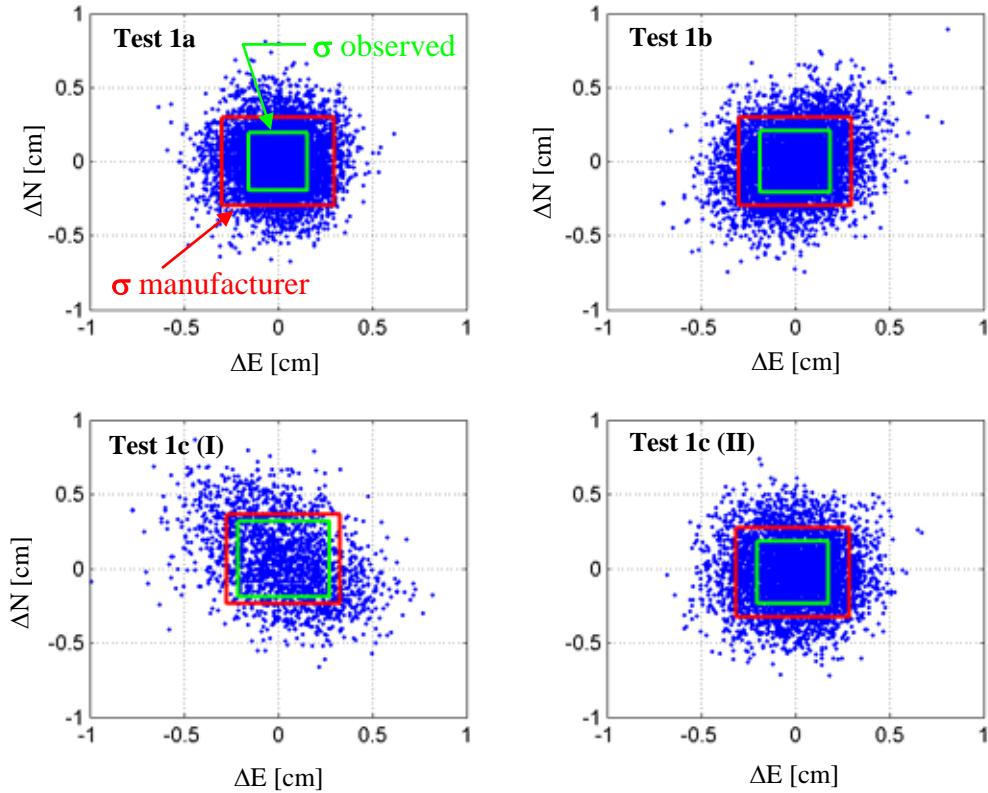


FIGURE 12.2. Results from static tests and comparisons between observed RMS displacement (inner box) and manufacturer's prediction (outer box)

Gaussian distribution, as shown in Table 12.3. The Gaussian limits conservatively confine over 99% of the background noise within this range. Since it is this spread of the distribution, particularly in the tail regions, that is most concerning when attempting to quantify the extent of background noise, this simple demonstration verifies that the Gaussian assumption is adequate to conservatively estimate distribution of the background noise. Note that in Equation 10.13 the quality of GPS position estimates are quantified using a standard deviation measure. This practice assumes that confidence ellipses, centered at the two-dimensional estimated position, can be defined. The probability of the actual position lying within an ellipse measuring 1 standard deviation is

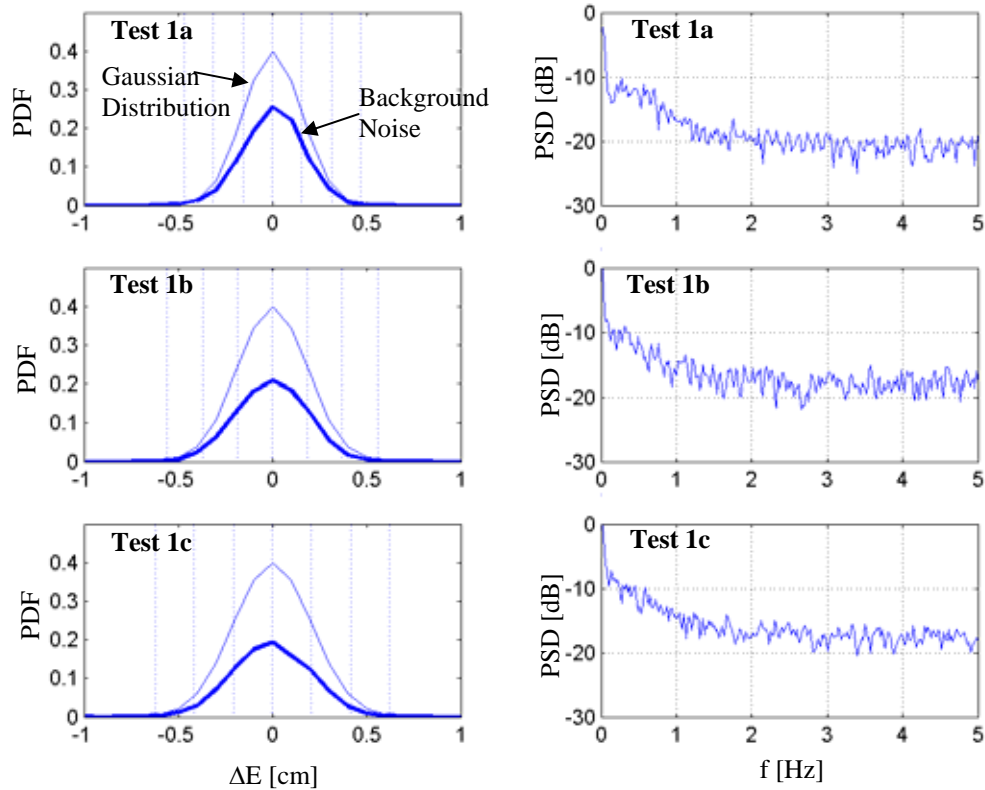


FIGURE 12.3. Probability density (compared to Gaussian function with same mean and standard deviation) with vertical bars denoting 1, 2 and 3 standard deviations of the mean, and power spectral density for each of the static tests in Test 1 series, E-W component

68.3%. Similarly, within 2 standard deviations the probability is 95.5% and within 3 standard deviations is 99.7%. This implies the assumption of Gaussianity, which appears conservatively justified from the discussions herein.

An examination of the PSDs of each test verifies the generally broadband nature of the background noise in GPS displacement measurements. The noise threshold is elevated from DC to approximately 2 Hz, reiterating the aforementioned low-frequency mean trends. The strong DC component is further evidence of the offsets observed in Figure 12.1, particularly larger for Test 1c. Therefore, when tracking motions less than 2

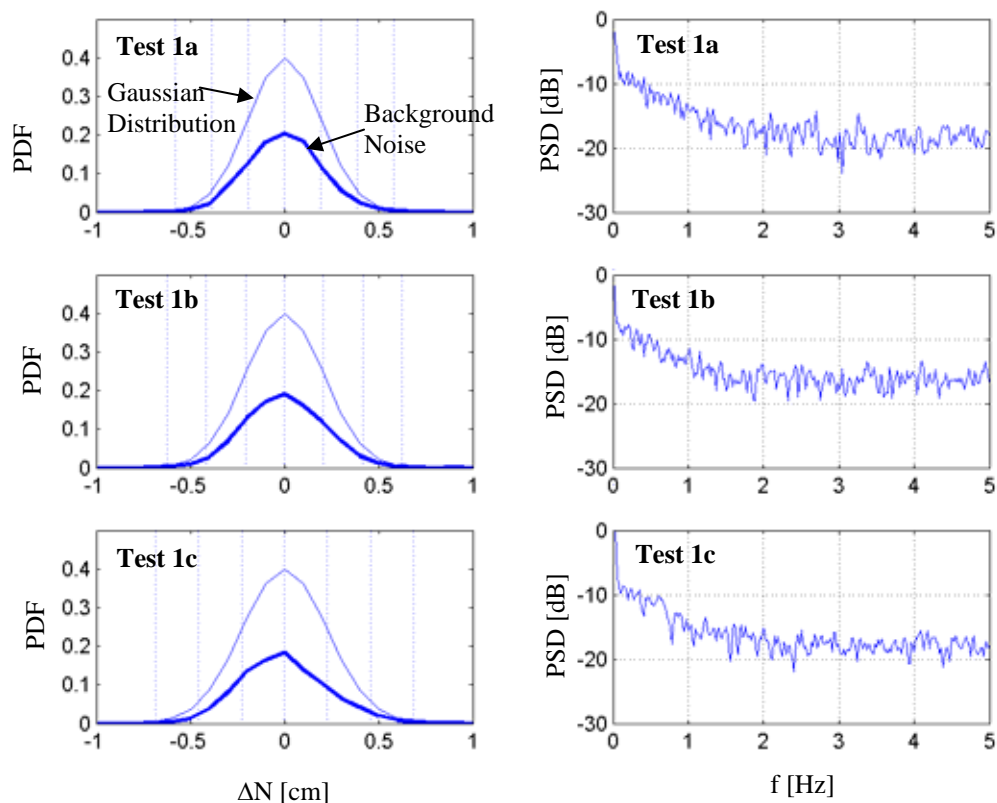


FIGURE 12.4. Probability density (compared to Gaussian function with same mean and standard deviation) with vertical bars denoting 1, 2 and 3 standard deviations of the mean, and power spectral density for each of the static tests in Test 1 series, N-S component

TABLE 12.3

COMPARISON OF 99.7TH PERCENTILE CONFIDENCE LIMITS OF GPS BACKGROUND NOISE WITH THOSE OF GAUSSIAN DISTRIBUTION

	ΔE [cm]		ΔN [cm]	
	Actual	Gaussian	Actual	Gaussian
Test 1a	(-0.458, 0.402)	(-0.467, 0.467)	(-0.522, 0.558)	(-0.580, 0.580)
Test 1b	(-0.510, 0.510)	(-0.558, 0.558)	(-0.565, 0.585)	(-0.624, 0.624)
Test 1c	(-0.581, 0.589)	(-0.621, 0.621)	(-0.570, 0.660)	(-0.686, 0.686)

Hz, the presence of these low frequency noise trends should be considered, while additional higher frequency noise may be removed by low-pass filtering.

12.2.2 Additional Information from Static Component of Dynamic Tests

It is difficult to determine the influence of GDOP from the aforementioned three static tests, as they were all conducted under periods of acceptable GDOP (< 4). Fortunately, each of the dynamic tests listed in Table 11.3 provide additional static information. As the direction of shaking in all of these tests, with the exception of Test 5, was along the North-South axis, any GPS estimate of motion along the East-West axis provides a running measure of the background noise in the measurements. Table 12.4 lists these background noise statistics, with each instance where the GDOP exceeded 4 shown in bold. Again, the mean values throughout are essentially zero, with the exception of the tests conducted on the second day of testing, due to a slight modification in the post-processing protocol. Still, the residual mean components in these cases are all less than 1 mm. Examining Table 12.4, it is evident that the background noise never exceeded ± 1 mm, in terms of peak value, and maintained RMS values less than 3 mm, as predicted by the manufacturer. Further, these supplementary data permit a detailed examination of the influence of GDOP on the level of background noise. This is quantified by the standard deviation of the GPS displacements in the E-W (static) direction during these dynamic tests, as shown in Equation 10.13 and is provided in Figure 12.5. The figure affirms that while there is a general tendency for large GDOP values to result in higher levels of background noise, degrading the accuracy of the GPS system, there is significant scatter. Particularly for GDOP values between 2-3, it becomes apparent that a number of

TABLE 12.4

STATISTICS OF E-W (STATIC) DIRECTION IN DYNAMIC TESTS

Test	No. of Satellites	PDOP	GDOP	mean [cm]	std [cm]	min [cm]	max [cm]
2a	7	4.2-4.3	5.1-5.2	-9.53E-08	0.1659	-0.5939	0.6461
2b	8,7	2.1-2.4	2.7-3.2	1.67E-07	0.1873	-0.6856	0.6244
2c	7	2.5-2.6	3.1	3.20E-07	0.2095	-0.7646	0.9554
2d	7	2.5	3	-6.48E-09	0.232	-0.6547	0.9053
2e	7	2.5	3	-1.56E-08	0.1951	-0.5773	0.6327
2f	7	2.4-2.5	2.9	1.29E-07	0.2146	-0.7198	0.6802
2g	7	2.4	2.9	-9.93E-08	0.2617	-0.7371	0.6929
2h	7	2.4	2.8-2.9	-5.72E-08	0.2133	-0.7971	0.6229
2i	7	2.4	2.8	-9.80E-08	0.2383	-0.7368	0.6032
2j	7	2.4	2.8	-3.71E-08	0.1722	-0.5197	0.4703
2k	7	2.4	2.8	1.46E-08	0.1618	-0.5227	0.4573
2l	7	2.4	2.8	1.32E-07	0.2179	-0.8619	0.5181
2m	7	2.4	2.9	1.57E-07	0.1762	-0.5854	0.4646
2n	7	2.4	2.9	-5.56E-08	0.1812	-0.5231	0.6569
2o	7	2.4-2.5	2.9	6.33E-08	0.2162	-0.6301	0.5899
2p	7	2.5	2.9	-8.46E-11	0.1945	-0.6466	0.6634
2q	7	2.5	2.9	-1.12E-07	0.1811	-0.5633	0.5167
2r	7	2.5	2.9	5.72E-08	0.2029	-0.5658	0.6542
2s	7,6	1.7-2.8	2.0-3.3	-0.0662	0.1963	-0.9764	0.6936
2t	6	4.7	5.8	-1.19E-07	0.2384	-0.8168	0.7332
2u	6	4.7	5.8	-2.03E-08	0.2738	-0.693	1.017
2v	6	4.7	5.8	1.23E-08	0.2802	-0.8594	0.7306
2w	6	4.7	5.8	-3.66E-08	0.2796	-0.7235	0.8865
3a	6	4.6	5.6-5.7	-8.86E-08	0.2683	-0.9146	0.8354
3b	6	4.3-4.4	5.2-5.3	-4.31E-08	0.2475	-1.0407	0.7493
3c	7	3.2-3.3	3.8-3.9	4.43E-07	0.2788	-0.8759	1.0141
3d	7	1.8-2.9	2.0-3.4	4.11E-07	0.3009	-0.9099	0.9601
3e	6,5	2.1-2.9	2.4-3.3	0.0925	0.2002	-0.7405	0.9295
3f	6	2.2-2.3	2.6-2.7	0.1695	0.2137	-0.6953	1.0947
4a	6	2.4-2.8	2.8-3.1	0.0312	0.1711	-0.6190	0.6410
4b	7	2.3-2.4	2.7-2.8	-0.0224	0.1657	-0.5782	0.5618
4c	7,6	2.7-3.4	3.0-4.0	0.0862	0.1966	-0.6052	0.8048
6a	8,7	1.9-2.2	2.1-2.5	-0.0803	0.1991	-0.8273	0.6027
6b	7,6	2.2-3.5	3.5-4.3	-0.0484	0.2241	-0.9909	0.8091

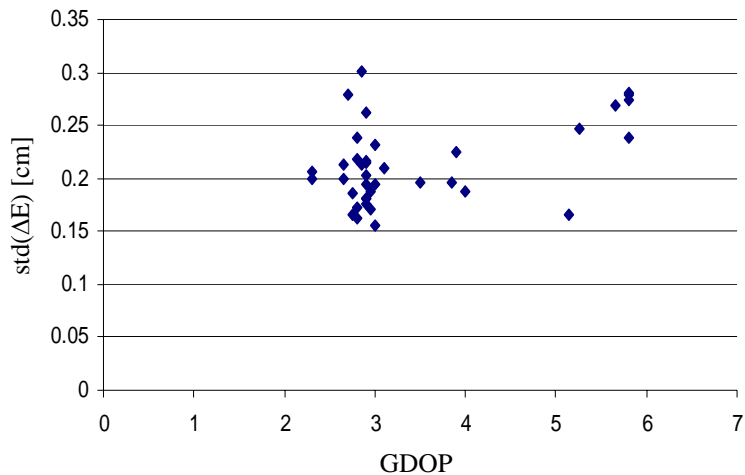


FIGURE 12.5. Standard deviation of background noise along E-W direction, (static) for all tests, as a function of GDOP

additional factors beyond GDOP influence the level of background noise in the displacement estimates. Still, the standard deviation values tend to cluster at lower levels for $GDOP = 3$, indicating some influence of satellite orientation and reiterating the importance of measurement during periods of the lowest GDOP possible in at least helping to minimize the inherent errors in the system.

12.3 Accuracy Estimates

In the case of static testing, the level of background noise is readily quantified through the statistical measures provided in Table 12.2. Even in the dynamic tests conducted as part of this study, the use of the static component measured in the E-W direction, as discussed in 12.2.2, provides a running check on the level of background noise throughout testing. However, in practical applications, motion may be simultaneously

occurring along an axis not aligned with true North or East, leading to components of motion in both directions of GPS displacement. Therefore, the use of statistics from the static components of dynamic tests is not completely viable in all situations. However, in the post-processing regimen to solve for ambiguities, a statistical measure of the accuracy of GPS measurements is provided at each epoch. As shown previously in Figure 11.17, the GPS positions are accompanied by a standard deviation measure along the North axis σ_N and the East axis σ_E , quantifying the level of potential error in that calculated position. These two measures are combined by the SRSS rule, to define an overall horizontal position quality (PQ) measure at each epoch of GPS measurement. The larger these values, the more the uncertainty in the GPS position estimate. In the case of the static tests, it was demonstrated that, using the conservative assumption of a Gaussian distribution, over 99% of the background noise could be captured within three standard deviations. In the case of dynamic tests, this information is not available; therefore it is proposed to use the standard deviation of the position estimates (σ_N and σ_E) in its place to accomplish the same goal. As the standard deviation of position estimates is available at each epoch, this will yield a time-varying noise threshold Δ_{noise} that will be used to quantify the reliability of GPS estimates, according to

$$\Delta_{noise} = [-3\sigma(t), 3\sigma(t)] \quad (12.1)$$

where $\sigma = \sigma_N$ or σ_E depending on the direction being analyzed. For comparative purposes, the standard deviation of the static component of each test is provided in Table 12.5. This is compared to the average standard deviation of the position estimate in each direction. Note again that the standard deviation of the position estimate, and thereby the

TABLE 12.5

STANDARD DEVIATION OF GPS STATIC DISPLACEMENTS COMPARED TO
AVERAGE OF STANDARD DEVIATION IN GPS DISPLACEMENT ESTIMATE

Test	E-W		N-S		avg(PQ)
	std	avg(σ_E)	std	avg(σ_N)	
1a	0.156	0.129	0.193	0.165	0.209
1b	0.186	0.134	0.208	0.179	0.224
1c	0.207	0.195	0.229	0.198	0.278
2a	0.166	0.125		0.193	0.230
2b	0.187	0.167		0.180	0.246
2c	0.210	0.176		0.179	0.251
2d	0.232	0.178		0.180	0.253
2e	0.195	0.174		0.176	0.248
2f	0.215	0.171		0.173	0.243
2g	0.262	0.175		0.177	0.249
2h	0.213	0.175		0.177	0.248
2i	0.238	0.169		0.171	0.240
2j	0.172	0.134		0.180	0.224
2k	0.162	0.125		0.168	0.210
2l	0.218	0.126		0.169	0.211
2m	0.176	0.120		0.162	0.201
2n	0.181	0.124		0.168	0.209
2o	0.216	0.131		0.177	0.220
2p	0.195	0.130		0.177	0.219
2q	0.181	0.123		0.167	0.207
2r	0.203	0.122		0.166	0.206
2s	0.1963	0.1609		0.2583	0.3045
2t	0.238	0.137		0.227	0.265
2u	0.274	0.137		0.225	0.263
2v	0.280	0.149		0.240	0.283
2w	0.280	0.173		0.273	0.323
3a	0.268	0.175		0.265	0.317
3b	0.248	0.215		0.291	0.362
3c	0.279	0.222		0.240	0.327
3d	0.301	0.192		0.187	0.268
3e	0.2002	0.1513		0.1645	0.2235
3f	0.2137	0.1547		0.1744	0.2332
4a	0.1711	0.1426	0.3013	0.2249	0.2662
4b	0.1657	0.157	0.2152	0.2116	0.2635
4c	0.1966	0.1346	0.2272	0.1694	0.2163
6a	0.1991	0.202	0.2843	0.2434	0.3163
6b	0.2241	0.2237	0.2689	0.2521	0.3373

position quality, is time-varying and a direct result of the inaccuracies anticipated in the calculated GPS displacements. As such it is perhaps best geared to define noise analysis thresholds, even more so than the statistics of the static tests. Note that the position quality measure is also provided in Table 12.5. It is often convenient to examine PQ as it combines the uncertainty in both horizontal displacement estimates. An example of the PSD and PDF of the position quality measure is shown in Figure 12.6. Note that aside from the DC component, reflective of the mean value, the PQ is broadband in nature and does not reflect any distinct periodic tendency, even for the dynamic test case whose frequency of motion was 0.2 Hz. Therefore, it can be assumed that PQ is independent of the characteristics of the motion undertaken by the GPS antenna. The distribution of position quality is also non-Gaussian with a slight skew towards the low side of the mean. Its distribution is compared to the Gaussian distribution that is obtained using the mean and standard deviation of PQ over the duration of Test 1a. The influence of GDOP on position quality is shown in Figure 12.7. To simplify the analysis, the average PQ for each test is plotted as a function of the average GDOP over the duration of that test. Though these are only averaged quantities, the trends indicate that GDOP increases lead to greater uncertainties in GPS positions, quantified through the position quality measure, as expected. The scatter in the data further reiterates the observations in Figure 12.5 – additional factors beyond GDOP contribute to the degradation of GPS accuracy.

A demonstration of the insights that can be gained by using these time varying noise thresholds is provided in Figure 12.8. The top six images show the noise thresholds enveloping the displacements recorded during static testing, indicative of background

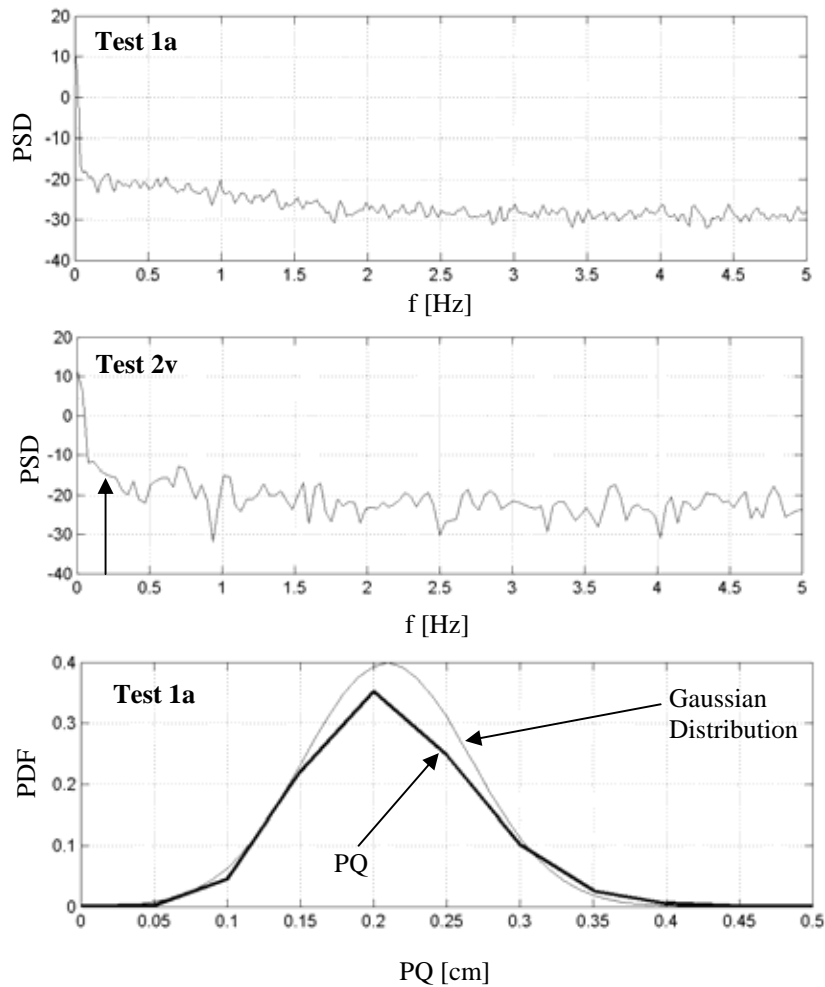


FIGURE 12.6. Spectral structure of position quality measure for Test 1a and Test 2v, along with probability distribution for Test 1a

noise levels. By using the formulation in Equation 12.1, the error thresholds, with the exception of a few spikes, conservatively define the upper and lower limits of the background system noise. Even in the presence of local mean trends that shift the background noise levels, as shown by the northern component in Test 1c, the noise thresholds are not fully surpassed. In the lower six images, dynamic test results are also examined. While the eastern component is static with much similarity to the images from

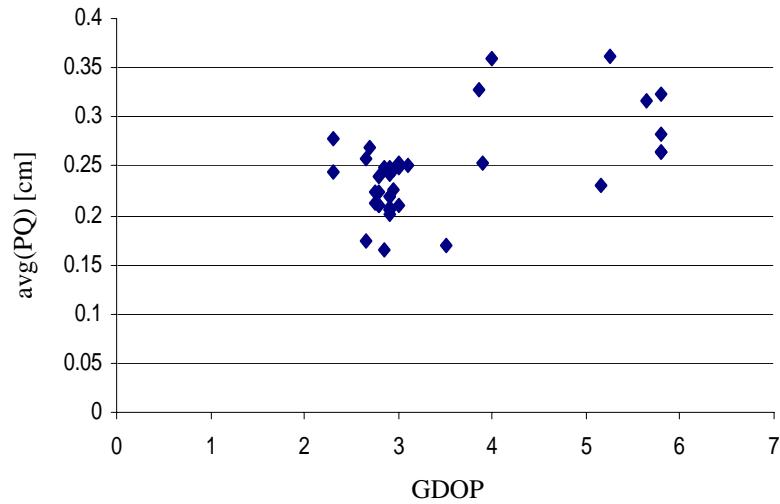


FIGURE 12.7. Average position quality as a function of GDOP

the Test 1 series, the dynamic tests on the right demonstrate that the quality of GPS displacement data is compromised when the signal amplitude is less than or equal to the noise threshold. The northern results for Test 2d reveals the difficulty of tracking a ± 0.5 cm sine wave, essentially buried in the inherent noise of the GPS system. However, as the amplitude increases in Tests 2j and finally Test 2v to ± 1 and ± 3 cm, the signal can be tracked far more accurately. Note that in the eastern component of Test 2v there is a trace of periodic motion at 0.2 Hz, indicating that the shake table was not directly aligned with true North and instead had a small component projected on the E-W axis. At lower amplitudes (Test 2d, 2j) this slight rotation of the shake table from the N-S axis is not even discernable.

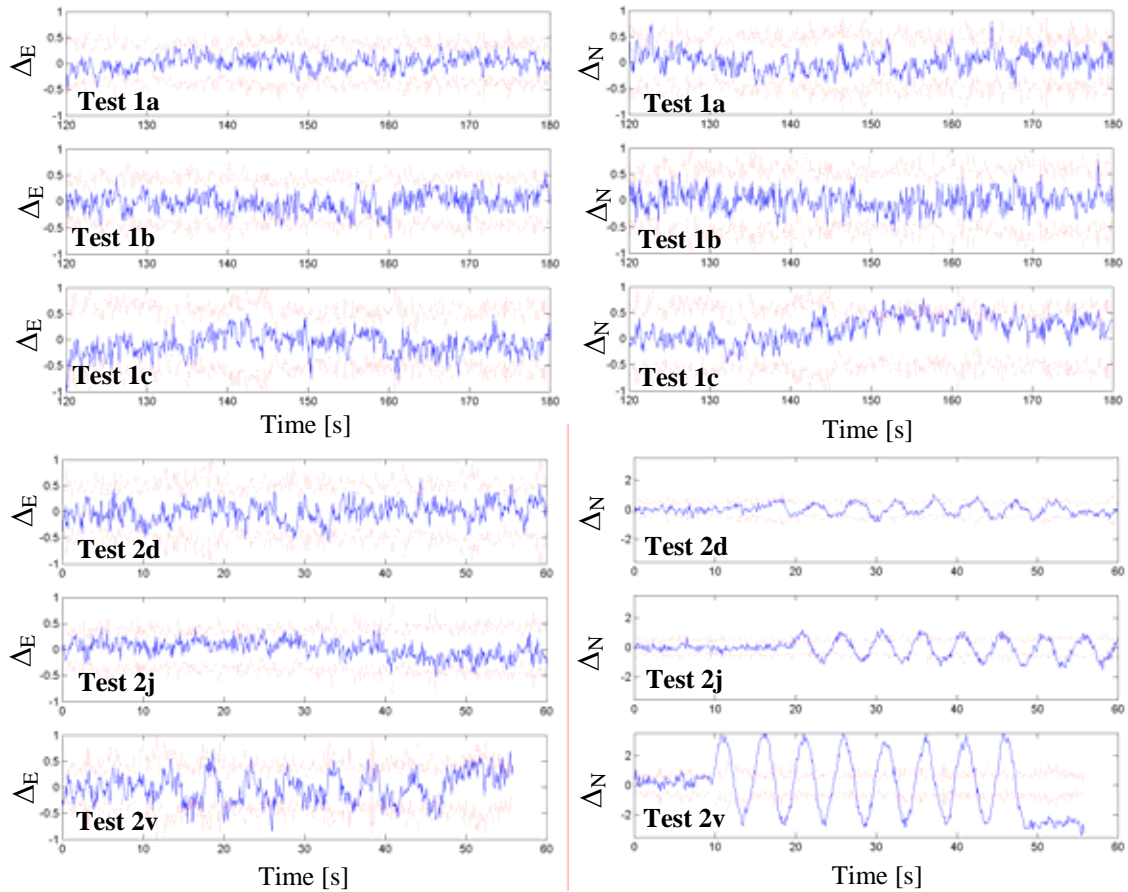


FIGURE 12.8. Examples of noise threshold levels (dotted) [cm] superimposed on GPS displacements [cm] for a series of static and dynamic tests

12.4 Data Preparation

Referring back to Figure 12.8, the results from the three dynamic tests shown in the lower right hand corner manifest an overlay of high frequency noise, even at amplitudes above the noise threshold (Test 2v). As demonstrated in Figure 12.4, the background noise of the system is particularly concentrated between DC and 2 Hz, which includes the frequency (0.2 Hz) of the sine wave data shown in Figure 12.8. Another example of the relative GPS displacements, determined as described in Section 11.7, is provided in

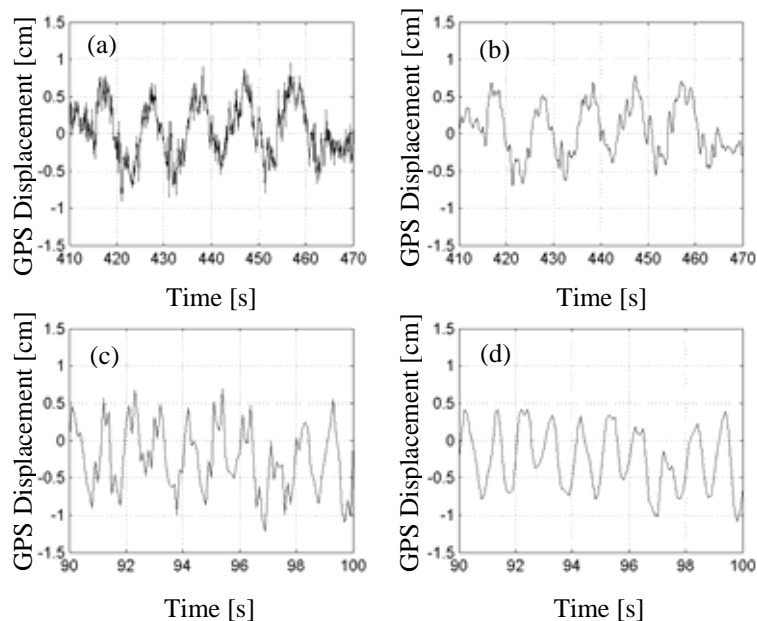


FIGURE 12.9. (a) Test 2a GPS displacement data; (b) Test 2a GPS displacement data after low-pass filtering; (c) Test 2e GPS displacement data; (d) Test 2e GPS displacement data after low-pass filtering

Figure 12.9a,c for two cases from the Test 2 series: Test 2a and 2e. For these two cases, the amplitude of motion (± 0.5 cm) is at the RMS accuracy limit of the GPS receiver, listed previously in Table 11.1 and falls beneath the noise threshold, which takes on an average value of ± 0.5406 cm for Test 2a and ± 0.5778 for Test 2e. Therefore, the signals being tracked are consumed by the background noise in the GPS system, as discussed in the previous section. This noise appears as an overlay of high frequency noise on the lower frequency signals being monitored, degrading the apparent quality of the GPS displacement data. In traditional data acquisition systems utilizing analog measurement devices, anti-aliasing filtering is incorporated, helping also to minimize the influence of high frequency noise in the measurements prior to their digitization. Though GPS data acquisition is a completely digital process, the incorporation of low-pass filtering

following the post-processing of GPS data can help to alleviate the influence of the high-frequency background noise component.

As a result, a second-order Chebyshev lowpass filter was implemented (0.1 dB of ripple in the pass band) in with three basic cut-off frequencies dependent on the maximum meaningful frequency f_{max} of the signal being analyzed. The various cut-off frequencies are listed in Table 12.6. Implementation of this filtering approach is shown in Figure 12.9b,d, enhancing to some extent the quality of the data. Affirmation of the performance of the filtering approach is provided by the PSDs in Figure 12.10. Though selecting an even lower cut-off frequency for the low-frequency signals may improve the quality of GPS data even further, there is potential risk of signal distortion. Therefore, the conservative cut-off frequencies in Table 12.6 were retained. This filtering approach was used for the analysis of each dynamic test result presented in subsequent sections.

TABLE 12.6
CHEBYSHEV FILTER CUT-OFF FREQUENCIES

Frequency Content of Signal	Filter Cut-Off Frequency
$f_{max} < 1 \text{ Hz}$	1 Hz
$1 \text{ Hz} < f_{max} < 2 \text{ Hz}$	3 Hz
$f_{max} < 2 \text{ Hz}$	5 Hz

12.5 Analysis of Dynamic Calibration Tests

The following sections will present the findings from Tests 2-3, the fully dynamic calibration tests which verify the performance of the GPS at varying amplitude levels,

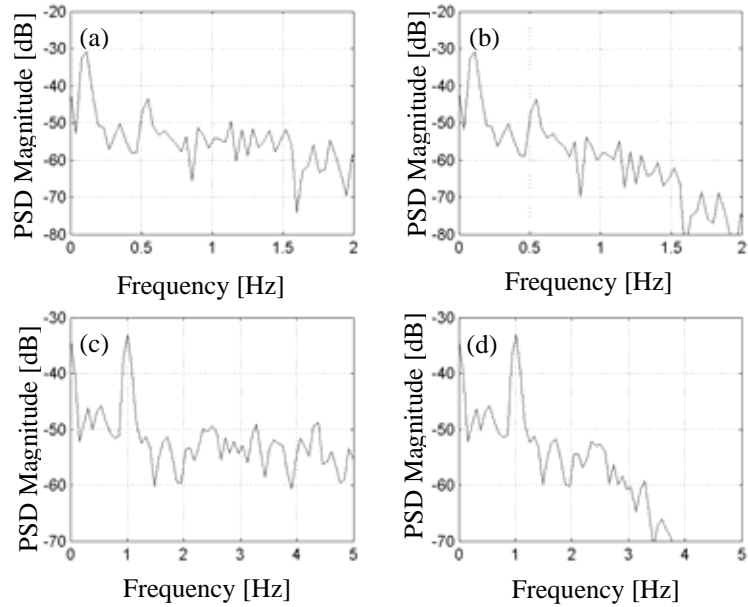


FIGURE 12.10. (a) PSD of Test 2a GPS displacement data; (b) PSD of Test 2a GPS displacement data after low-pass filtering; (c) PSD of Test 2e GPS displacement data; (d) PSD of Test 2e GPS displacement data after low-pass filtering

frequencies and waveforms. To provide a frame of reference for interpreting results, the noise threshold introduced in Section 12.3 is discussed simply in a mean sense to provide a quantitative measure of the background noise in the GPS measurements, which can be compared to the signal amplitude, much like the traditional signal-to-noise ratio. Table 12.7 lists the statistics of the standard deviation σ_N of the GPS position estimate of the north component, which was the designated axis of motion for all dynamic tests. The most meaningful quantity for the current discussion, the mean of this uncertainty measure, is marked in bold, and is consistently on the order of 2 mm. The standard deviation of this measure and the associated CoV reveals a significant level of variation in the uncertainty of the GPS position coordinate with time. By virtue of Equation 12.1,

TABLE 12.7

STATISTICS OF σ_N AND MEAN NOISE THRESHOLD

Test	σ_N					Mean Noise Threshold [cm]
	mean [cm]	std. [cm]	CoV [cm]	min [cm]	max [cm]	
1a	0.165	0.045	27%	0.040	0.380	±0.494
1b	0.179	0.050	28%	0.050	0.440	±0.538
1c	0.198	0.051	26%	0.040	0.430	±0.594
2a	0.193	0.058	30%	0.010	0.440	±0.578
2b	0.180	0.048	27%	0.050	0.400	±0.541
2c	0.179	0.051	29%	0.060	0.470	±0.537
2d	0.180	0.054	30%	0.070	0.380	±0.541
2e	0.176	0.047	26%	0.050	0.350	±0.528
2f	0.173	0.046	26%	0.050	0.370	±0.518
2g	0.177	0.047	27%	0.060	0.330	±0.532
2h	0.177	0.046	26%	0.070	0.370	±0.530
2i	0.171	0.046	27%	0.060	0.380	±0.512
2j	0.180	0.045	25%	0.070	0.380	±0.539
2k	0.168	0.045	27%	0.060	0.360	±0.505
2l	0.169	0.049	29%	0.060	0.340	±0.506
2m	0.162	0.047	29%	0.060	0.380	±0.485
2n	0.168	0.046	27%	0.060	0.340	±0.504
2o	0.177	0.051	29%	0.070	0.390	±0.530
2p	0.177	0.052	29%	0.000	0.420	±0.530
2q	0.167	0.046	28%	0.070	0.350	±0.500
2r	0.166	0.042	25%	0.070	0.370	±0.497
2s	0.258	0.081	31%	0.040	0.720	±0.775
2t	0.227	0.076	34%	0.060	0.710	±0.681
2u	0.225	0.075	33%	0.070	0.610	±0.674
2v	0.240	0.082	34%	0.080	0.560	±0.721
2w	0.273	0.093	34%	0.090	0.650	±0.819
3a	0.265	0.085	32%	0.090	0.560	±0.794
3b	0.291	0.085	29%	0.070	0.560	±0.874
3c	0.240	0.069	29%	0.060	0.530	±0.721
3d	0.187	0.054	29%	0.050	0.420	±0.561
3e	0.165	0.053	32%	0.030	0.460	±0.494
3f	0.174	0.055	31%	0.030	0.460	±0.523
4a	0.225	0.070	31%	0.040	0.570	±0.675
4b	0.212	0.059	28%	0.050	0.510	±0.635
4c	0.169	0.056	33%	0.040	0.460	±0.508
5	0.252	0.071	28%	0.080	0.580	±0.756
6a	0.243	0.059	24%	0.070	0.500	±0.730
6b	0.252	0.063	25%	0.070	0.570	±0.756

the mean noise threshold is defined in the last column of Table 12.7. As will be demonstrated by examples in the following sections, GPS cannot reliably track signals that are less than this threshold and ideally, one should only consider data obtained for displacements at least twice this mean noise threshold.

12.5.1 Test 2a-w: Verification of Amplitude Sensitivity

As discussed in Section 11.5.2, the experiments in Test 2 considered a series of sine waves with variable amplitude and frequency. The parameters of these tests were previously summarized in Table 11.3. Table 12.8 lists the standard deviation and peak values of the shaking table displacement (second row in each grouping) and compares these values to the GPS-measured displacements (first row in each grouping). The error in the estimate, defined as the GPS displacement estimate minus the table displacement, all normalized by the table displacement, is shown in the third row in each grouping. For additional insights, the mean noise threshold, shown previously in Table 12.7, is compared to the peak displacement of the table to form a signal-to-noise ratio. This measure is used to determine if the signal being tracked is of sufficient amplitude in comparison with the mean noise threshold predicted from the GPS post-processing calculations. Understandably, in the field, the true peak amplitude of a structure is not known, however, an approximation of this signal-to-noise ratio can similarly be provided using the resulting peak amplitude of the GPS measurements.

Figure 12.11 displays the results from Tests 2a-2f, a ± 0.5 cm sine wave of increasing frequency. The result shown in red is the shake table displacement and the

TABLE 12.8

ACCURACY OF GPS TRACKING FOR TEST 2

Test	ΔN [cm]				Noise [cm]	
		std	min	max		
2a	GPS	0.377	-0.426	0.368	Δ_{noise}	0.578
	TABLE	0.351	-0.490	0.491	x_{max}	0.491
	ERRORS	7%	-13%	-25%	S/N	85%
2b	GPS	0.365	-0.286	0.704	Δ_{noise}	0.540
	TABLE	0.352	-0.483	0.487	x_{max}	0.487
	ERRORS	4%	-41%	45%	S/N	90%
2c	GPS	0.359	-0.458	0.575	Δ_{noise}	0.537
	TABLE	0.352	-0.487	0.492	x_{max}	0.492
	ERRORS	2%	-6%	17%	S/N	92%
2d	GPS	0.358	-0.589	0.302	Δ_{noise}	0.540
	TABLE	0.351	-0.487	0.489	x_{max}	0.489
	ERRORS	2%	21%	-38%	S/N	90%
2e	GPS	0.370	-0.578	0.490	Δ_{noise}	0.528
	TABLE	0.352	-0.479	0.486	x_{max}	0.486
	ERRORS	5%	21%	1%	S/N	92%
2f	GPS	0.423	-0.556	0.467	Δ_{noise}	0.519
	TABLE	0.353	-0.491	0.490	x_{max}	0.490
	ERRORS	20%	13%	-5%	S/N	95%
2g	GPS	0.683	-0.871	0.806	Δ_{noise}	0.531
	TABLE	0.703	-0.987	0.982	x_{max}	0.982
	ERRORS	-3%	-12%	-18%	S/N	185%
2h	GPS	0.699	-1.077	0.785	Δ_{noise}	0.531
	TABLE	0.705	-0.989	0.993	x_{max}	0.993
	ERRORS	-1%	9%	-21%	S/N	187%
2i	GPS	0.645	-1.066	1.060	Δ_{noise}	0.513
	TABLE	0.705	-0.990	0.994	x_{max}	0.994
	ERRORS	-9%	8%	7%	S/N	194%
2j	GPS	0.670	-1.058	1.093	Δ_{noise}	0.540
	TABLE	0.704	-0.985	0.985	x_{max}	0.985
	ERRORS	-5%	7%	11%	S/N	183%
2k	GPS	0.691	-0.924	0.867	Δ_{noise}	0.504
	TABLE	0.708	-0.998	0.999	x_{max}	0.999
	ERRORS	-2%	-7%	-13%	S/N	198%
2l	GPS	0.803	-0.856	0.913	Δ_{noise}	0.507
	TABLE	0.714	-1.000	1.003	x_{max}	1.003
	ERRORS	12%	-14%	-9%	S/N	198%

TABLE 12.8 (CON'T)

Test	ΔN [cm]				Noise [cm]	
		std	min	max		
2m	GPS	1.324	-1.986	1.439	Δ_{noise}	0.486
	TABLE	1.410	-1.989	1.992	x_{max}	1.992
	ERRORS	-6%	0%	-28%	S/N	411%
2n	GPS	1.302	-1.407	1.678	Δ_{noise}	0.504
	TABLE	1.414	-1.990	1.991	x_{max}	1.991
	ERRORS	-8%	-29%	-16%	S/N	395%
2o	GPS	1.303	-1.929	1.738	Δ_{noise}	0.531
	TABLE	1.410	-1.988	1.993	x_{max}	1.993
	ERRORS	-8%	-3%	-13%	S/N	376%
2p	GPS	1.268	-1.937	1.466	Δ_{noise}	0.531
	TABLE	1.409	-1.987	1.986	x_{max}	1.986
	ERRORS	-10%	-3%	-26%	S/N	375%
2q	GPS	1.377	-1.775	2.134	Δ_{noise}	0.501
	TABLE	1.415	-1.985	1.998	x_{max}	1.998
	ERRORS	-3%	-11%	7%	S/N	400%
2r	GPS	1.042	-1.073	1.406	Δ_{noise}	0.498
	TABLE	0.983	-1.490	1.459	x_{max}	1.459
	ERRORS	6%	-28%	-4%	S/N	294%
2s	GPS	1.925	-2.765	2.741	Δ_{noise}	0.775
	TABLE	2.117	-2.981	2.979	x_{max}	2.979
	ERRORS	-9%	-7%	-8%	S/N	384%
2t	GPS	1.937	-2.751	2.695	Δ_{noise}	0.681
	TABLE	2.125	-2.986	2.991	x_{max}	2.991
	ERRORS	-9%	-8%	-10%	S/N	439%
2u	GPS	1.987	-2.729	3.109	Δ_{noise}	0.675
	TABLE	2.126	-2.985	2.995	x_{max}	2.995
	ERRORS	-7%	-9%	4%	S/N	444%
2v	GPS	2.019	-2.904	2.694	Δ_{noise}	0.720
	TABLE	2.129	-2.992	2.996	x_{max}	2.996
	ERRORS	-5%	-2%	-10%	S/N	415%
2w	GPS	2.067	-3.128	2.930	Δ_{noise}	0.819
	TABLE	2.123	-2.988	2.994	x_{max}	2.994
	ERRORS	-3%	8%	-2%	S/N	366%

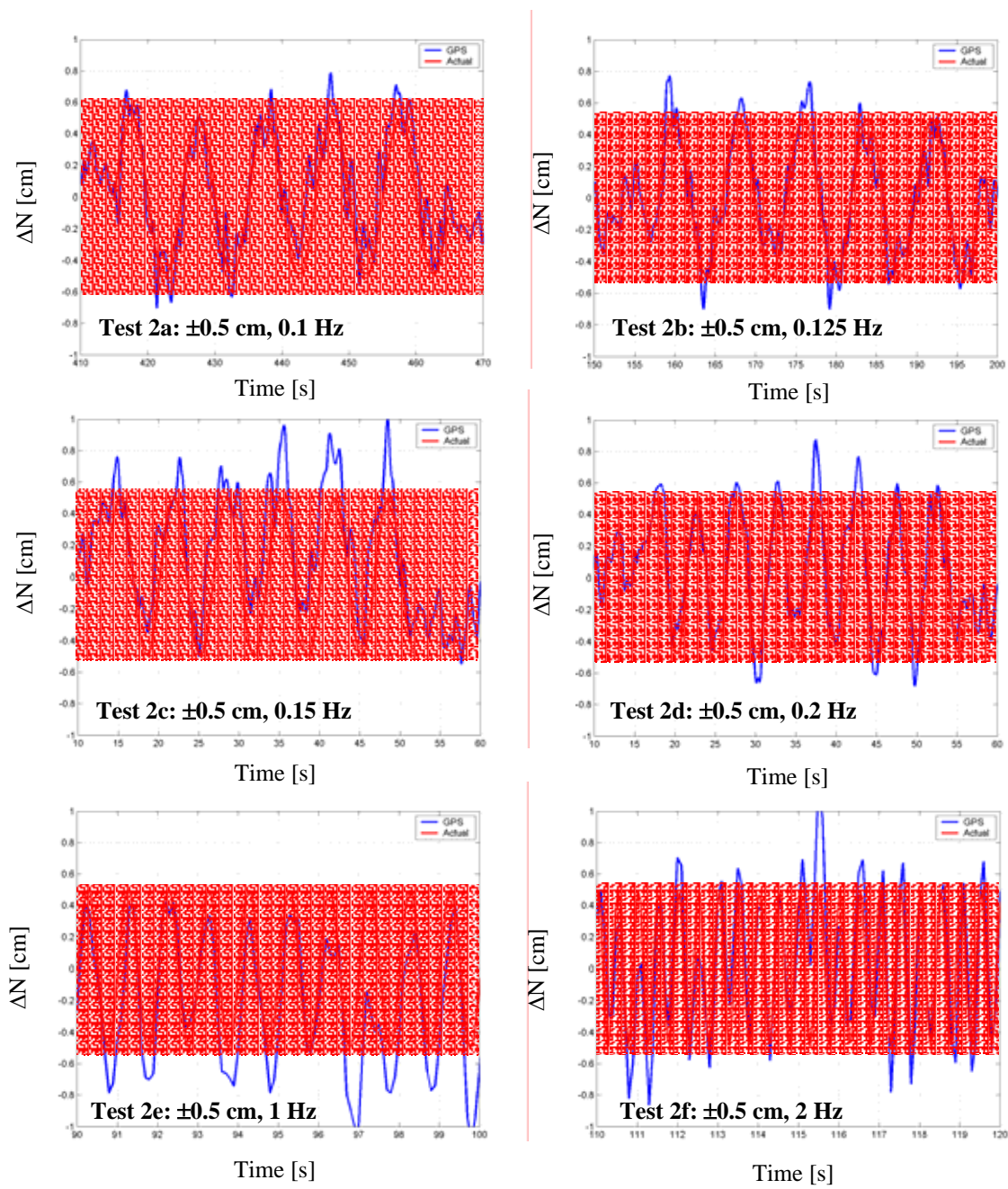


FIGURE 12.11. Comparison of shake table displacement (red) to GPS displacement estimate for Tests 2a-2f, mean noise threshold shaded in red

blue line is the GPS result following the filtering discussed in Section 12.4. To aid in evaluation of the performance, the range of values between mean noise thresholds for each test has been shaded. Any signal that is enveloped by this shaded region should be considered of insufficient amplitude for tracking, as is the case in this series of tests. Tests 2a-2d manifest a residual high frequency overlay, which may be lessened by adjusting the cutoff frequency of the low-pass filter. The low amplitude of the signal relative to the noise threshold results in large shifts of the tracked signal about its mean value, reiterating the possibility for low-amplitude, local mean trends in GPS data as a result of the inherent noise. At higher frequencies closer to the cutoff of the low-pass filter, the tracked result is cleaner though still prone to the inaccuracies in matching peak displacements within the signal. Referring to the statistical measures in Table 12.8, for this series of tests, the mean noise threshold is actually larger than the signal amplitude, reconciling the observed performance. Despite the inability of the GPS to capture peak displacements with repeatable accuracy, the standard deviation of GPS displacements is quite consistent with the actual table displacements. The worst performance in this series of tests was for the highest frequency signal at 2 Hz, Test 2f. For the lower frequency tracking, i.e. less than 1 Hz, errors in the standard deviation were minimized to 2-7%, indicating that the GPS sensor is well-suited to the frequency ranges anticipated in the full-scale application.

Doubling the amplitude in Tests 2g-2l, the signal being tracked is now 80-90% above the mean noise threshold, as listed in Table 12.8. Figure 12.12 displays the quality of tracking for this series of tests. In the lower frequency tests, Test 2g-2j, the appearance of higher frequency noise ripples are still present but reduced, as the amplitude of the

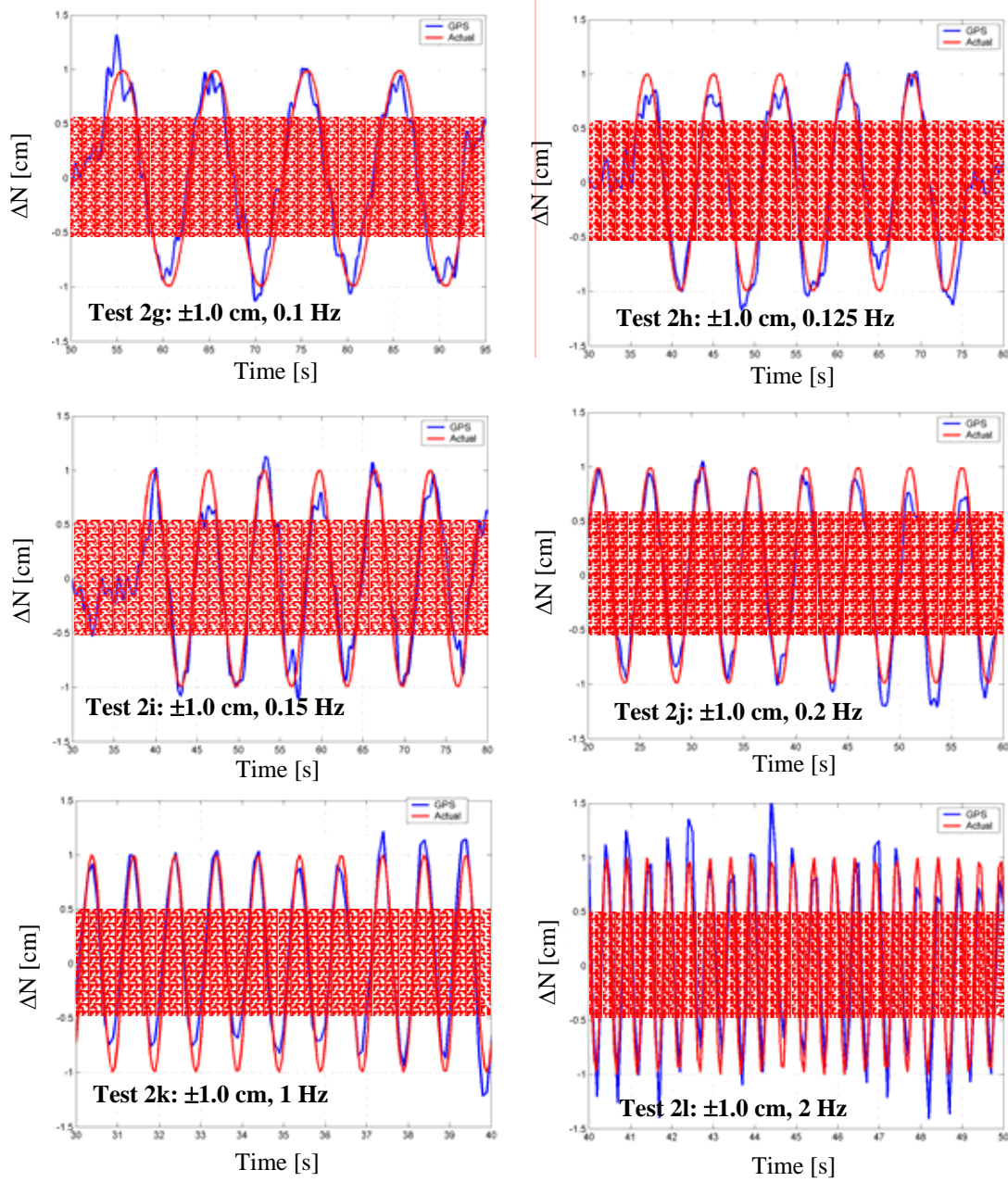


FIGURE 12.12. Comparison of shake table displacement (red) to GPS displacement estimate for Tests 2g-2l, mean noise threshold shaded in red

signal is nearly twice the noise threshold. The overall quality of the GPS tracking shows improvement when compared to the results of Figure 12.11. Note again that peak amplitudes are most difficult to consistently capture, as shown in Table 12.8. This can be in part the result of localized shifts in the mean, such as that in Test 2j between 50-60 s, similarly observed in Test 2k from 30 to 40 s. In general, both the standard deviation and peak tracking are improved for this series of tests, as a result of the increased amplitude. With this sufficient level of signal-to-noise ratio, the performance in terms of errors in standard deviation shows no appreciable dependence on frequency, having errors of magnitude 1 to 12% across the board. For the low frequency tests (2g-2j), standard deviations are underestimated by less than 10%.

Increasing the amplitude again to ± 2 cm, elevates the amplitude of the tracked signal to approximately four times the mean noise threshold to further diminish the level of discrepancy between the GPS estimate and the actual table displacement, as shown for Tests 2m-2r in Figure 12.13. Again the slight jaggedness for the low frequency tests (Test 2m-2p) is the result of the high frequency noise in the system. At these larger amplitudes, the standard deviation errors show no visible dependence on frequency, with errors remaining at or below 10%, however it becomes evident that it can be difficult to consistently capture peaks in the response. Table 12.8 lists only the errors encountered by GPS in capturing the maximum and minimum values of the table displacement. This, however, does not describe the ability of GPS to capture the many intermediate peaks within the response. Figure 12.13 affirms this difficulty in consistently matching these peaks, similarly observed in the calibration tests by Tamura et al. (2001). Table 12.8 demonstrates that errors in peak matching can be as small as 0% or as large as nearly

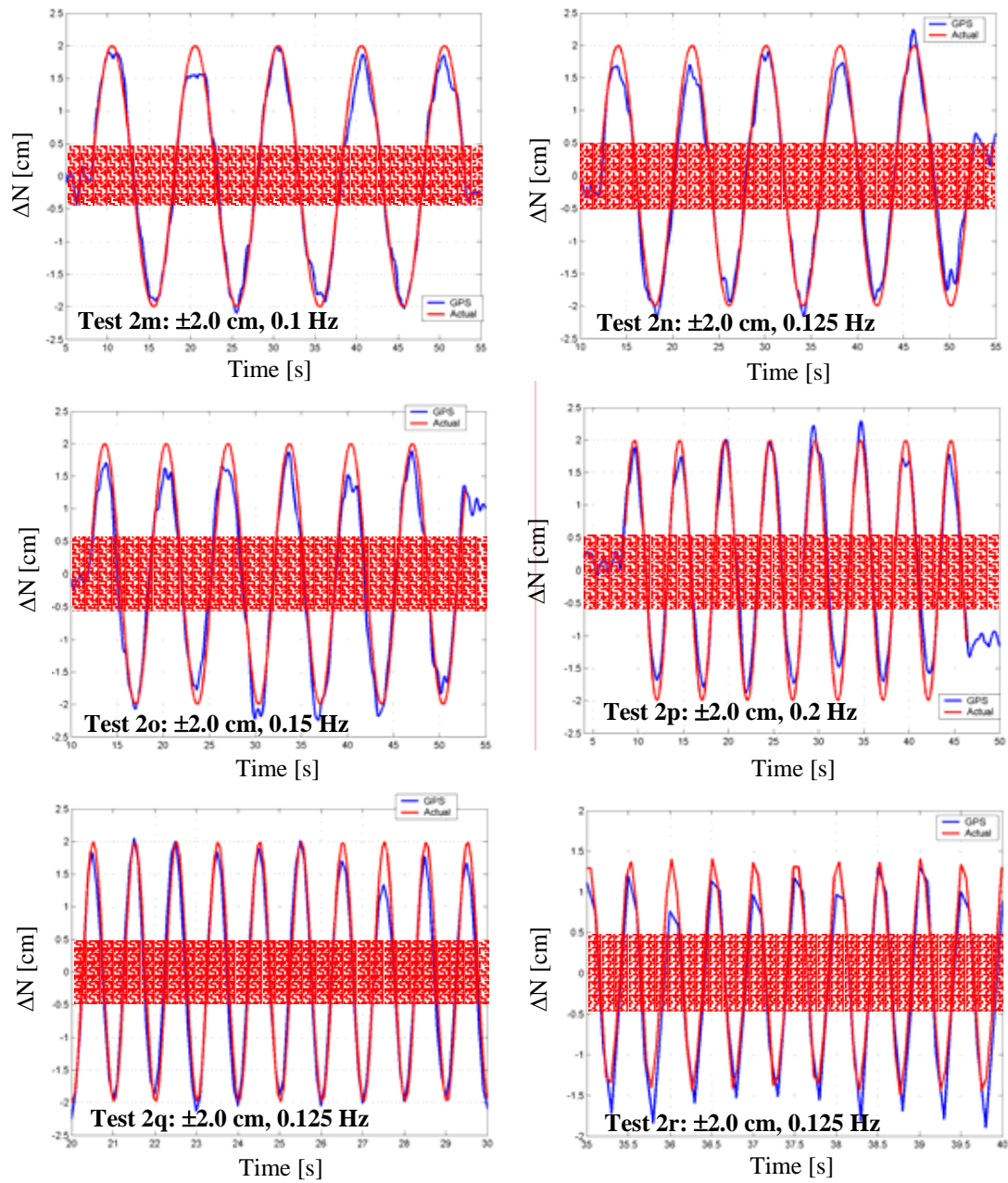


FIGURE 12.13. Comparison of shake table displacement (red) to GPS displacement estimate for Tests 2m-2r, mean noise threshold shaded in red

30%. Returning to Table 12.7, the standard deviation σ_N of a GPS estimate is a quality measure that fluctuates with each epoch of the monitoring period due to the variations in a variety of error sources discussed in Chapter 10. While the mean value is used to define the error threshold in Table 12.7, Figure 12.8 demonstrates that these error bounds are actually time varying. Over the course of test series 2, the standard deviation in the GPS estimate can be as high as 3 to 4 mm. These isolated degradations in quality help to explain local inaccuracies in peak matching, despite good quality in overall tracking quantified by more averaged measures like standard deviation in Table 12.8.

The results of the last of this series, Test 2s-2w, are presented in Figure 12.14. In these figures, the large amplitude levels were moderately offset by higher noise levels, bringing the signal-to-noise ratio to approximately the same or slightly higher levels as the results shown in Figure 12.13. This is the result of a diminished number of satellites, leading to the higher DOP errors shown in bold in Table 12.4. Had a greater number of satellites been available at this time, in a more optimal configuration, the GPS tracking ability would have been enhanced. Even so, the larger amplitude of these signals produces a bit cleaner tracking, especially in the low frequency range. Referring to the statistics in Table 12.8, the dependence on frequency is again not evident. Instead, uniformly over all the tests at this amplitude level, the errors in standard deviation underestimate all less than 10%. For this ± 3 cm signal, the peak matching is consistently the best of all Test 2. The magnitude of errors in peak estimation is limited between 2 and 10%. This affirms that the amplitude of motion greatly influences the accuracy of GPS tracking, even in comparison to Tests 2m-2r, which had comparable signal-to-noise ratios. Note however, that in the case of Test 2w, it becomes evident that the peak

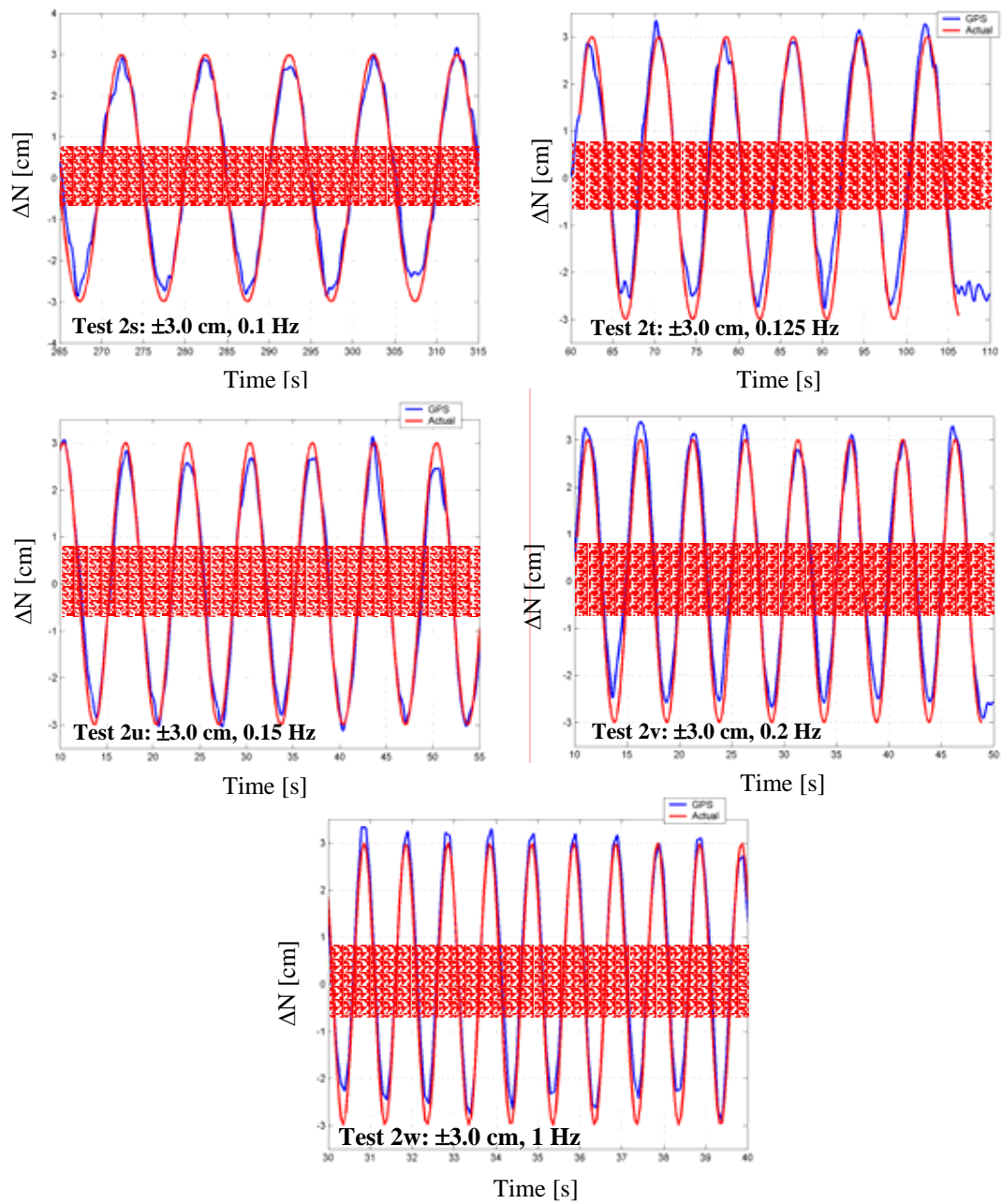


FIGURE 12.14. Comparison of shake table displacement (red) to GPS displacement estimate for Tests 2s-2w, mean noise threshold shaded in red

matching is poorer in specific areas, apparently as a result of some weak mean trend in the GPS tracking, though this is small compared to the amplitude of motion.

In general, this series of tests reflects, that for a very simple waveform, the amplitude of motion is the most critical parameter in assuring quality GPS tracking. For motion levels accompanied by signal-to-noise ratios less than 100%, peak errors can reach 45%, meanwhile errors in standard deviation can rise to 20% for higher frequency signals. Once above a 100% signal-to-noise ratio, these standard deviation errors, regardless of the frequency of motion, remain beneath 10%. Peak errors, though erratic, diminish significantly for large amplitude signals, even under less favorable noise conditions. Thus, it can be summarized that quality tracking in terms of averaged measures like standard deviation can be achieved consistently when the signal-to-noise ratio is 200% or more. This corresponds to motions above ± 1 cm. The errors in peak estimation are consistently mitigated for signals with above ± 2 cm.

12.5.2 Test 3a-3f: Verification of Ability to Track Complex Signals

While Test 2 established the amplitude ranges that GPS could track reasonably, those signals were of simple sinusoidal form. Test series 3 whose parameters were delineated in Table 11.3, uses a variety of more sophisticated waveforms to further verify GPS performance. Test 3a begins with a sinusoidal chirp with frequencies that sweep quadratically from 0.1 to 2 Hz over the course of one minute. As shown in Table 12.4, DOP values during this test and the following test were relatively high. Table 12.9 summarizes the statistics associated with this test and the other experiments in Test 3. For

TABLE 12.9

ACCURACY OF GPS TRACKING FOR TEST 3

Test		ΔN [cm]			Noise	
		Std	Min	max		
3a	GPS	0.718	-0.942	1.3837	Δ_{noise}	0.794
	TABLE	0.696	-1	1	x_{max}	1
	ERRORS	3%	-6%	38%	S/N	126%
3b	GPS	1.047	-1.831	2.005	Δ_{noise}	0.874
	TABLE	1.024	-2.255	2.217	x_{max}	2.217
	ERRORS	2%	-19%	-10%	S/N	254%
3c	GPS	0.631	-4.268	2.013	Δ_{noise}	0.721
	TABLE	0.656	-4.652	2.181	x_{max}	2.181
	ERRORS	-4%	-8%	-8%	S/N	302%
3d	GPS	1.079	-4.787	3.433	Δ_{noise}	0.561
	TABLE	1.113	-4.979	3.273	x_{max}	3.273
	ERRORS	-3%	-4%	5%	S/N	583%
3e	GPS	0.909	-2.642	2.323	Δ_{noise}	0.494
	TABLE	0.986	-2.630	2.560	x_{max}	2.560
	ERRORS	-8%	0%	-9%	S/N	518%
3f	GPS	1.071	-4.548	2.731	Δ_{noise}	0.523
	TABLE	1.143	-4.997	2.756	x_{max}	2.756
	ERRORS	-6%	-9%	-1%	S/N	527%

Test 3a, the tracking in terms of standard deviation is quite good, though the maximum peak displacement observed by the GPS is nearly 40% higher than the actual table displacement. This results from the fact that the noise level is almost on the order of the amplitude of motion, which was ± 1.0 cm. As discussed in Section 12.5.1, the peak matching can have significant limitations at such low amplitudes. Figure 12.15 shows a comparison between the GPS estimated displacements and the actual motions of the table, zooming in on several time intervals during the course of the test. This chirp example demonstrates that the overshoots in peak displacement are more visible in the high frequency component of the chirp. Note that there is similar jaggedness in the low frequency range, indicating that more stringent bandpass filtering must be conducted to remove more of this high frequency overlay.

Test 3b, tracking of a random signal discussed in more detail in Section 11.5.3, was similarly conducted under less than favorable monitoring conditions, resulting again in a high mean noise threshold. Fortunately the high amplitudes that are achieved in the signal offset this. As shown in Table 12.9, the errors in standard deviation tracking are only a few percent, though again, there can be difficulty in accurately capturing peak displacements, which can be in error by 10-20%. However, as a result of the higher amplitudes of motion in this test, these findings are better than those of Test 3a. As shown in Figure 12.16, despite the fact that the noise thresholds can be quite significant, the tracking of the random signal is reasonable, particularly between 70 and 80 seconds.

Considering the intended application of this monitoring system, a series of responses were generated to mimic MDOF systems under the action of wind. Details of

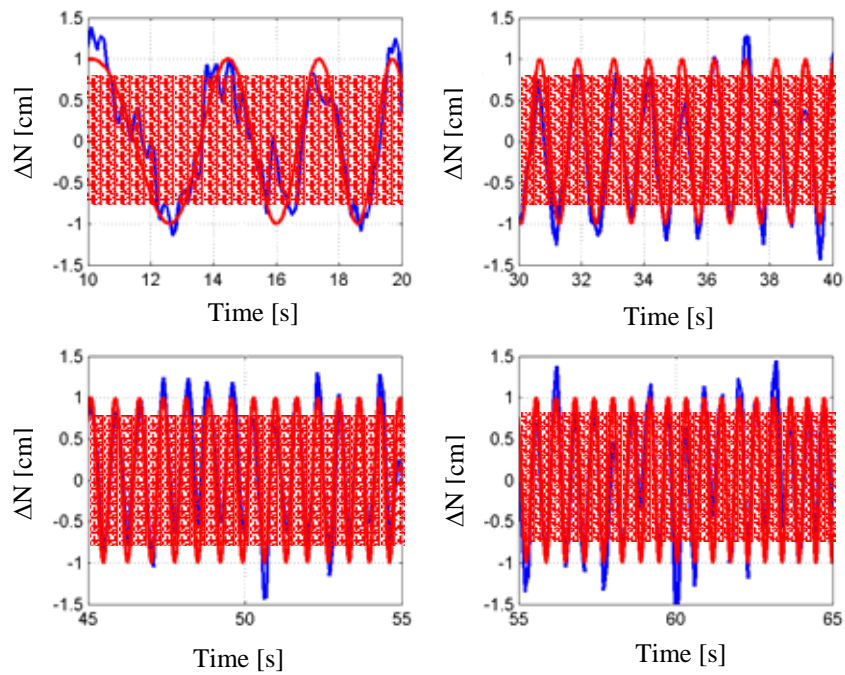


FIGURE 12.15. Comparison of shake table displacement (red) to GPS displacement estimate for Test 3a at various intervals in the test, mean noise threshold shaded in red

these simulated time histories are provided in Section 11.5.3. Tests 3c-d involve a system responding at a higher frequency for two amplitude levels. The results of the test are shown in Figure 12.17, which displays a comparison for the entire duration of the test as well as snapshots zooming in on specific intervals in more detail. Referring again to Table 12.9, the standard deviation tracking is in error by 3-4%, while peak matching is quite good, with errors between 4 and 8% in magnitude. In Test 3c, the amplitude levels are on the order of Test 3b, though its noise level is quite smaller, which may help to explain the superior peak matching. Another consideration is the duration of testing.

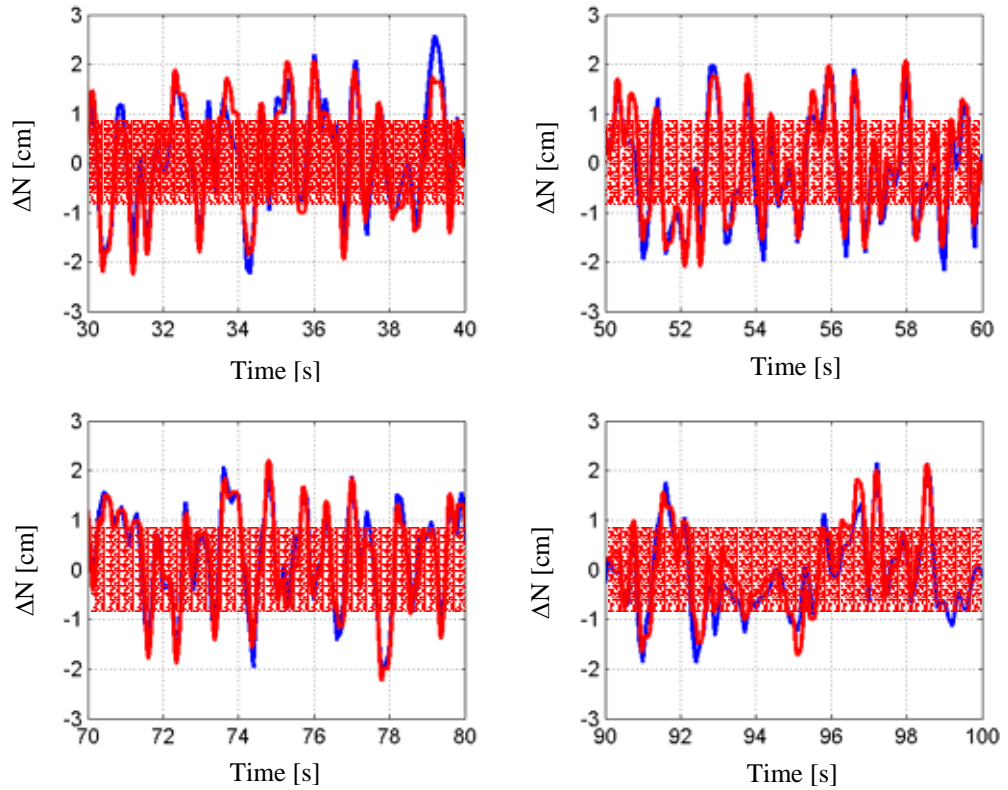


FIGURE 12.16. Comparison of shake table displacement (red) to GPS displacement estimate for Test 3b at various intervals in the test, mean noise threshold shaded in red

Each of the experiments in Test 2 and Tests 3a and b were relatively short duration tests lasting only a handful of minutes. Moving into Test 3c-f, longer tests on the order of several minutes were being conducted. As a result, the post-processing protocol was afforded more amounts of data for atmospheric modeling and ambiguity resolution. Returning to Figure 12.17, as expected, tracking is superior when the amplitude of motion is above the mean noise threshold, e.g. note the evolution in the final zoomed frame spanning 290 to 320 s. However, even in the frames that display low amplitude tracking, the comparison between the GPS and the table are quite reasonable. Overall,

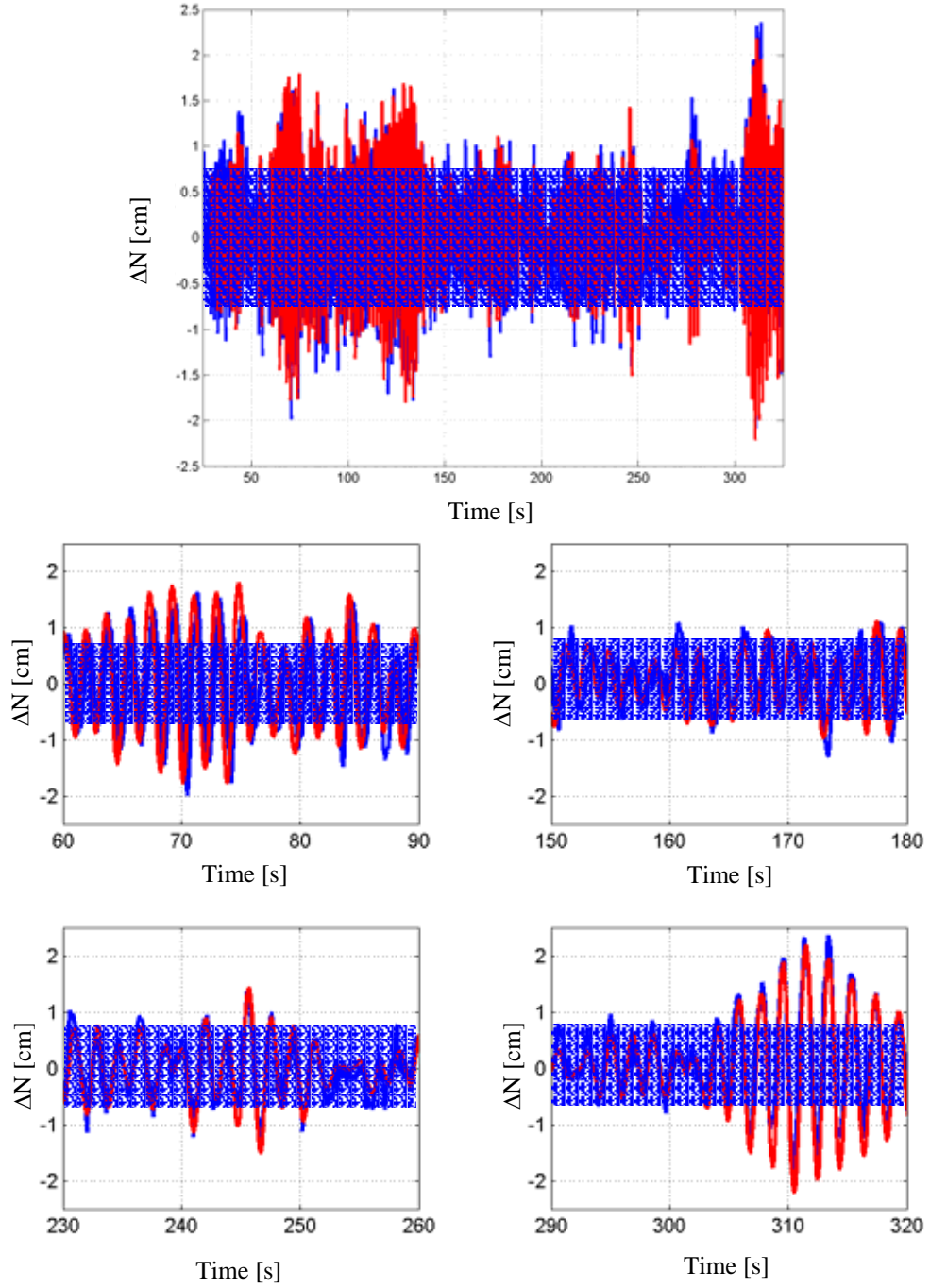


FIGURE 12.17. Comparison of shake table displacement (red) to GPS displacement estimate for Test 3c over the duration of the test (top) and zooming in at various intervals in the test, mean noise threshold shaded in blue

these findings suggest that the GPS displacement estimates indeed improve over the course of longer-duration testing, as will be encountered in the full-scale application.

The same linear system is again simulated in Test 3d, though at larger amplitude levels. As shown in Table 12.9, the standard deviation is again underestimated by only 3%, a slight improvement over the findings of Test 3c. The peak errors are nearly one half of these found in Test 3c, taking on magnitudes of 4-5%. This is a result of the reduction in noise threshold as the satellite configuration became more favorable, as shown in Table 12.4. This coupled with the increased amplitude of motion, led to a 583% signal to noise ratio. Figure 12.18 shows the results of this test in a format similar to the previous figure. The overall quality of the tracking is apparent in situations where motions are of sufficient amplitude in conjunction with low GPS noise conditions. Though these findings are promising, they do not reflect the frequency of motion anticipated in the full-scale application, prompting consideration of Tests 3e-f.

These two tests, detailed further in Section 11.5.3, simulate the response of tall, flexible building, responding to the action of wind with a fundamental frequency on the order of 0.12 Hz. Returning to Table 12.9, the errors in standard deviation are slightly higher than Test 3d, taking on values of 6-8%. In terms of peak tracking, errors in this case are less than 10% and as little as 0%. The noise levels of these tests were slightly less than Test 3d but the amplitude of motion was also slightly smaller, leading to overall signal-to-noise ratios that were less than Test 3d. This may explain why peak and standard deviation errors were slightly elevated in Tests 3e-f. Regardless, peak tracking in error by less than 10% for a signal whose maximum amplitude is less than ± 3.0 cm

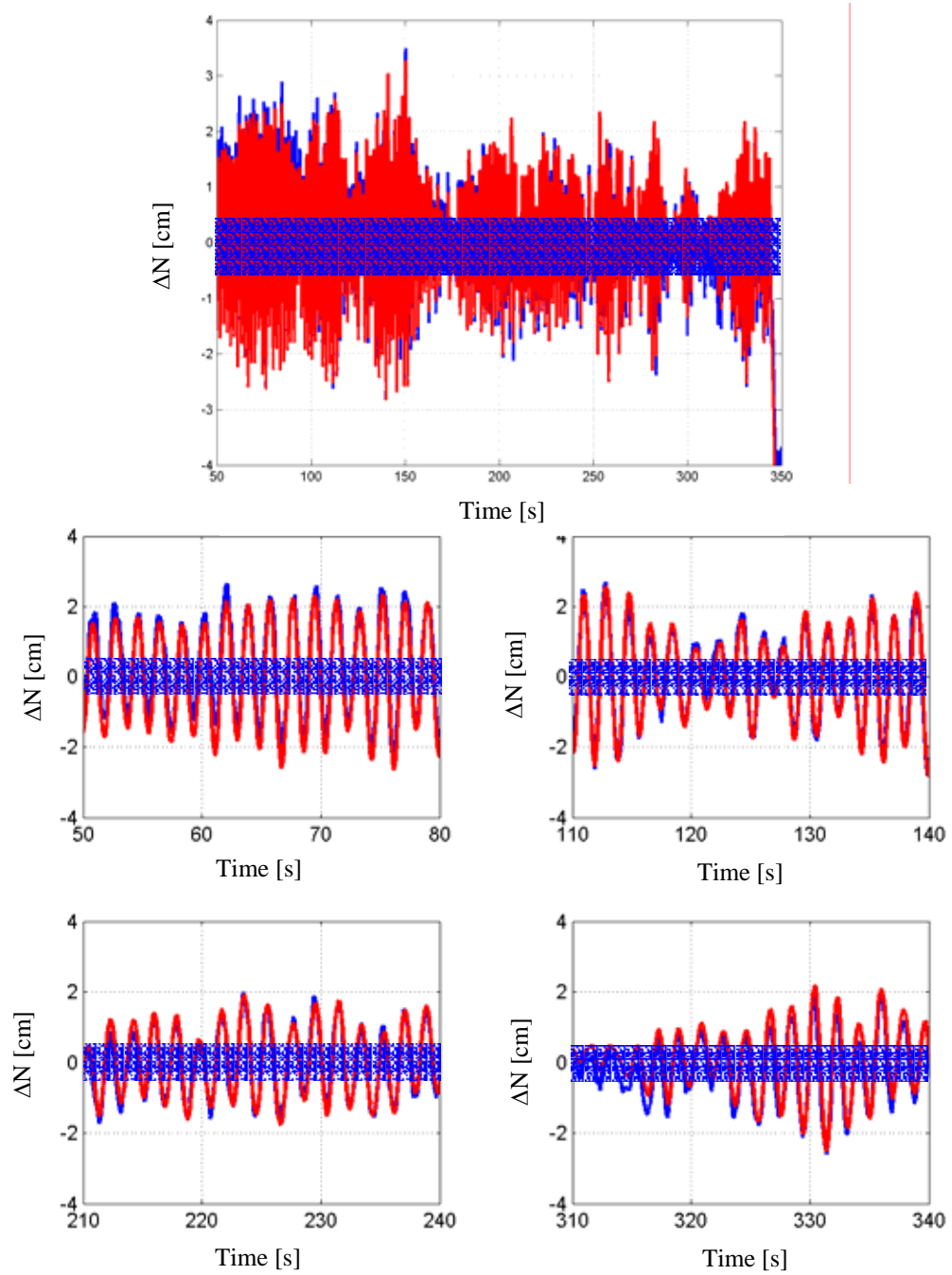


FIGURE 12.18. Comparison of shake table displacement (red) to GPS displacement estimate for Test 3d over the duration of the test (top) and zooming in at various intervals in the test, mean noise threshold shaded in blue

reiterates the promise of GPS for tracking tall building response under the action of wind. Figures 12.19 and 12.20 respectively display the GPS tracking of the signals simulated in Test 3e and 3f. The tracking appears to be very reasonable for both of these cases. The first zoom plot in Figure 12.19 reflects that, despite the low amplitude of the signal, in comparison to the noise threshold between 1000-1040 s, tracking can still be reasonable. Note that at such low amplitudes, some of the jaggedness associated with high frequency noise that has not been filtered away again resurfaces. Note from 1140-1150 s and 1260-1270 s the zoomed plots display a flat line characteristic. This is actually the result of a minor sticking of the table. This sudden glitch in the simulated motion was tracked with accuracy by the GPS sensors. It appears that as the amplitude of motion increased in Figure 12.20, the quality of tracking indeed improves overall. In light of these findings, over longer monitoring periods, both averaged quantities like standard deviation as well as peak measures can be accurately captured within 10% as long as the signal amplitude is three times the noise level. Specifically Tests 3e-f affirm the suitability for this technology in the monitoring of tall building motions.

12.6 Test 4a-c: Influence of Gas Capsule

As discussed in more detail in Section 11.2.3, a lightning protection system has been integrated into the GPS configuration. For all tests discussed thus far, this lightning protection hardware was not implemented. Test 4 explores the influence that this hardware may have on the quality of GPS displacement estimates. As discussed in Section 11.5.4, three tests were conducted to confirm the influence of each gas capsule

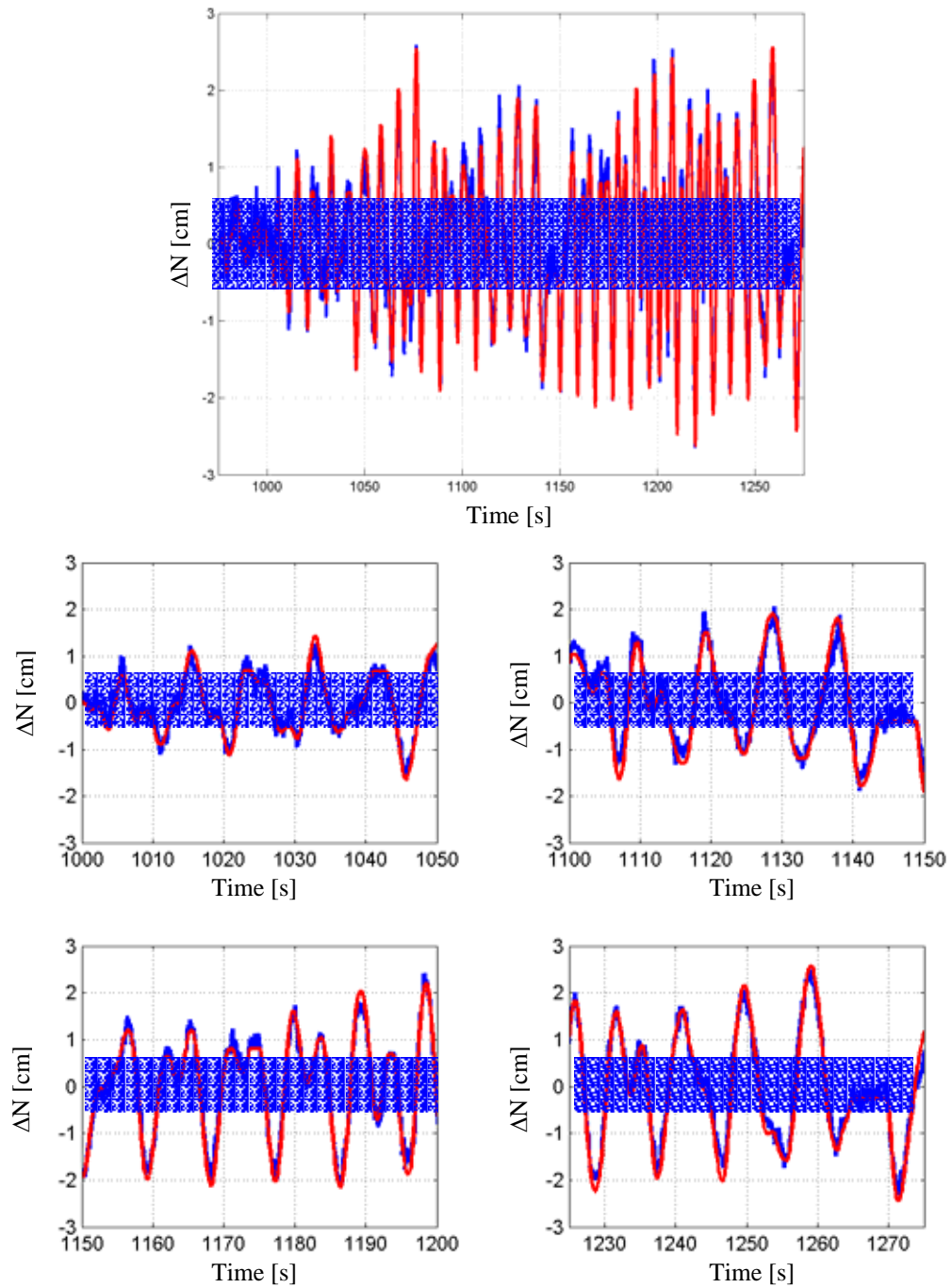


FIGURE 12.19. Comparison of shake table displacement (red) to GPS displacement estimate for Test 3e over the duration of the test (top) and zooming in at various intervals in the test, mean noise threshold shaded in blue

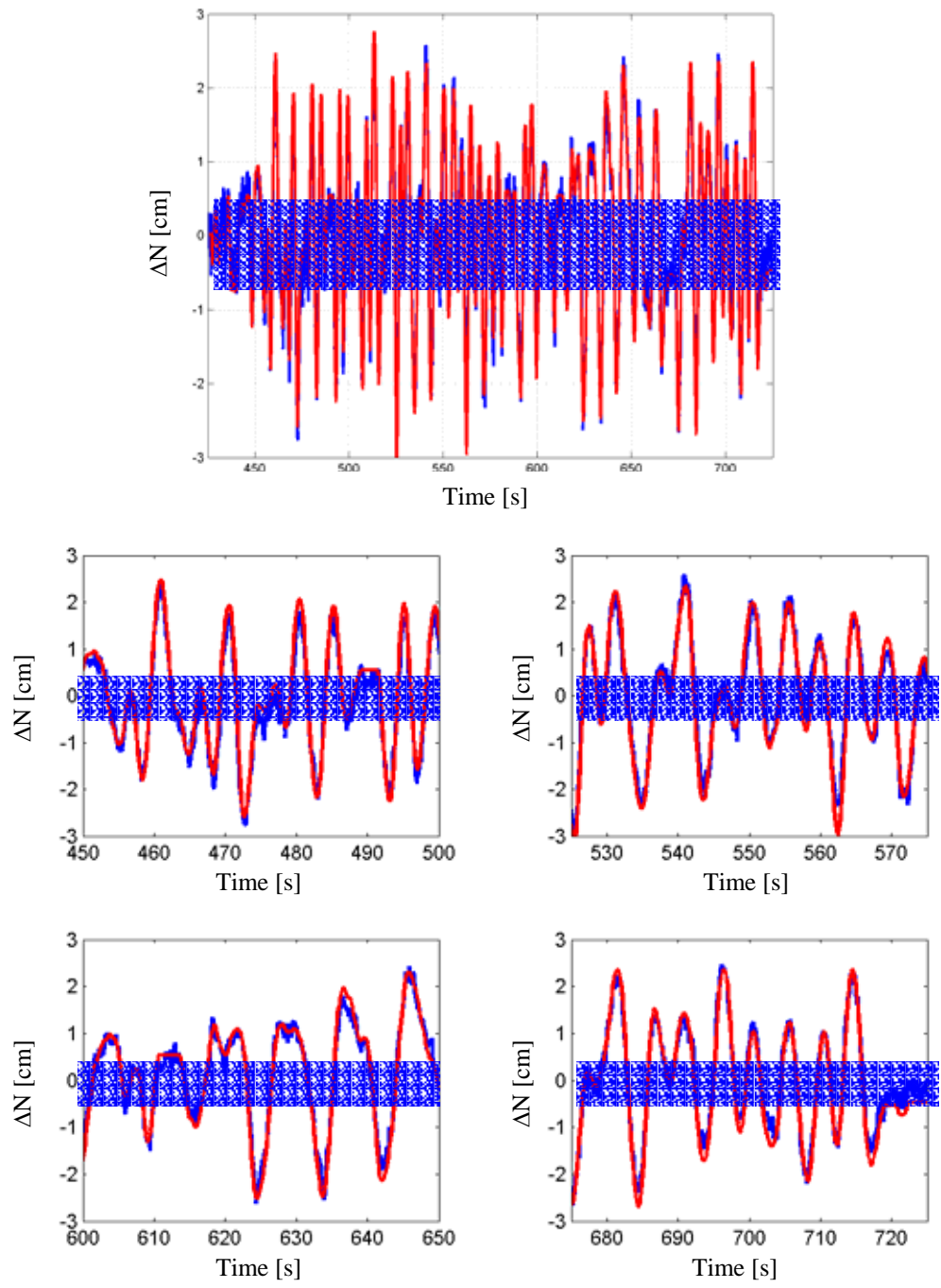


FIGURE 12.20. Comparison of shake table displacement (red) to GPS displacement estimate for Test 3f over the duration of the test (top) and zooming in at various intervals in the test, mean noise threshold shaded in blue

and were compared against test results in which no gas capsule was implemented under similar testing conditions, in terms of satellite configuration. The statistics associated with this test series are shown in Table 12.10. The shaded rows indicate the statistics when gas capsules were in place. An inspection of the statistics associated with this static test series reveals no appreciable increase in displacements in the east component, in fact, in the gas capsule tests there was a 15% decrease in the mean and standard deviation, indicating that the background noise in the GPS system was not increased by the addition of the gas capsule. Looking at the standard deviation of the GPS displacement estimates, there is a minor elevation in the statistics for Test 4a and b, as also reflected in the position quality measure. This 20% increase position quality led to a 25% increase in the standard deviation of the estimated GPS motion in the northern direction. Additionally, the mean component in Test 4a and b in this northern direction is appreciably larger with the addition of gas capsules. However, the increase in background noise in the north direction when the gas capsules were in place may be offset by the decrease in background noise while they were in place in the east direction.

Figure 12.21 helps to put these findings in clearer perspective. In this figure it becomes evident that if anything, Test 4c, which involved no form of lightning protection, manifests the most obvious bias and actually the largest values of displacement in the north and south direction during the course of this static test. This may indeed be due to the fact that, as shown in Table 12.10, the DOP values were not as favorable for this last test in series 4. Still, this affirms that any errors introduced by the lightning protection are no greater than the common errors due to satellite orientation and others inherent to GPS technology. Inspection of the time histories in Figure 12.22 does

TABLE 12.10

STATISTICS OF GPS DISPLACEMENT ESTIMATES AND ASSOCIATED ERRORS
FOR TEST 4A-C

Test	ΔE [cm]				ΔN [cm]			
	mean	std	Min	max	mean	std	min	max
4a	0.031	0.171	-0.619	0.641	-0.305	0.301	-1.424	0.766
4b	-0.022	0.166	-0.578	0.562	-0.117	0.215	-0.836	0.614
4c	0.086	0.197	-0.605	0.805	0.028	0.227	-0.878	0.972
Test	σ_E [cm]				σ_N [cm]			
	mean	std	Min	max	mean	std	min	max
4a	0.143	0.044	0.030	0.350	0.225	0.070	0.040	0.570
4b	0.157	0.043	0.040	0.370	0.212	0.059	0.050	0.510
4c	0.135	0.045	0.030	0.400	0.169	0.056	0.040	0.460
Test	PDOP	GDOP		PQ [cm]				
				mean	std	min	max	
4a	2.4-2.8	2.8-3.1		0.266	0.082	0.050	0.670	
4b	2.3-2.4	2.7-2.8		0.263	0.073	0.070	0.630	
4c	2.7-3.4	3.0-4.0		0.216	0.072	0.050	0.600	

affirm the statistics shown in Table 12.10. There are obvious mean trends in the northern displacement component in Tests 4a and b. However, the presence of local mean trends was also observed in other static tests presented in this chapter and also can be seen in the eastern component of Figure 12.22 for Test 4c, for which no gas capsule was utilized. These mean trends should not be interpreted as having anything to do with the use of gas capsules and instead are inherent characteristics of GPS monitoring. The time histories of the standard deviations of GPS displacement estimates also show no visible evidences of differences in the cases with gas capsule and that without.

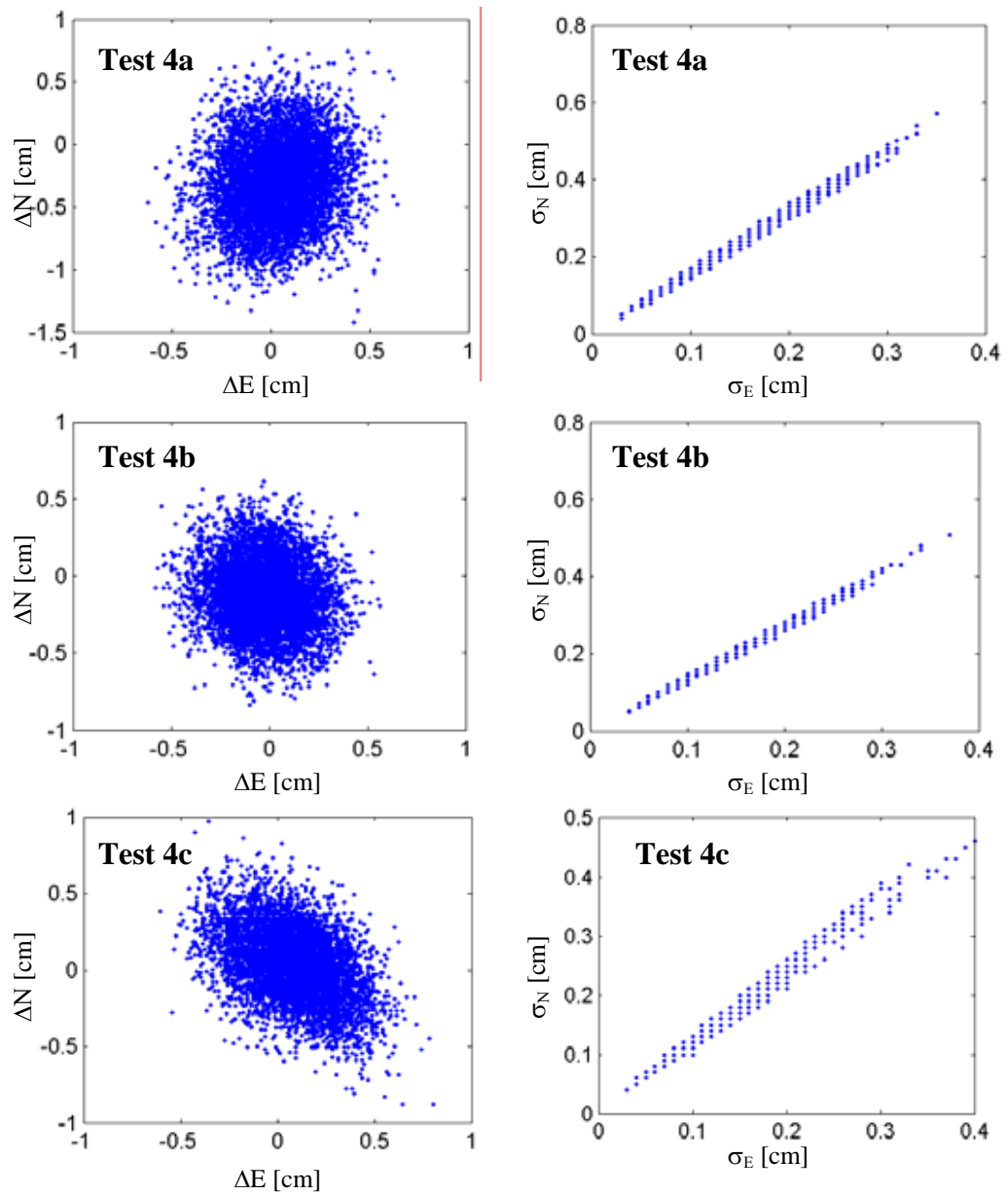


FIGURE 12.21. GPS displacements estimated during Tests 4a-c (left) and standard deviation of GPS displacement estimate

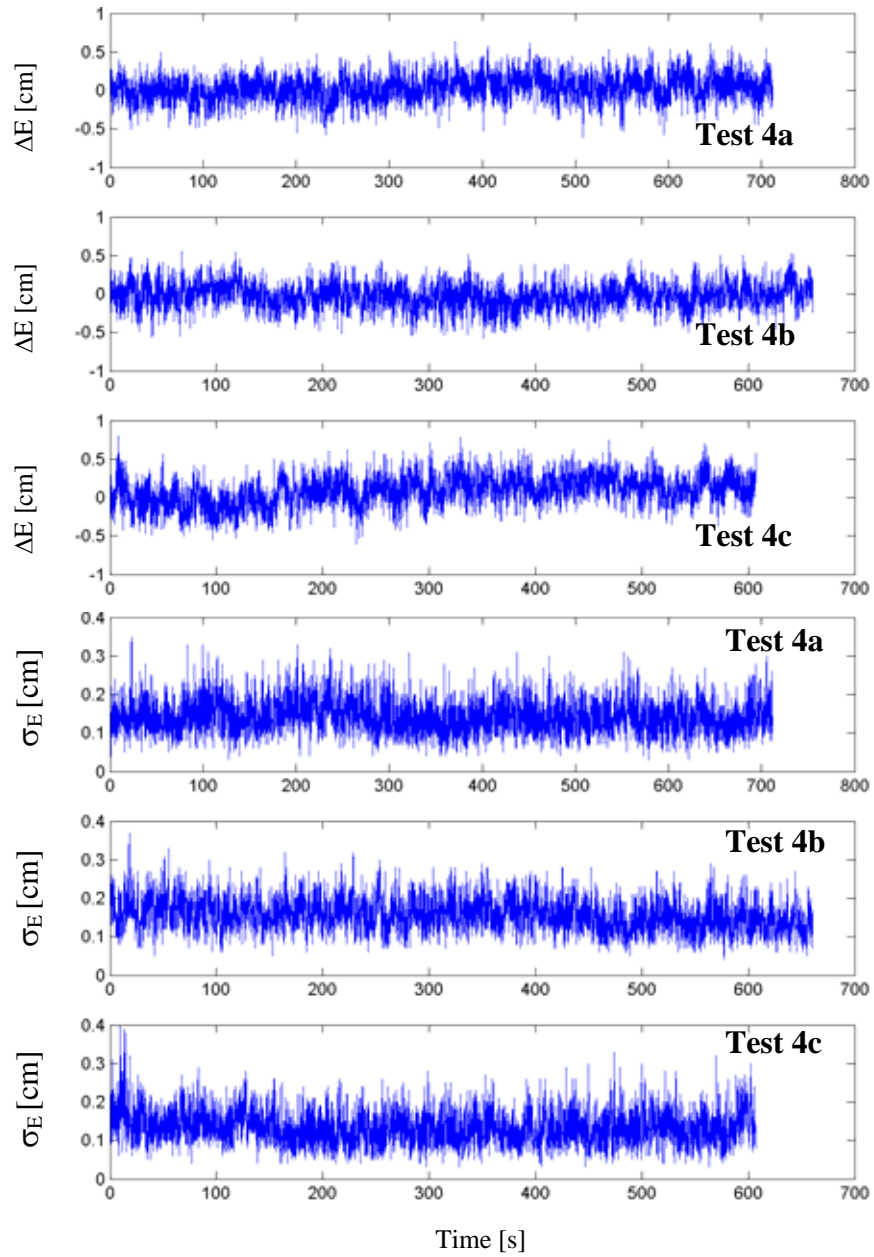


FIGURE 12.22a. Time histories of Test 4a-c GPS East-West displacement predictions and standard deviation of GPS displacement estimate

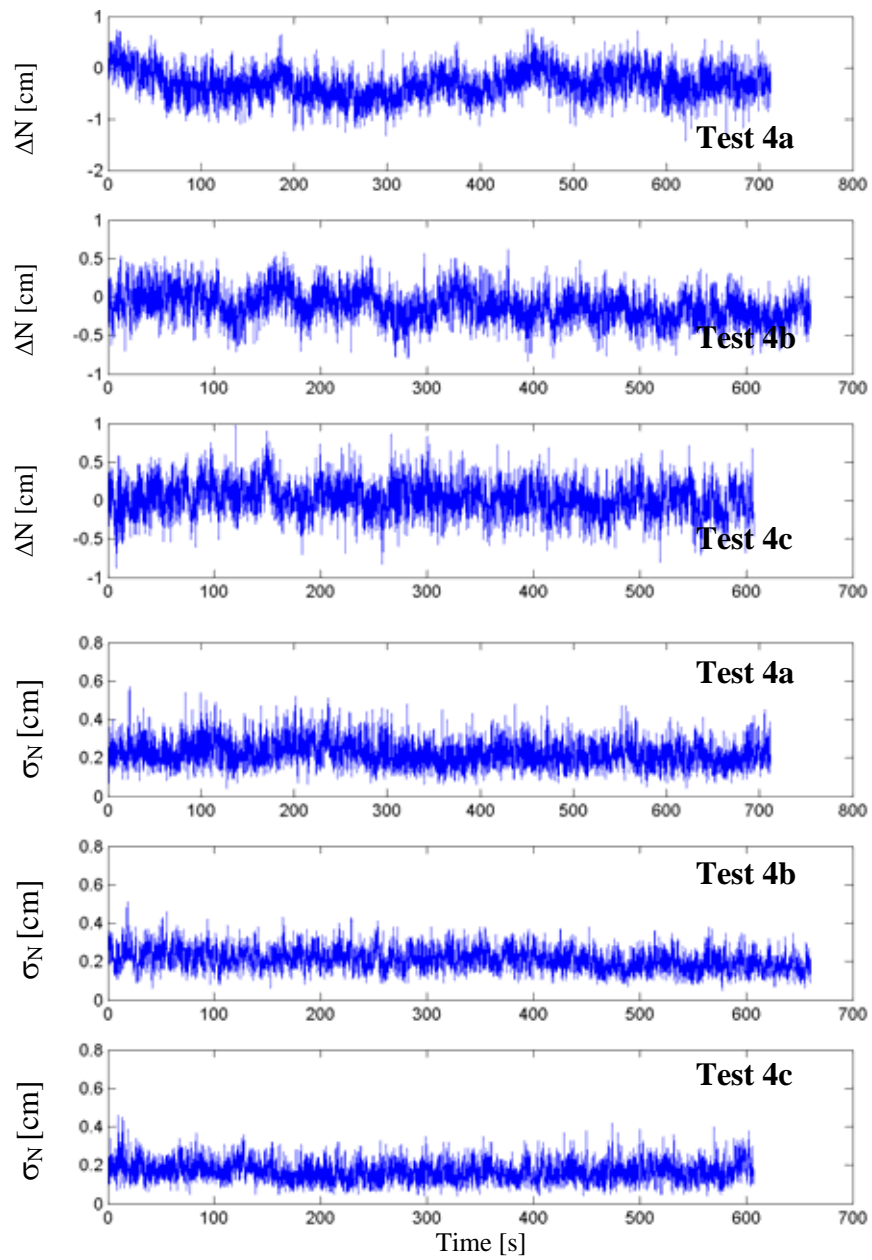


FIGURE 12.22b. Time histories of Test 4a-c GPS North-South displacement predictions and standard deviation of GPS displacement estimate

12.7 Test 5: Coordinate Transformation Mock-Up

As discussed in Section 11.5.5, in countless applications, the structural axes of motion do not align identically with the north and east axes. As a result, the challenges associated with transforming GPS displacement data into other coordinate systems is investigated through Test 5. As shown in Figure 12.23, the orientation of the rover was rotated by an angle θ . This angle assumed to be 45° based on the measurements in the field using the ETrex Summit handheld GPS units. However, it can be difficult to measure this angle with complete accuracy in the field, as the subsequent discussions will illustrate. Examining Figure 12.23, it is evident that an estimate of the table displacement along the shifted axis can be obtained from ΔE by performing the following transformation

$$\Delta table_E = \frac{\Delta E}{\sin \theta}. \quad (12.2)$$

An estimate based on ΔN can similarly be obtained using

$$\Delta table_N = \frac{\Delta N}{\cos \theta}. \quad (12.3)$$

Using these relations and $\theta=45^\circ$, the statistics in Table 12.11 were generated along with the images in Figure 12.24. For the value of θ intended, the standard deviations of ΔE and ΔN should be nearly identical. The fact that they are not indicates that the table was not specifically oriented along a 45° angle. A more precise measure of the angle defining the orientation of the axis of motion can be obtained by

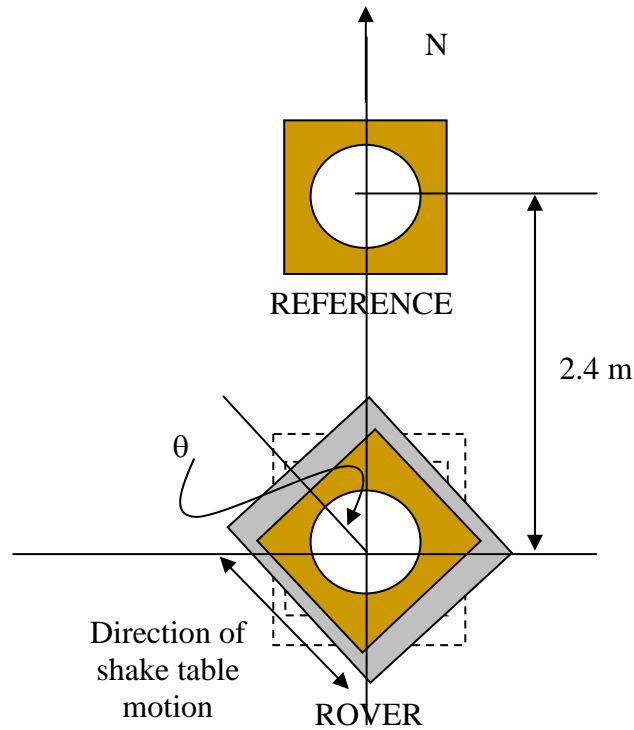


FIGURE 12.23. Generalized orientation of reference and rover stations for Test 5

$$\theta = \arctan\left(\frac{\text{std}(\Delta E)}{\text{std}(\Delta N)}\right). \quad (12.4)$$

Using this relation, the approximate angle of inclination is 50° and not 45° . Using this value in the transformation relations in Equations 12.2 and 12.3 yields a standard deviation, at least for the east axis, which compares well with the actual table displacement. This is affirmed in Figure 12.24. The value for the north axis, while improved, does not match with the same level of precision. It is not unusual to observe differing performance along the two directional axes. The average standard deviation of GPS displacement estimates in the east direction was 0.181 cm over the course of Test 5, while it was 0.252 cm along the north direction. Therefore, a handheld GPS should be

TABLE 12.11

ESTIMATES OF MOTION ALONG SHIFTED AXIS FOR TEST 5

	Mean	std	min	Max
Δ table [cm]	0.020	1.413	-1.983	1.986
No Transformation				
Δ E [cm]	0.039	0.709	-1.624	1.730
Δ N [cm]	0.057	0.590	-1.159	1.310
$\theta=45^\circ$				
Δ table _E [cm]	~0	1.520	-2.296	2.446
Δ table _N [cm]	~0	1.113	-1.164	1.853
$\theta=50^\circ$				
Δ table _E [cm]	~0	1.404	-2.120	2.258
Δ table _N [cm]	~0	1.224	-1.804	2.038

used in the field to approximate the angle defining the axis of motion for first estimate, which can then be verified and refined, if necessary, using Equation 12.4 and the statistics from post-processed data.

12.8 Test 6a-b: Influence of Antenna Mount

The use of an elevated antenna mount can be critical in minimizing obstructions that would degrade the quality GPS tracking. As discussed in Section 11.5.6, the significance of elevated mounts is assessed in the final test of this calibration study. As shown in Table 12.12 and by the time histories in Figure 12.25, there is no appreciable change in the background noise in the GPS measurements, as defined by the statistics of estimated GPS displacements for this static test. This affirms that at least at the Anderson Road site, there were no reflective surfaces or interferences from the ground when the antenna was

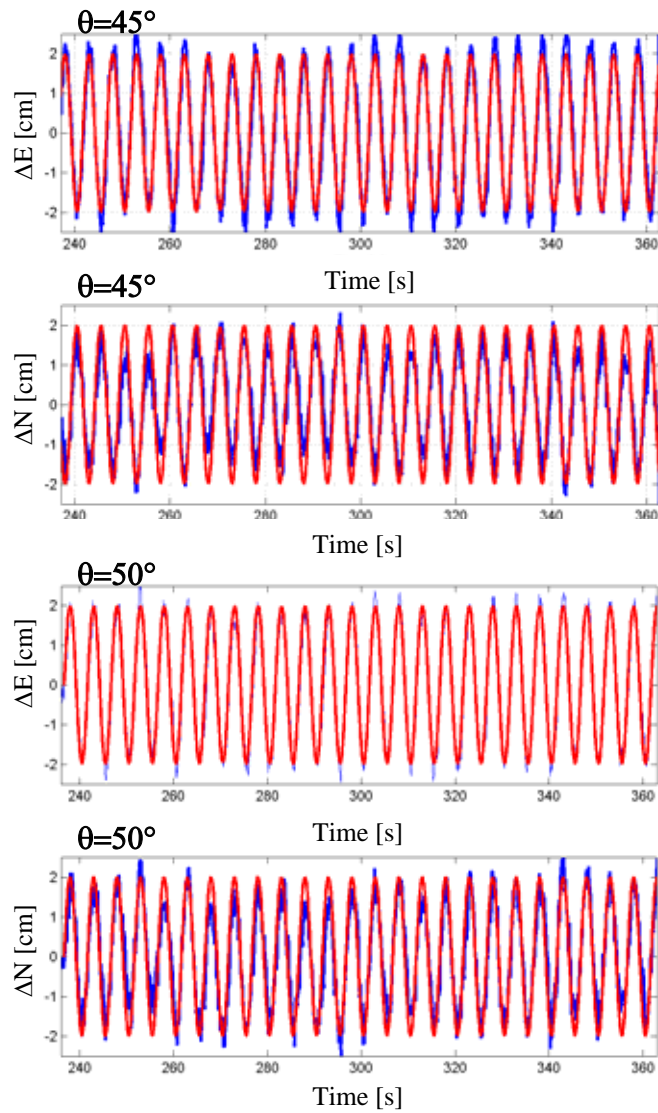


FIGURE 12.24. Comparison of actual table displacement (red) and transformed GPS displacement estimates along E-W and N-S axes, using transformation angle of 45° and 50°

TABLE 12.12

STATISTICS OF GPS DISPLACEMENT ESTIMATES AND ASSOCIATED ERRORS
FOR TEST 6

Test	ΔE [cm]				ΔN [cm]			
	mean	Std	Min	max	mean	std	min	max
6a	-0.0803	0.1991	-0.8273	0.6027	-0.0147	0.2843	-0.9909	1.0491
6b	-0.0484	0.2241	-0.9909	0.8091	-0.0808	0.2689	-0.9738	0.9962
Test	σ_E [cm]				σ_N [cm]			
	mean	std	Min	max	mean	std	min	max
6a	0.202	0.0482	0.06	0.42	0.2434	0.0591	0.07	0.5
6b	0.2237	0.0586	0.07	0.55	0.2521	0.0629	0.07	0.57
Test	PDOP	GDOP		PQ [cm]				
				mean	std	min	max	
6a	1.9-2.2	2.1-2.5		0.3163	0.0762	0.09	0.66	
6b	2.2-3.5	3.5-4.3		0.3373	0.0849	0.1	0.79	

placed at this level. However, applications in urban environments may find significant influence from ground plane noise sources, necessitating elevated mounts.

The statistics for the position quality and standard deviation of GPS displacement estimates show a slight elevation in the case where no mount was used, but still this is not an appreciable increase. The GDOP is markedly higher in the latter case due to the lack of elevated mount. Though the satellite conditions were predicted to be nearly identical during both tests, this prediction is based on the mask angle being preserved in both cases. This was not the case for Test 6b, where obstructions blocked at least one satellite from view. In this respect, the lack of elevated amount can have negative influences in terms of GDOP and PDOP if it permits obstructions of satellites for the antenna. Consequentially, the first few epochs of Test 6b suffered from ambiguity problems, possibly due to a nearby obstruction shielding some satellites. No ambiguity problems

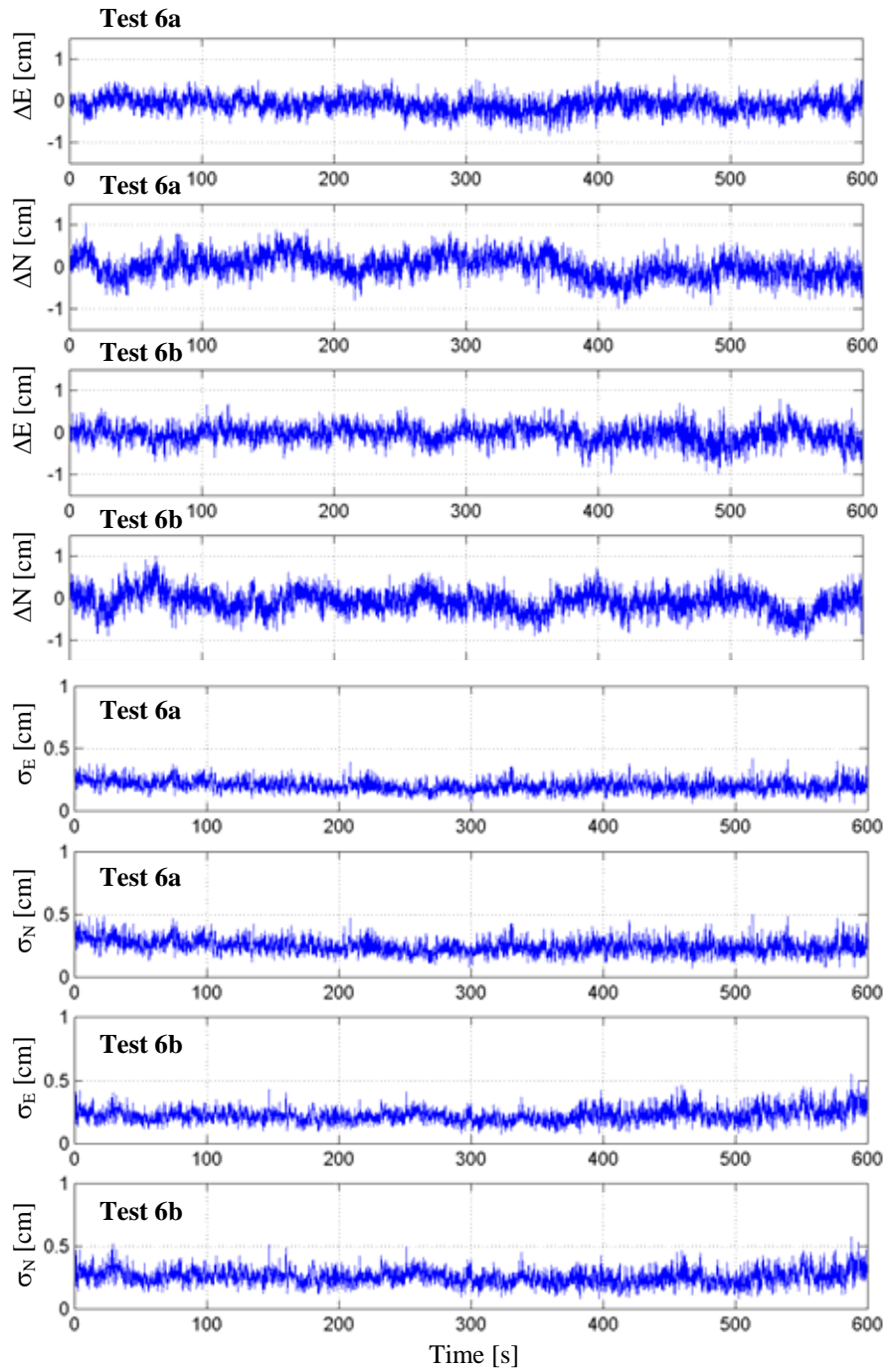


FIGURE 12.25. GPS displacement estimates for Test 6a-b and standard deviations of GPS displacement estimate

were experienced by Test 6a due to the antenna's elevation. Therefore the use elevated mount has similar merit for improving the satisfaction of mask angle requirements.

12.9 Recommendations for Full-Scale Application

Based on the findings of the calibration tests conducted in this chapter, the following recommendations are made to achieve the best possible performance in the full-scale application:

- The performance of the GPS is highly dependent on its ability to view the sky without obstructions. A maximum of 15° mask angle or preferably less must be maintained in all quadrants. Any unavoidable obstructions, e.g. due to neighboring buildings or equipment, can shield orbiting satellites from review, increasing DOP errors and degrading GPS performance. The use of an elevated mount may improve the ability to maintain this mask angle requirement.
- The DOP is not an issue simply of the number of satellites, but also a measure of the optimality of their orientation. Therefore, the tracking ability of the GPS is time-varying based on these orientations. Thus the performance of the GPS tracking documented in this chapter should be referenced to the DOP at the time of the survey and may be enhanced even further under more optimal DOP scenarios.
- Reflective surfaces can bounce satellite signals and cause multi-path errors. The use of choke-ring antennas can minimize these effects; however the final

installation of the antenna should avoid direct proximity to reflective or metallic surfaces either adjacent to or below the unit.

- Based on manufacturer recommendations, the GPS antenna should be elevated a minimum of 3 feet above the surface in the final installation to reduce noise effects. Though this was not observed in testing due to the pristine environment, it is still recommended for full-scale application.
- In the work by Ashkenazi et al. (1997), significant degradation of the GPS accuracy was attributed to vibrations of the stand on which it was mounted. Thus it is critical that the antenna's mount is completely rigid, as discussed in Chapter 13.
- Position quality and GPS standard deviation measures should be used in conjunction with the aforementioned noise thresholds for a reliability measure. Dynamic testing has revealed that quality tracking in terms of averaged measures like standard deviation can be achieved consistently when the signal-to-noise ratio is 200% or more. This corresponds to motions above ± 1 cm. The errors in peak estimation are consistently mitigated for signals with above ± 2 cm. At sufficiently large amplitudes, the GPS system is capable of tracking displacements with comparable quality regardless of frequency, however, for low amplitude motions, tracking at lower frequencies is superior.
- This performance is enhanced even further for longer duration monitoring, in which it was observed peak values could be even more accurately captured when signal-to-noise ratios were larger than 300%. Thus the longer duration

of full-scale applications is of direct benefit, as shown using synthetic building motions.

- Lighting protection should be used in full-scale application as its effects on the quality of GPS tracking ability are negligible.
- The angle defining the axis of motion should be approximated in the field by handheld GPS sensors and then affirmed or refined in post-processing using a simple trigonometric relationship.

CHAPTER 13

GPS MONITORING IN URBAN ENVIRONMENTS: DATA MINING AND INFORMATION PROCESSING

13.1 Introduction

This chapter summarizes the implementation of the GPS components in Chicago, as part of the full-scale monitoring program overviewed in Chapter 9. Preliminary data from the GPS investigations is presented herein, as well as some of the issues associated with processing GPS measurements in urban environments.

13.2 Identification of Reference Site

Within the differential GPS configuration detailed in Chapter 10, the resolution capabilities of the GPS at the monitored building, or rover, are greatly enhanced through the addition of a nearby reference station configured with the same GPS unit. As discussed at the conclusion of the previous chapter, the identification of a stationary structure of sufficient height nearby the rover station, in order to minimize baseline separation errors, can be challenging within the city environment, particularly since this reference station must be of sufficient height to provide the GPS antenna an ample view

of the sky. As a compromise, a moderate height structure, for which relations with the building owners were well established, was selected. The structure is a 23-story, steel-framed building with cast-in-place reinforced concrete slabs, standing 264 ft. above street level, with two levels below grade. The building was first occupied in the spring of 1925 and interactions with long-time building owners and engineers indicate no significant movement in the structure over the last 30 years, due in part to the fact that the building is shielded from the direct effects of wind due to surrounding buildings. This reference station is located approximately 0.8 miles (1.29 km) from the monitored rover station at Building 1, yielding a RTK GPS accuracy of 7.58 mm, according to the expression in Table 11.1.

13.3 Installation of GPS Components in Full-Scale

The following sections detail the various components of the GPS within its full-scale application. The units and all supporting electronics were installed at the reference site on August 26, 2002 and at the rover site the following day and have been manually triggered over different monitoring periods to document the displacements of Building 1.

13.3.1 Antenna Mounts

As indicated by Ashkenazi & Roberts (1997), the influence of antenna mount dynamics on GPS tracked displacements can be quite significant. As a result, mount configurations producing minimal displacements, yet consistent with the mounting constraints at both the reference and rover stations, were requisite. The height of the mounts was minimized as much as possible to limit potential vibration levels, while still allowing the antenna a

minimum of 3 feet of clearance above neighboring obstructions on the building rooftop. The mount for the rover installation at Building 1 was comprised of three feet of galvanized pipe with inner diameter of 2.5", as shown by Figure 13.1. These mounts were designed to slip over protruding pipes on a pre-existing frame atop the building's penthouse, as shown by the schematic in Figure 13.2, with bolts at two levels on the mount's elevation bearing the pipe snugly against the frame. An aluminum cap was machined to fit slip into the mount pipe and was outfitted with a 5/8" x 11 pitch bolt with 1" of thread exposed so the GPS antenna could be securely screwed in place. Any exposed surfaces were primed and painted to reduce reflectivity and potential for corrosion.

For the reference station, a similar galvanized pipe configuration was anchored directly to a masonry wall structure on the penthouse roof using standard pipefittings. Segment A, shown in Figure 13.1, was 48" in length, allowing it to readily rise above this masonry wall. This segment threaded into a second length of pipe, segment B, which was anchored to the masonry wall at its base and top to securely fasten the assembly and limit any potential of differential motion. The placement of this antenna at this location was quite critical, and its current position just south of the cooling tower at the southwest corner of the building gave the maximum view of the sky to the southwest and northwest with minimal obstructions due to neighbors and surrounding rooftop structures. The southeast and northeast quadrants are obstructed to some degree by neighboring buildings, potentially obscuring satellites orbiting at elevations below 45°. At the rover, being considerably taller, the issue of neighboring obstructions was not as prevalent. The antenna was mounted on the aforementioned pre-existing support frame at the building's



FIGURE 13.1. Reference and rover antenna mounts fabricated for full-scale application

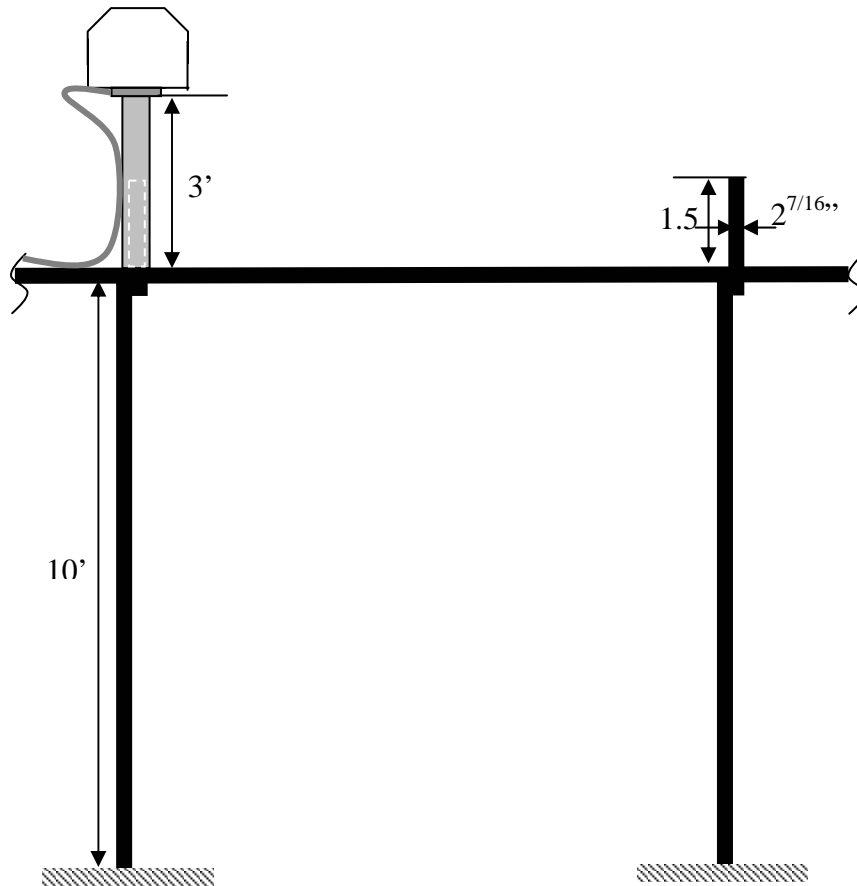


FIGURE 13.2. Schematic of GPS antenna placement on rooftop frame of Building 1

approximate centerline, thereby eliminating any potential for torsional displacement tracking and providing pure sway response along the buildings primary axes, which incidentally align with true North and West. The GPS antennas in their final rooftop positions on the two buildings are shown in Figure 13.3.

13.3.2 Grounding

As discussed in Chapter 11, this system was outfitted with in-line lightning surge protection. The two lengths of coaxial cable connecting the GPS receiver to the antenna



FIGURE 13.3. Fully installed GPS antennas at Building 1/rover site (left) and reference site

were run in advance of the component installation and were then linked near a grounding point using the Huber + Suhner (H+S) Lightning Protector, discussed in Chapter 11. A grounding lug attached to a 6 AWG cable running from this device (see Figure 13.4) was then welded to the grounding bar in Building 1 to completely engage the lightning deterrent system and prevent the possibility of lightning strikes damaging the receiver and its electronics. In Building 2, a similar end was achieved using a grounding clamp affixed to a grounded conduit on the building's cooling tower. To protect the capsule, the interface was bound in self-vulcanizing tape, as shown in Figure 13.4.

13.3.3 Receiver Cabinetry

As mentioned in Chapter 11, the GPS electronics are comprised of the GPS receiver, a laptop and a power supply (UPS). The system is powered from the building through a standard AC receptacle and is interrogated remotely using the computer's modem. Since the system is intended for remote operation and could potentially freeze, a PSTONE

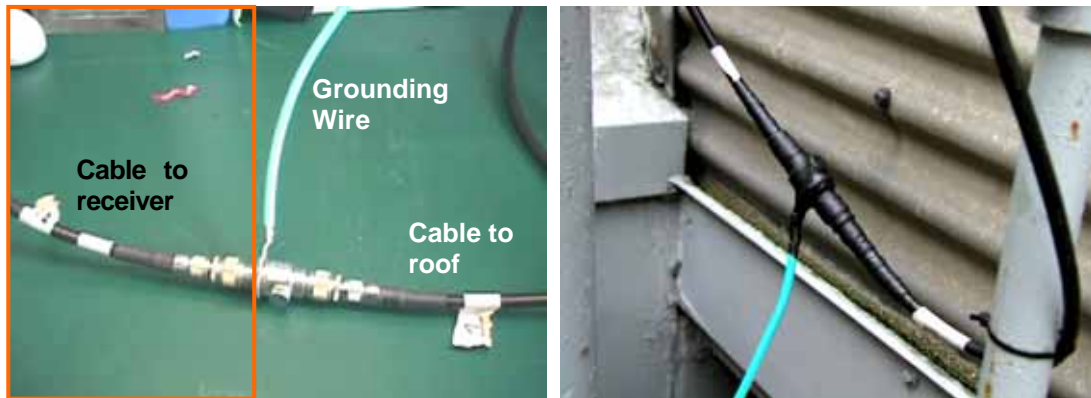


FIGURE 13.4. In-line lightning protection with grounding wire (left) and installed in full-scale at reference site

telephone activated power controller was also included in the final configuration to allow the project team to terminate power to the unit at any time and force a re-boot of the system. Each of these four components is shown in its final orientation within the metal instrumentation cabinet in Figure 13.5. The enclosure is ventilated by two 4.7” muffin fans, a vented shelf, and two additional circulation vents to satisfy the environmental constraints detailed in Section 11.2.4. These cabinets were placed on the highest mechanical floors of the reference and rover buildings, elevated by rigid stands to prevent potential damage due to pooling water and to elevate them above any existing machinery, as shown by the images in Figure 13.6. Note the rover unit is positioned directly below the datalogger cabinet discussed in Chapter 9.

13.4 Monitoring Program

The post-processing configuration assumed for this study requires that the GPS be remotely triggered through the use of the PC Anywhere software discussed in Section 9.7. The GPS post-processing PC at Notre Dame utilizes PC Anywhere to access the

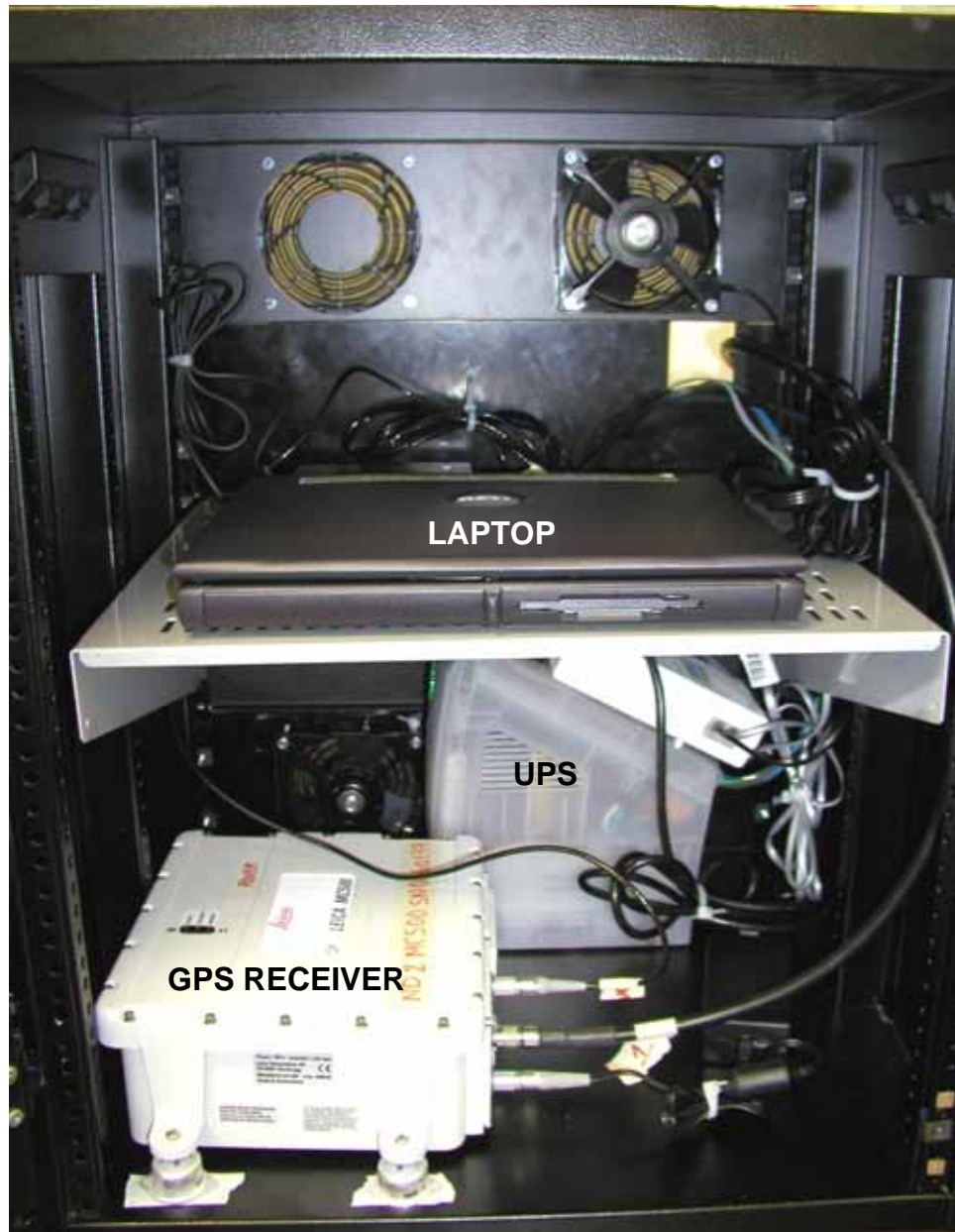


FIGURE 13.5. Zoom of GPS cabinetry contents installed in full-scale program



FIGURE 13.6. GPS Instrumentation cabinet in place at reference site (left) and at rover site just below data logger cabinet in Building 1

SOM hub computer in Chicago via Ethernet. A second PC Anywhere application is launched on that computer, a process termed by this researcher as the “Chain of Hosts” configuration, and uses a modem connection to then individually interrogate the laptops associated with the reference and rover stations. This interface allows complete control of all the files and applications on these computers. Through this Chain of Hosts, Control Station can be launched on each laptop and the ring buffers can be activated to initiate the data acquisition. The modem connections can be dropped and then re-established hours or days later to terminate the data acquisition via Control Station. Next the raw GPS ASCII files of satellite data from the receivers are downloaded to the on-site laptops, and then transferred offsite to the SOM host computer via FTP by modem, and finally by FTP

through Ethernet to the Notre Dame analysis portal where the data is post processed. Though this configuration has several nodes, it provides a cost-effective means to transmit large amounts of data from Chicago to the university without the expense of long distance communications.

The GPS has been triggered thus far in the study to capture four types of events: 1) nighttime monitoring periods with minimal wind, in order to determine a baseline position for the building; 2) 24-hour monitoring programs with minimal wind, to identify thermal effects; 3) monitoring of significant wind events to capture dynamic response characteristics and displacement due to mean winds; and 4) follow-up monitoring approximately 24 hours after a significant wind event for use as a repeatability measure against multi-path effects. The processing approaches utilized are discussed in the subsequent sections. Selected data will be presented in this chapter to demonstrate some features of GPS sensing technology. The records utilized for this purpose are listed in Table 13.1.

13.4.1 Modifications to Post-Processing Routine

In the post-processing of the full-scale data, some parameters were changed from those used in the calibration studies discussed in Section 11.6. The solution type was modified to Iono Free Fixed as it has the capability to remove ionospheric disturbances over the longer baseline in the full-scale application. Since all the monitoring in full-scale is conducted over periods of hours and even days, there is always sufficient information to build an ionospheric model from, justifying the use of the Computed Ionospheric Modeling feature in SKI-Pro. All data is viewed within the local *Chicago East*

TABLE 13.1

MONITORED DATES OF INTEREST

	Monitoring Interval (CST)	RB	No. Files	Environmental Condition	Purpose
11/13/02	16:45 – 21:51	0	6	Low winds, evening	Baseline
11/14/02	17:45 – 21:53	1	6	Low winds, evening	Baseline
11/30/02	11:12 – 15:00	2	9	Strong mean winds (~30 mph)	Dynamic Monitoring
1/7/03	12:38 – 15:36	0	7	Front moving through	Dynamic Monitoring
1/8/03	12:29 – 15:36	1	7	N/A	Multi-path Follow-Up

NOTE: RB = Ring Buffer Number

Coordinate System based on the Illinois East NAD83 grid. In the full-scale application, the satisfaction of ambiguities can be more difficult due to the limited satellite availability at the reference station, which can fall to as low as 4-5 satellites at times due to obstructions in the northeast and southeast quadrants. As a result, positions flagged with “yes” and “yes*” ambiguity statuses are retained. All data flagged as “no” are discarded.

13.4.2 Preliminary Baseline Position

In order to meaningfully interpret static displacement data, a baseline position must be established for the rover structure. Ideally, this would imply monitoring the building over an extended period free from thermal effects, wind-induced response or significant GPS errors to establish its undeformed position. Tamura (2002) determined a baseline position using extended monitoring over a three-month period during which time only data meeting three conditions were considered: data obtained at night to eliminate thermal

effects, data obtained when wind speeds were relatively low to eliminate wind-induced response, and data collected under satellite configurations for which PDOP was less than 2, which is very high precision data. The mean of the data meeting these criteria over three months was then used to establish his baseline building position. Though a similar baseline position in the local coordinate system (X_E^0, X_N^0) is being calculated during the spring of 2003 for this ongoing monitoring program, a preliminary baseline position was identified early on so that the data collected in the subsequent months could be analyzed in the interim. Since, for the purposes of discussion in this chapter, only relative displacements are of interest, a lack of complete precision in this preliminary baseline is not of great consequence. This preliminary baseline was determined on the evening of November 14, 2002 by taking the mean position of the building in the local coordinate system (X_E, X_N) over a nighttime interval during which the wind speeds were relatively low. On that day, the sun set at 16:31 CST and twilight concluded at 17:01 CST. As shown in Table 13.1, data was collected soon thereafter at 17:45 CST. Over the next four hours, the mean wind direction was 45° deg, i.e. the northeast, at an average mean hourly wind speed of 17.7 mph, holding relatively stable and even diminishing slightly over the monitoring period. The temperature over the monitoring period began at 43°F , dropping to 41.7°F midway through and rising again to 42.2°F at the end of the monitoring period. Thus, the net temperature change was less than a degree over the monitoring period. The prior day, data was also taken after sunset, this time beginning at 16:45 CST following a sunset at 16:32 CST. Over this monitoring period, winds were from the southwest (226°) and ramped up during the second half of the monitoring period, to achieve an average mean hourly wind of 23.2 mph at the lake level sensor discussed in Chapter 9. The air

temperature began at 55°F and dropped to 52.1°F before rising again to 54.5°F at the end of the monitoring period, leading to a net temperature change of a half-degree. These environmental conditions are summarized in Table 13.2. Of the two days, the measurements on 11/14/2002 represent a more stable wind condition, without the ramping observed on the prior day, and will be used as a preliminary baseline position for this chapter.

The mean positions of Building 1 over these two monitoring periods are also shown in Table 13.2. Note that the mean position on 11/13/2002 is 1.62 m more to the east and 2.6 m more to the north than its counterpart the following day. This observation is consistent with the wind conditions on those days, summarized in Table 13.2. On 11/14, with lower winds out of the northeast, the building was displaced to the south and west of its original position. On 11/13 the winds were coming from the opposite direction, pushing the building north and east. Due to the higher wind speeds on 11/13, the building not only moved back to its centerline from its displaced south-west position on 11/14, but also likely extended further to the north and east due to the increased wind speeds. This is visualized in Figure 13.7. Again, 11/14 will be used as the preliminary baseline position for subsequent discussions, since relative positions are the primary point of interest. Still it should be kept in mind that this preliminary baseline is likely displaced south and west of the true undisturbed position, which will be determined in the future work, discussed in Chapter 14. With a preliminary baseline position in hand, the remainder of this chapter will now focus on some specific interference issues and systematic error sources that present unique challenges in urban monitoring.

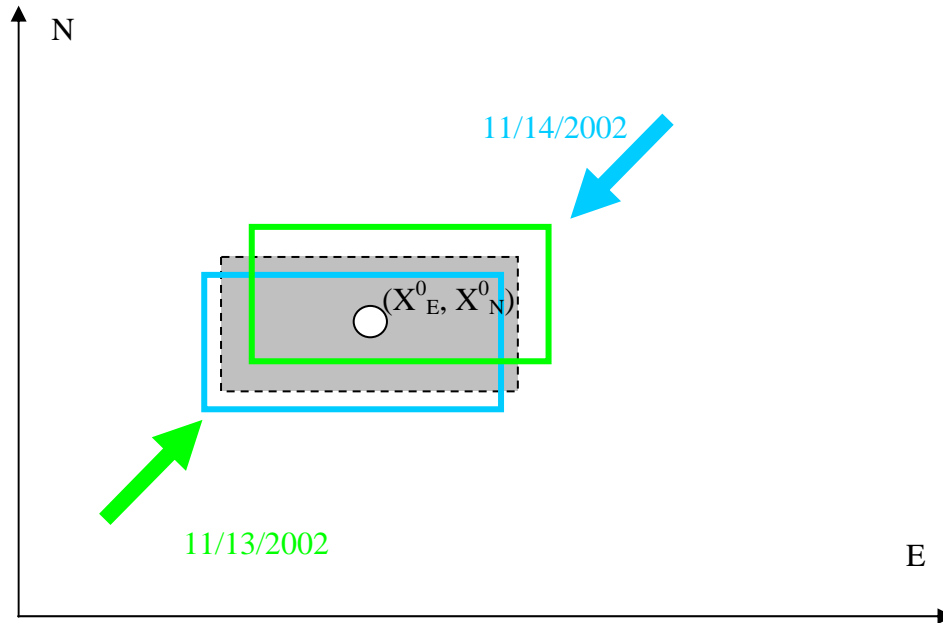


FIGURE 13.7. Preliminary baseline position from monitoring on 11/14/2002 and comparison with displaced position on 11/13/2002

TABLE 13.2

PRELIMINARY BASELINE POSITION DETERMINATION

	X_E [m]	X_N [m]	σ_E [mm]	σ_N [mm]	Net Temp.	Average Wind Speed (Direction)
11/14/2002	358936.3199	581116.5462	4.39	5.22	-0.8° F	17.7 mph (46°)
11/13/2002	358937.9430	581119.1471	4.66	4.69	-0.5° F	23.2 mph (226°)
ΔX	+1.62 m	+2.6 m				

NOTE: Wind speed is average of mean hourly winds over the monitoring interval, taken by the lake level anemometer. Net temperature is the difference between the air temperature at the end of the monitoring period and its value at the beginning.

13.5 Radio Frequency Interference

As GPS moves into urban environments, one major concern is Radio Frequency Interference (RFI) inhibiting the ability of GPS to lock onto and track satellites. RFI is characterized by a sudden loss of satellites or unexpectedly low signal to noise ratio. This noise is represented by the position quality measures discussed previously, which capture thermal noise inherent to the receiver due to the random motion of electrons in its circuitry, as well as the natural emissions of ground or atmospheric radiation and the contributions of interfering transmitters. If an interfering radio signal is received along with the GPS transmission, it is also modulated with the code replica during the correlation process, essentially providing artificial white noise spread uniformly across all frequencies. Thus an increase in the position quality measures introduced in Chapter 12 is one way to document potential RFI. This interference effect can also prevent the receiver from operating at all or causing it to completely lose its lock on the satellite signals.

As discussed in Butsch (2002), such interference is often associated with the GPS L2 frequency due to the use of amateur pocket radio transmitters occupying the band from 1240 to 1243.25 MHz. GPS receiver manufacturers are now including additional bandpass filtering in their receiver designs to limit this problem and incorporating RF jamming protection, a feature of the Leica MC 500 unit used herein. Still, the presence of two-way communications transmitters and receivers in the vicinity of the GPS reference and rover was an initial concern. A survey of the communications devices in the immediate vicinity of the antennas confirmed that transmissions broadcast and received

were at 931 MHz or less, appreciably below the L1 and L2 frequencies used by GPS. To date, no complete loss of tracking ability has been observed in this application.

13.6 Multi-Path Interference and Identification

As discussed in Section 10.7.2, multi-path errors remain the most significant concern in urban environments. Their identification and removal from GPS displacements is an important consideration in any full-scale application. Obviously, the most direct remedy is to mitigate their presence at the source, given that the reflected signals can be deflected at the antenna and thus not considered outright, i.e. through the choke ring antennas used in this study. Though this is an important remedy, delayed versions of the signal reflected from surfaces above the antenna plane can still be received by choke ring antennas, producing multi-path effects. For this reason, residual multi-path effects must be treated within the receiver hardware or through signal processing remedies within the GPS solution process. The key difficulty in the latter strategy lies in the fact that multi-path cannot be removed by signal processing approaches if the distance between the direct signal and the reflected signal is less than a few meters. Fortunately, this is not the case in most situations. Nevertheless, manufacturers of GPS receivers are now working toward developing analysis frameworks that can identify, isolate and remove the traces of multi-path errors in satellite data, thereby removing it directly from the output displacement estimates (e.g. Van Nee, 1995) or incorporating hardware features to prevent the false lock points associated with the multi-path problem (see www.javadgps.com). This however is an area of research that has not fully materialized in current receiver technologies, though making progress.

In lieu of such technology, the following protocol has been established to treat the possible presence of multi-path errors in the data collected in this full-scale monitoring program. As these errors are systematic in nature and therefore not reflected in the position quality measures, which are more indicative of the random noise in the solution, a different means of identification is requisite. First, consider the fact that not all the satellites in a given constellation are responsible for transmitting signals that are reflected to cause multi-path errors. Rather, one or two satellites at a given time tend to be the culprits, having an azimuth and elevation that places them in such an orientation that their signals can be reflected off of nearby reflective surfaces located above the GPS antenna. Thus, one strategy would require a review of the satellite orientations throughout a complete calendar day to identify at which times a given satellite is oriented in such a way that their signal is likely being intercepted by the multi-path reflector source – if it can be identified. In post-processing, these satellites can be appropriately omitted.

However, it would be advantageous to develop a strategy to treat multi-path effects through secondary post-processing of the GPS displacement data, not requiring the labor-intensive identification and removal of interfering satellites. Since multi-path errors manifest themselves locally as long period fluctuations in the data on the order of several minutes in period, they can be identified and de-trended from the displacement data. This approach was exploited by Chen et al. (2001) in their monitoring of the Di Wang building, but the excessive filtering through a coarse discrete wavelet used in that study removed all trace of static and quasi-static displacements, leaving only the resonant displacements that could have been recovered just as easily from accelerations.

Instead, this on-going study will utilize some additional strategies to identify multi-path periodicities. One feature to exploit is the fact that the reflected satellite signal inducing multi-path is received by the GPS, the position is calculated based on this corrupted signal, and then decomposed onto the local grid coordinates of north and east. Therefore, any periodicity of the systematic GPS multi-path error should be approximately the same in both the north and east components, though of potentially different magnitude and even phase. Thus the spectra for east and north position can be examined for shared frequency components that are likely caused by systematic errors, since wind effects will not manifest identical periodic trends in both response directions. One example of such a removal is provided herein for data acquired on November 30, 2002. The power spectra of the northern and eastern relative displacements are shown in Figure 13.8. The resonant response associated with the fundamental sway modes is evident in each, with the northern displacements capturing the 0.142 Hz sway frequency along that building axis and the eastern displacements containing the 0.206 Hz sway frequency in the opposite direction. The mean hourly winds at the time this data was acquired were 29 mph at the lake level sensor discussed in Chapter 9, coming out of the north at 340°. Thus, the displacements along the northern coordinate represent alongwind response and the displacements along the eastern coordinate are indicative of acrosswind sway. Again, the placement of the antenna was such that torsion is not detectable.

A low-frequency periodic component near 0.025 Hz is detected strongly in the eastern coordinate, shown by the arrow in Figure 13.8b, as well as in the northern coordinate in Figure 13.8a. A second-order Chebyshev bandstop (notch) filter was utilized to remove this periodic component. The resulting displacement time histories are

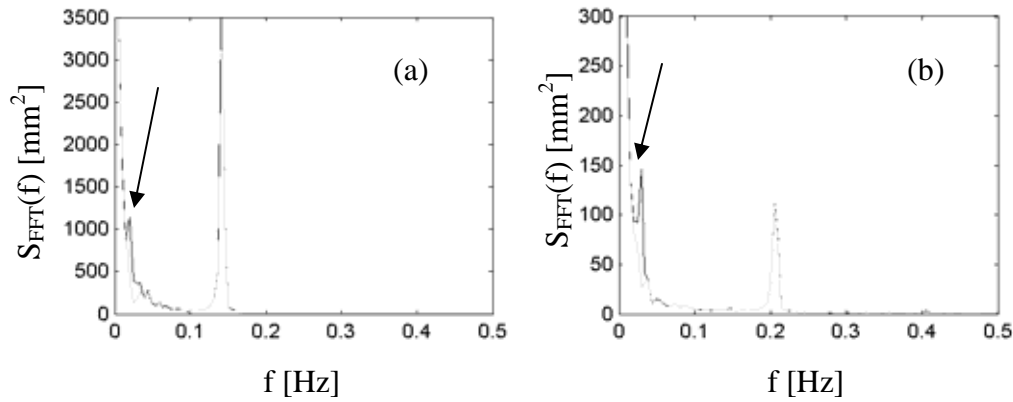


FIGURE 13.8. Fourier power spectra of relative displacements to the (a) north and (b) east: original data in black, filtered data in gray

shown in Figure 13.9. Note that both displacements still manifest upward ascent at the end of their respective records. To discern if this is a remaining feature of multi-path effects, the noise thresholds introduced in Chapter 12 are applied. This comparison is facilitated by examining the resonant component of the response filtered using a second-order Chebyshev bandpass filter relative to these noise thresholds, as shown in Figure 13.10.

The thresholds are elevated relative to the levels observed in the calibration tests of Chapter 12. In those studies, the thresholds were on the order of 5-7 mm whereas they can be more than double that in full scale. Recall that due to the baseline separation alone, as discussed in Section 13.2, the RMS dynamic resolution was elevated by over 2.5 mm. Considering the noise level in the urban environment, noise thresholds of these levels should not be alarming. What the levels clearly demonstrate is that the resonant displacements in this case were generally at or below the noise thresholds for the system. Note for example, at 800-1000 s, the northern response is greater than the noise threshold

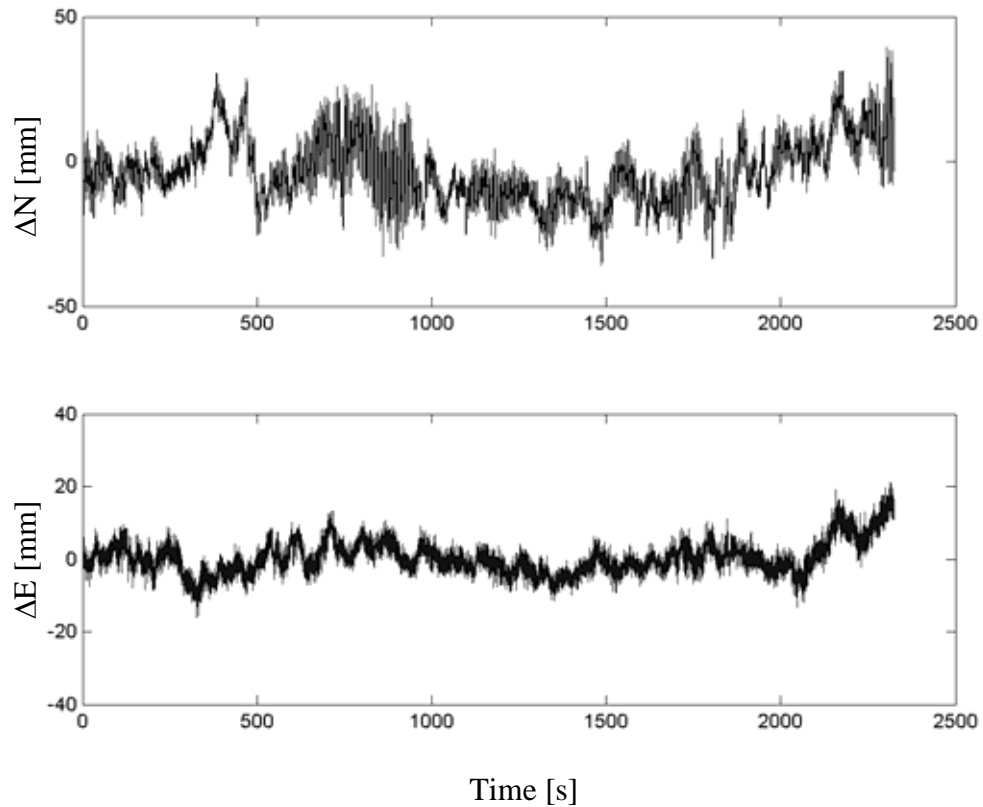


FIGURE 13.9. Filtered displacement data for 11/30/02

and is thus taken as reliably tracked. The eastern displacements are markedly less, however. Still, referring back to Figure 13.8 It is reassuring to note that despite the low amplitude crosswind displacement response, the fundamental frequency along this axis was accurately identified.

Revisiting the issue of the escalating displacements at the conclusion of this record, the degrading error thresholds in Figure 13.10 clearly indicate that this is not a multi-path effect. Instead, the degrading accuracy is reflected in the noise thresholds, which do not inherently account for multi-path, but are indeed influenced by DOP and satellite availability, as well as other noise sources. The log file for this data revealed that

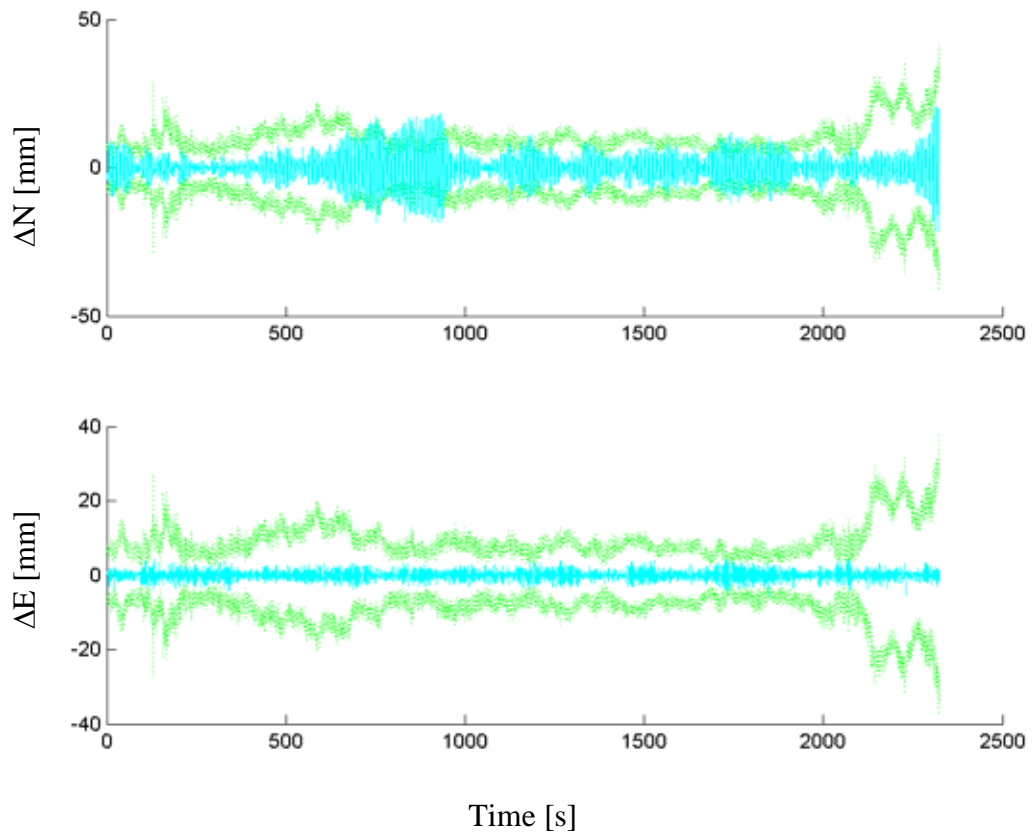


FIGURE 13.10. Resonant displacement data for 11/30/02 with error thresholds (green)

a satellite at the reference station was obstructed for a period of time. The gradual loss of this satellite began to degrade the DOP, elevating the noise thresholds as shown just beyond the 200th second of Figure 13.10. This example demonstrates the importance of noise thresholds in analyzing full-scale GPS data and determining the quality of the tracked positions. These noise thresholds are indeed a clear merit of a post-processing protocol. Finally, a zoom of the resonant response data is shown in Figure 13.11 to demonstrate the tracking ability. The jaggedness of the eastern displacement values is again the result of these displacements falling well below the noise thresholds.

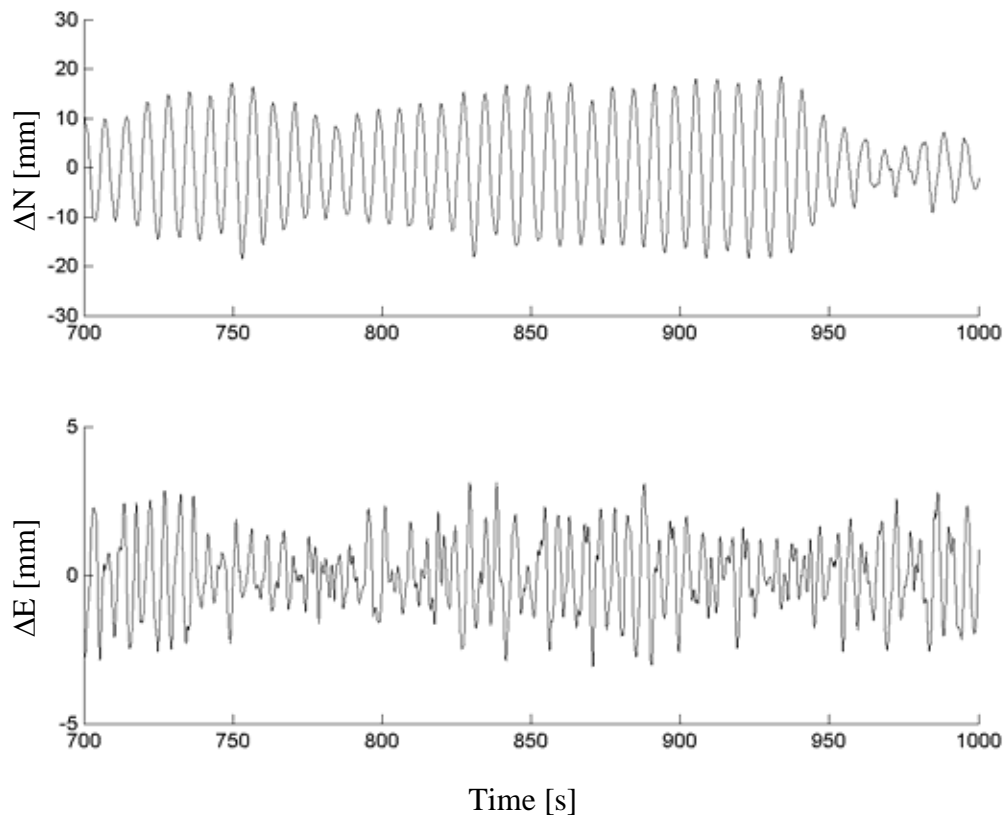


FIGURE 13.11. Zoom of resonant displacement data for 11/30/02

This simplified analysis using the power spectra of the two displacement directions does not however account for multi-path effects that are of longer period, say of a minute or more, which are consequently embedded in the large DC component of the spectra and are difficult to separate from thermal and background wind components. However, there is another characteristic of the multi-path phenomenon that can be explored. Since the multi-path sources are permanent, e.g. masts, cooling tanks or neighboring buildings, their positions are fixed. Therefore, as the satellites orbit and sweep past those locations every sidereal day (every 23 hours and 56 minutes), the signals should be reflected off of those permanent fixtures in the same manner as the day

prior. This repeatability provides a means to compare data measured on two consecutive days, shifting the second day's observations by four minutes, and then examining the time histories and power spectra to identify strong low-frequency periodicities and subsequently filter or detrend them from the data.

To demonstrate this approach, data was taken on January 7, 2003 and the measurements were repeated on January 8, 2003, four minutes earlier, for comparison. The data shown in Figure 13.12 was acquired between 15:00 and 15:30 CST. During the monitoring interval on 1/7/2003, the mean wind speed was approximately 30 mph at lake level and approaching from the west at 290° . The following day, the winds were comparable, approaching from approximately 270° . In this case, the response detected in the eastern direction corresponds to alongwind response and the northern response carries the acrosswind component. The data was low pass filtered using a second order Chebyshev filter to separate the quasi-static components in order to better distinguish the potential multi-path effects. This filtered data is shown in Figure 13.13. There appears to be no repeatability manifested in the low-frequency components between the two days. Thus, it can be assumed that all the quasi-static components of response are associated with the background component of the wind. For reference, the resonant components of the response from this event are shown in Figure 13.14. Note that, although the wind speeds are approximately the same as the earlier event on 11/30/2002, the westerly wind direction generates larger displacements along the eastern axes, particularly on 1/08/2003 as the wind comes from due west. Although no clear multi-path trends like those described in Chen et al. (2001) were observed in the data presented here or other collected thus far, it is likely to be encountered during the course of the extended

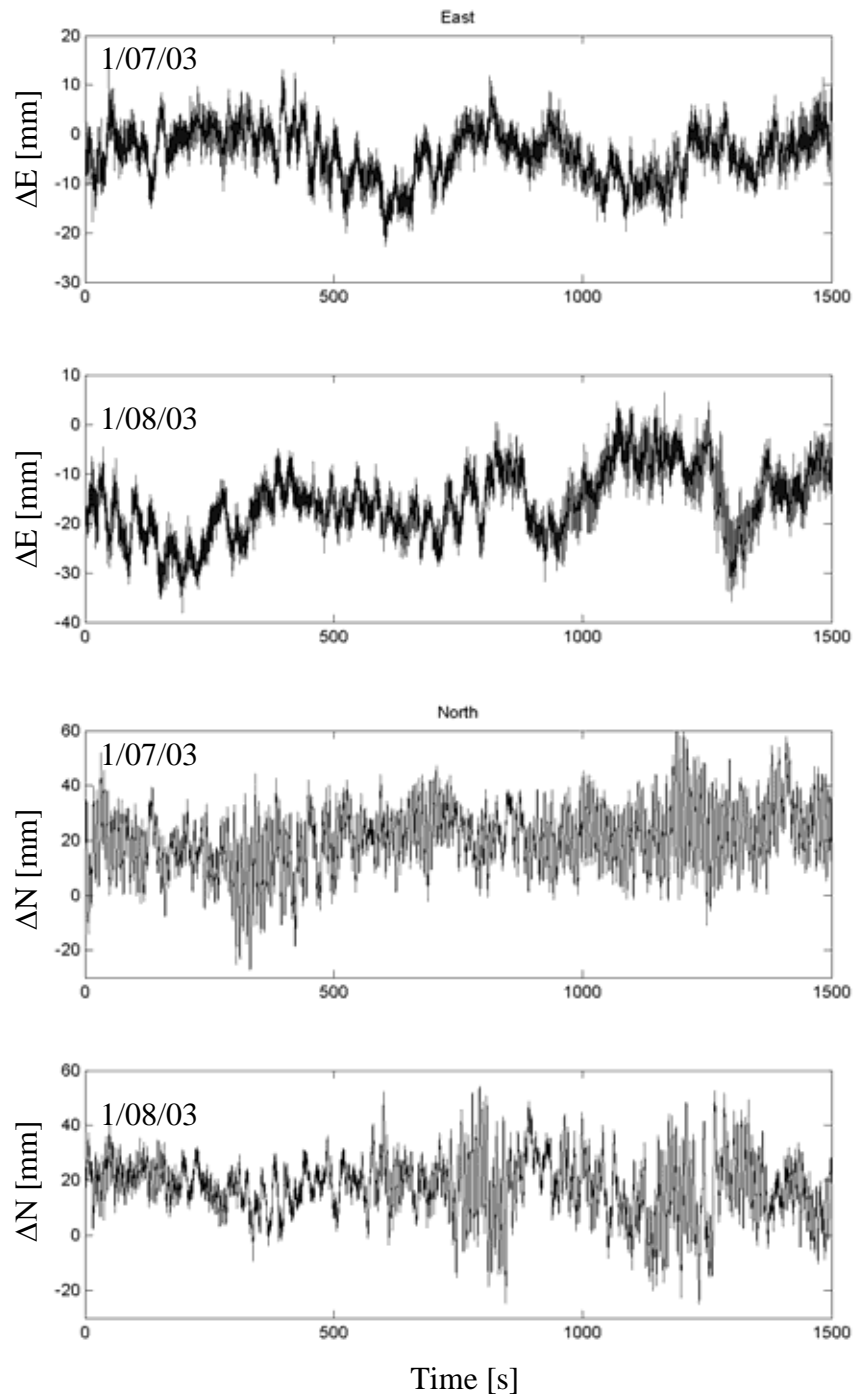


FIGURE 13.12. East and north relative displacements on consecutive sidereal days (data for 1/08/03 has been shifted 4 minutes)

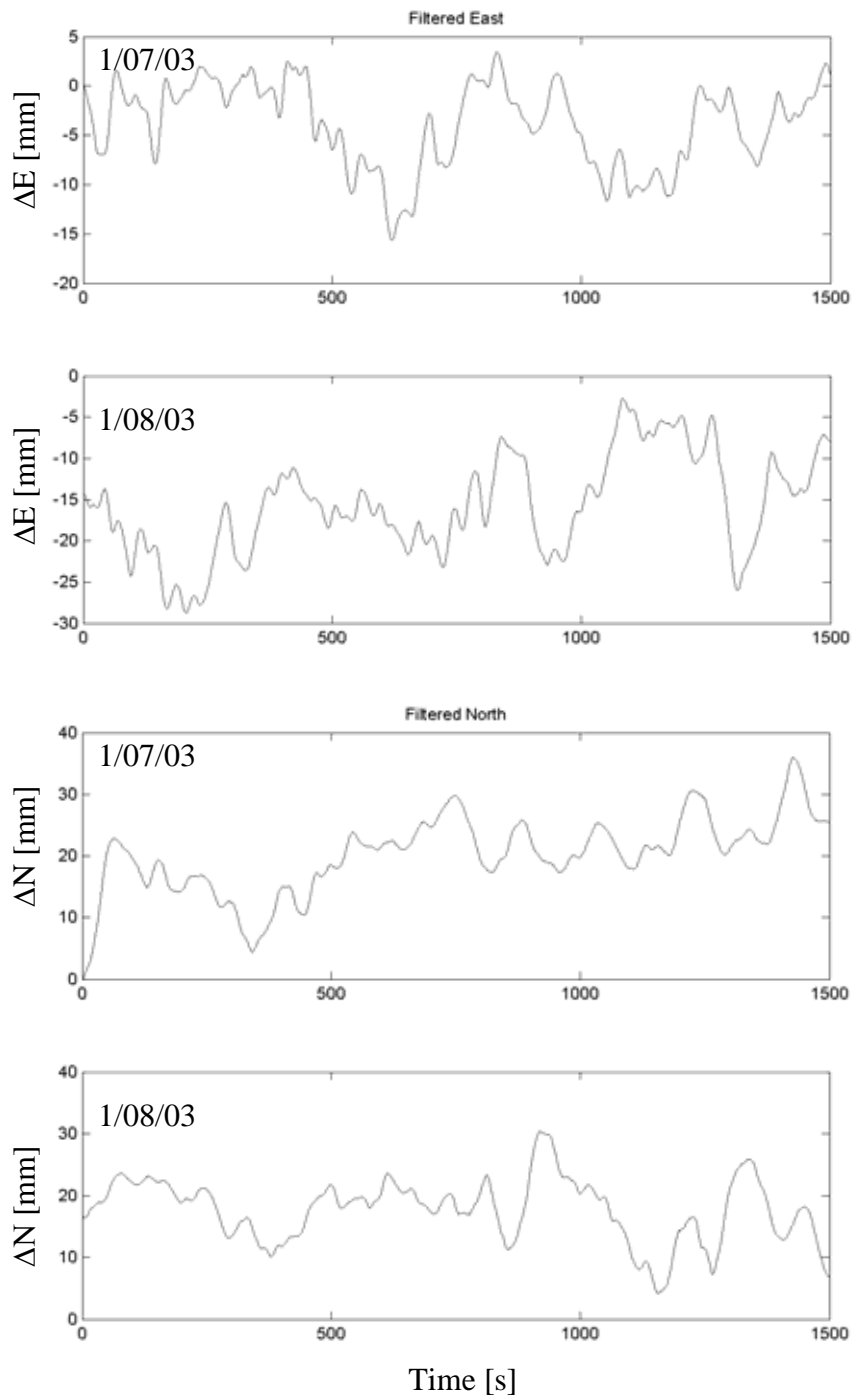


FIGURE 13.13. Quasi-static east and north relative displacements on consecutive sidereal days (data for 1/08/03 has been shifted 4 minutes)

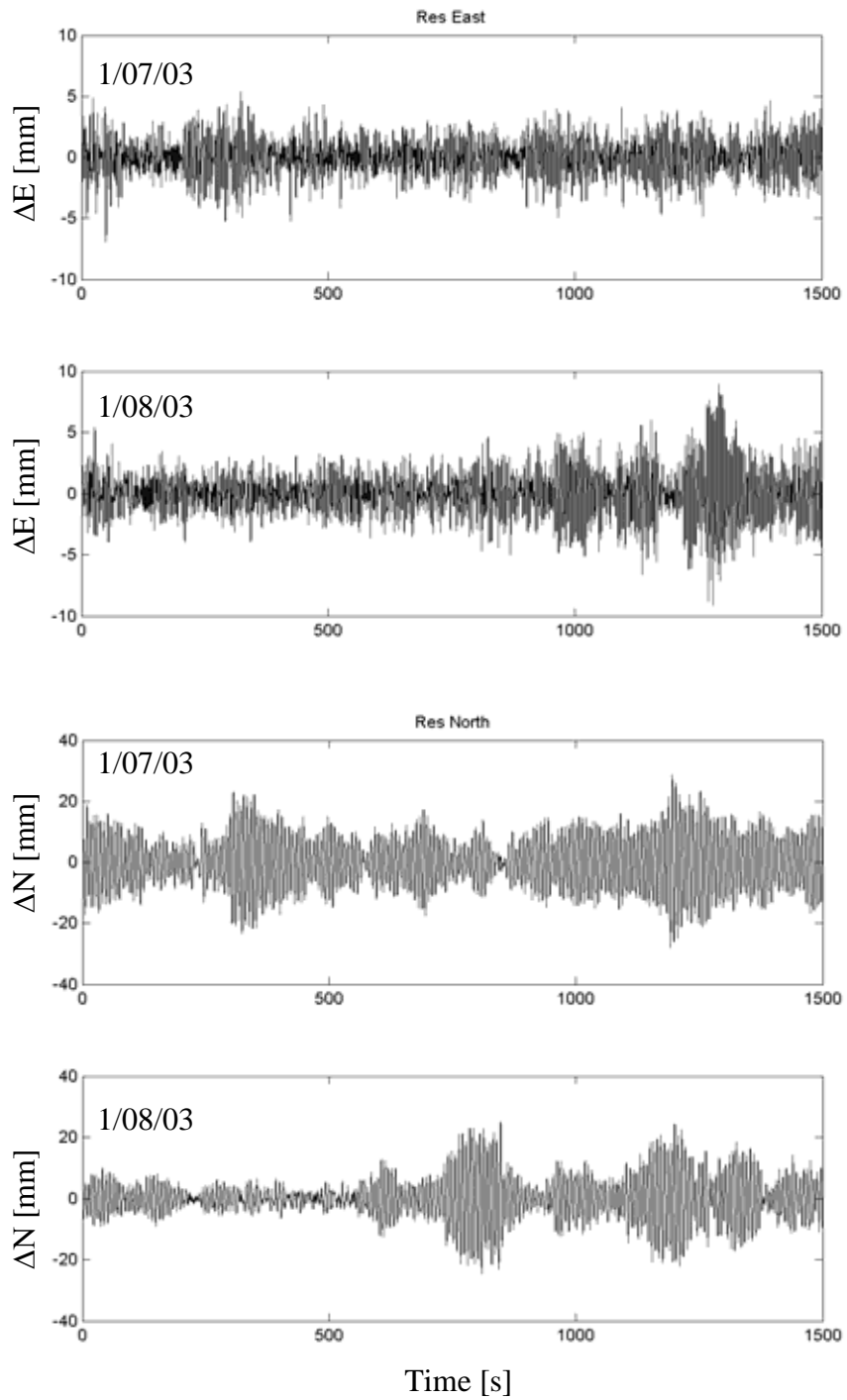


FIGURE 13.14. Resonant east and north relative displacements on consecutive sidereal days (data for 1/08/03 has been shifted 4 minutes)

monitoring program. Therefore, continued analysis using the evaluation techniques offered in this chapter will be required.

13.7 Assessment of System Performance in Full-Scale

This chapter presented the installation of a GPS sensor pair for monitoring the displacements of a tall building in Chicago. Thus far, the system has been manually triggered on a number of occasions to evaluate its performance in full-scale. In light of the increased baselines and interference sources, the noise thresholds were expected to be elevated in comparison to the calibration studies. Though this elevation was by no means alarming, this situation does require motions of the building on the order of a few centimeters to be reasonably tracked. The primary difficulty that has been encountered thus far is the ability to consistently resolve ambiguities. This arises from the fact that the DOP at the reference station is often quite high (4-6) due to the obstruction of lower elevation satellites in the eastern quadrants. At times, the number of satellites at this site can be reduced to 4 or 5. This increases the errors in the tracking and at times, makes ambiguity solutions impossible. As a result, there may be pockets of data on the order of an hour in length that cannot be utilized. On the other hand, the rover can at times track up to 8 or more satellites. Clearly, the present study is only limited by the location of the reference. One way to overcome this difficulty would be to relocate the reference station to a more unobstructed location. In the meantime, the data satisfying the ambiguity checks can be evaluated using the multi-path analysis strategies provided herein, and using the noise thresholds to distinguish the significance of drastically escalating position

estimates. This again reiterates the importance of a post-processing protocol in providing such reliability measures to critically evaluate the accuracy of the GPS position estimates.

CHAPTER 14

CONCLUSIONS AND FUTURE DIRECTIONS

The state-of-the-art in Civil Engineering is rapidly advancing and with it the societal prominence of complex, dynamically sensitive structures. The unique characteristics of these structures challenge a number of accepted analysis tools, ill-suited for fully capturing dynamic nonlinear or nonstationary features, and compel engineers to recast their perspectives and refine their understanding by moving into time-frequency domains and learning from full-scale observations. Within the context of such initiatives, researchers can begin to document the in-situ dynamic characteristics of structures, particularly damping levels, as they evolve with amplitude and come to a deeper understanding of the inherent levels of energy dissipation within real structures.

14.1 Contributions of This Work

This work explored a number of the issues confronted as time-frequency analysis techniques and advanced instrumentation systems are applied to Civil Engineering structures. The specific contributions of this work are summarized herein.

14.1.1 Wavelet Analysis Framework and Application to Civil Engineering Signals

The multi-resolution capability of Wavelet Transforms makes it a powerful tool for time-frequency analysis, optimally adjusting to the Heisenberg Uncertainty Principle at each analysis frequency. However, in order to provide meaningful results, the transform must be applied with a proper understanding of its time-frequency resolutions. As these issues are rarely discussed within the literature, in part due to the infancy of Wavelet Transforms, an analysis framework was presented in this work for the popular Morlet wavelet. In particular, this work unified and organized the theory of wavelets and assembled within a single framework the various properties and relations necessary for application to real Civil Engineering signals. This framework, detailed in Chapter 4, was predicated on the general theory of wavelets and the properties of the Gaussian window specifically associated with the Morlet wavelet. Three flexible tools were provided in the context of this discussion, each reiterating the importance of wavelet central frequency in achieving desired results: (1) a discretization of scales consistent with frame theory but with flexibility and accommodating the adaptive bandwidth of this parent wavelet; (2) a flexible criterion for selecting the central frequency of the wavelet to separate closely spaced modes; and (3) a rationalization of end effects in this parent wavelet and the introduction of a reflective padding scheme to mitigate its effects. The examples provided within Chapter 4 and throughout this work reiterate the significance of these framework elements in achieving satisfactory results, particularly within Chapter 8 in the context of a wavelet-based system identification procedure and in the rationalization of spurious coherence in the wavelet-based coherence measure in Chapter 6, which was effectively mitigated by three tiers of thresholding introduced by this work.

The framework was then applied in Chapter 5 to a number of signals of interest in Civil Engineering, tracking the evolution of frequency content in a number of noteworthy earthquake events, quantifying the rates of energy accumulation in time and frequency. The subsequent analysis of the measured response of a structure to the Northridge Earthquake further demonstrated the power of this technique for tracking the softening of frequency attributable to damage in the structure following strong shaking. These perspectives, including the wavelet instantaneous spectra, which provide snapshots of energy content at a given time, were then applied to unlock the mystery surrounding the lateral-torsional response of a tall building monitored in full-scale. The wavelet was crucial in facilitating the identification of beat phenomenon in the structure, leading to a coalescence between closely-spaced sway and torsional modes, as well as capturing a nonlinearity in frequency that surfaces as the result of large amplitude motion and facilitates beating between the structural modes. An extension of this framework to measured offshore platform response further highlights the wavelet's ability to capture time-varying characteristics in response and intermittent features of random waves. Many of these insights were not previously available without the use of Wavelet Transforms.

14.1.2 Wavelet Analogs to Hilbert Spectral Analysis

Although the work by Huang et al. (1998) brought a new tool to time-frequency analysis, its comparisons to wavelet transforms cast considerable doubt on the performance of the latter tool for analyzing nonlinear and nonstationary phenomenon. However, upon revisiting many of these examples, in light of the aforementioned processing framework and through the appropriate understanding of the importance of central frequency, both

can be shown to track supercyclic nonlinearities and nonstationary features in a comparable manner. This comparison between the two was facilitated through the introduction of a wavelet instantaneous frequency spectrum to clarify that there is no fundamental difference between the representation of the wavelet representation and the Hilbert Spectrum. These discussions in Chapter 7 further highlighted some deficiencies of Hilbert Spectral Analysis in two instances, one related to the inability to separate closely spaced modes for which the aforementioned wavelet framework proved advantageous. Perhaps the more significant finding was that the treatment of highly sensitive nonlinear systems varies between the two approaches, with the Hilbert Spectrum carrying both supercyclic and subcyclic nonlinearities while the wavelet's instantaneous frequency carries the former and the latter is captured by the wavelet instantaneous bandwidth.

14.1.3 Introduction of Full-Scale Monitoring and Advanced Instrumentation: Global Positioning Systems

This work also introduced a full-scale monitoring program in Chicago seeking to systematically validate the performance of tall buildings by comparing the observed response to the predictions from wind tunnel testing and analytic models developed in the design phase. In that regard, this program is one of the first of its kind, particularly in the United States. Chapter 9 discussed sensor selection, configuration and installation as part of this on-going monitoring program. In particular, Chapters 10-13 give a detailed discussion of the configuration and assembly of a comprehensive global positioning system and validation of this sensor for tracking the displacements of flexible structures

in full scale within urban environments. In particular, these calibration studies validated the performance of the system and identified the manner in which position quality thresholds could be constructed to provide a much needed reliability measure for the GPS position estimates. Dynamic testing revealed that quality tracking in terms of averaged measures like standard deviation can be achieved consistently when the GPS signal-to-noise ratio is 200% or more. Full-scale data demonstrate the utility of GPS monitoring for such investigations and the importance of the position quality thresholds in determining the reliability of the GPS tracking. In that regard, this work takes the first steps in practically addressing the issues associated with GPS monitoring in urban environments, including the identification and mitigation of multi-path effects.

14.1.4 Evaluation and Treatment of Uncertainty in Damping Estimation from Ambient Vibration Data

This work documented the uncertainty associated with common system identification approaches, contributing bootstrapping to provide a practical tool for assessing the uncertainty associated with an estimate of damping, allowing the construction of variance envelopes, confidence intervals and histograms for the estimated damping from a single measured time history. This work also documented the factors contributing to the performance of the Random Decrement Technique. Although other studies had considered the ramifications of violating the white noise assumption or the nonlinearity of the oscillator, none had systematically addressed other issues governing the performance of the technique. This research responded to this deficiency by investigating the influence of potential correlation between captured segments, the required number of

captured segments to generate a stable signature, the significance of the selected triggering condition, and the influence of nonstationarity, all important in light of the growing popularity of this system identification technique.

14.2 Future Directions

One obvious extension of this work lies in the analysis of the full-scale data being collected continuously through the monitoring program in Chapter 9 to fulfill the objectives of the original NSF proposal. This data will also provide a venue in which to explore the in-situ damping levels and their amplitude dependence. These comprise immediate area of future work based on this dissertation. In a more general sense, this work overviews many of the emerging technologies in sensing, system identification and data analysis that are the cornerstones of advanced health monitoring — an initiative that is growing in potential within the United States. However, the very nature of this work also provides the opportunity to extend many of the frameworks, particularly with regard to wavelets, for the analysis of other signals relevant to Civil Engineering and beyond. Some of the future work in these areas is articulated below.

14.2.1 Extension of Framework to Other Wavelets

In general, most parent wavelets do not have a 1:1 inverse relation between scale and Fourier frequency and do not provide a direct relation Fourier frequency and scale, unlike the Morlet wavelet used in this work. Still, such relations can still be approximately generated through a procedure discussed in Meyers et al. (1993). An equivalent Fourier frequency relationship with scale can be derived analytically for a given parent wavelet

by calculating the wavelet transform of a cosine wave of known frequency, when the desired parent wavelet is invoked. By utilizing the simplified calculations in the frequency domain, similar to those shown in Chapter 4 when discussing a wavelet half-power bandwidth measure, the scale at which the power spectrum reaches its maximum can be determined. These calculations were conducted in Torrence & Compo (1998) to validate this technique for the Morlet wavelet. They found that the Fourier frequency was inversely proportional to 1.03 times the scale when a $f_o = 0.955$ Hz Morlet wavelet was used. Considering that the exact relation between scale and frequency for the Morlet wavelet is $f = f_o/a$, this analytic relationship provides a good approximation and is deemed adequate to identify a scale-frequency relationships for other wavelets. Armed with such an approach, this wavelet framework can be readily extended and adapted for other classes of wavelets, whose characteristics embody particular features being sought within measured data, e.g. discontinuities or other indicators of damage within a body. This also opens the spectrum of analysis to many of the discrete forms of the transform, which often have attractive features in terms of reconstruction and compact support, but lack direct relations to traditional Fourier frequencies.

14.2.2 Enhancing Ridge Extraction Abilities

The comparison of wavelets to Hilbert Spectra invoked the use of ridge extraction techniques to clearly isolate the instantaneous frequency with time and allow the wavelet skeleton to be identified. Ridge extraction can be very challenging in the presence of noise, leading to a number of approaches (Carmona et al., 1998). The wavelet scalogram can provide the opportunity to overcome many of these issues, even more so, if the

scalograms can be refined to remove some of these lingering noise features prior to ridge extraction, allowing the ridges to be more readily identified and isolated. One possibility is the use of scalogram reassignment for Morlet wavelets, as discussed in Peng et al. (2002) to refine the scalogram in this regard.

14.2.3 Window Separation

As shown throughout this work, the window effects due to wavelets modify the bandwidth of wavelet instantaneous frequency spectra. In future work, a strategy for separation of the window effects inherent to the parent wavelet will be developed. While the exploration of other parent wavelets may inherently reduce these window effects and can be explored as alternative spectral representations, in the context of Morlet wavelets that have attractive analogs to Fourier spectra, these window effects may still be quantified theoretically, through an extension of the work by Cohen (1999) and verified by simulation. The relations identified in Perrier et al. (1995) may also be helpful in this regard. In doing so, more meaningful instantaneous estimates of damping can be obtained from the instantaneous bandwidth measures introduced in Chapter 4, providing valuable insights into the variation of damping with amplitude. However, it may also be prudent to develop additional frameworks for estimation of instantaneous spectral bandwidth. One possibility in this regard is to relate the rate of change of wavelet coefficients over the range of scales on either side of the wavelet ridge. This will be explored in the future work based on this research.

14.2.4 Enhancement of GPS Sensing Technologies

The limited full-scale data harvested thus far using GPS has highlighted its utility in such monitoring programs. However, it has also reiterated the potential issues of multi-path effects embedded in the quasi-static components of GPS displacements. In order to enhance the ability to distinguish these error sources, taking advantage of the repeatability of GPS, future efforts will collect data at nights under mild wind conditions over an extended time period so that every potential GPS configuration can be observed in conditions free from considerable thermal and wind effects. Each of these satellite orientations will eventually cross into the nighttime monitoring period since the same satellite configurations orbit 4 minutes earlier each day. These will be averaged to define a baseline multi-path threshold for a complete 24-hour monitoring window. This reference pattern can be used to identify the probable multi-path trends, using the superior filtering abilities of wavelets to separate this reference pattern from future full-scale displacement data (Chen et al., 2001). This will be developed along with the approaches mentioned in Chapter 14 to repair future harvested displacement data contaminated by multi-path.

Concurrently, a permanent baseline for Building 1 is being established. Recall that a preliminary baseline was used to define differential displacements of Building 1 using the GPS position measures. A more precise baseline position can be determined by using the same data collected in the above procedure, since thermal expansion and wind-induced motion should not be present. This data will be more stringently filtered, keeping only the highest precision data for which ambiguities are minimal. The positions of

several months of such monitoring will then be averaged to minimize any residual multi-path effect to produce a permanent baseline position of the undeformed building within the local north and east coordinates.

APPENDIX

OVERVIEW OF RESAMPLING THEORY: THE BOOTSTRAP

A.1 Motivation

If the distribution of a random variable is known with certainty, then theory or simulation may be invoked to calculate various statistics. However, in most practical applications, this is not possible, but the bootstrap may be used to make the best of what information is available. The bootstrap approach is a computer-based method for assigning accuracy to statistical estimates based on independent data points or samples, which, in its simplest form, is non-parametric, requiring no assumptions about the distribution of the parameters (Politis, 1998). The approach is widely documented in the literature and has a variety of practical applications elaborated in textbooks (Efron & Tibshirani, 1993; Hjorth, 1994). Even in cases where the statistic is too complicated for theoretical estimates of random errors, the bootstrap can be invoked to make some inference.

When enough samples are drawn randomly from an arbitrary distribution, the Central Limit Theorem (CLT) can be invoked to assert that the estimator is approximately normally distributed. Luckily, the underlying assumptions of bootstrap analysis are valid in cases where only limited samples are drawn, say 10 or 15 samples, though as more and more samples are drawn, the bootstrap and CLT will yield

increasingly equivalent representations. The bootstrap is also capable of capturing non-Gaussian statistics such as skewness that could not be captured relying on CLT (Efron & Tibshirani, 1993).

A.2 Bootstrap Theory

This process of statistical inference involves estimating some statistic $\hat{\theta} = s(x)$ of an unknown Probability Density Function (PDF) F of a population based on an observed random sample $x = [x_1, x_2, \dots, x_n]$ drawn from it. Let the sampled data compose a population with empirical distribution function \hat{F} . By randomly sampling with replacement from the observed values, a new sample or bootstrap sample $x^* = [x_1^*, x_2^*, \dots, x_n^*]$ can be generated which is not the actual data but a randomized or resampled version of it. The resampled data can then be used to estimate the statistic of interest $\hat{\theta}^* = s(x^*)$ to produce a bootstrap replication. The rationale for this methodology is based on simple analogies depicted in Figure A.1. F gives x by random sampling, so \hat{F} gives x^* by random sampling; $\hat{\theta}$ is obtained from x via the function $s(x)$, so $\hat{\theta}^*$ is obtained from x^* in the same way (Efron & Tibshirani, 1993). As the resamples are generated as a function of the sample distribution, which is itself a randomized sample of the actual population, the distribution of the resamples varies randomly in the same way that the sample population does, paralleling Monte Carlo simulation, as discussed in (Efron & Tibshirani, 1993). Note that the function $s(x)$ can be virtually any statistic or parameter of the system. This resampling process is repeated B times to form B replications. Based on these B replications, the variance or standard error of the

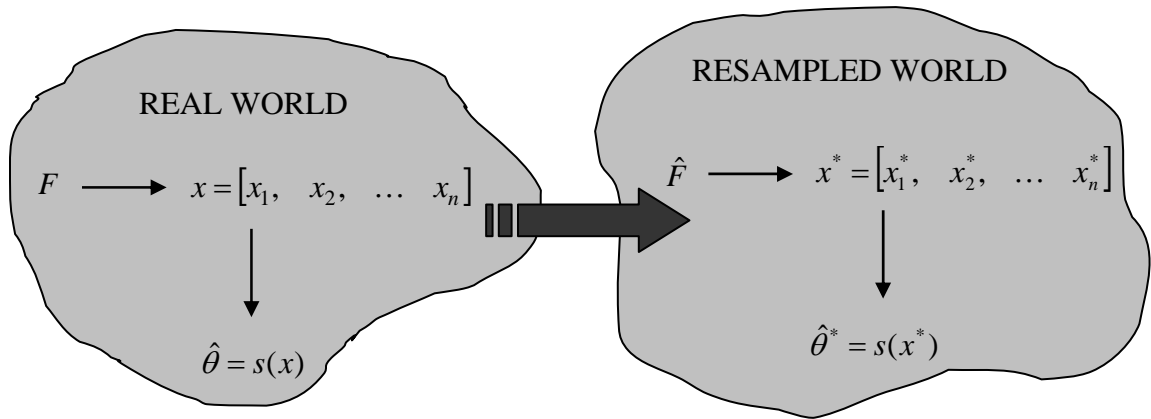


FIGURE A.1. Schematic diagram of generalized bootstrap concept (adapted from Efron & Tibshirani, 1993)

population can be determined. The resampling scheme proposed here merely mimics the randomness of the process itself, more closely approximating the process as more and more data is considered, i.e. as $\hat{F} \rightarrow F$.

A.3 Bootstrapping to Estimate Variance in RDS and PSD

For the present application, the measured response of a mechanical oscillator can be assumed to be one such random sample, as the driving process is randomly varying. By the nature of the random process driving the system, the estimated damping and frequency are not deterministic, but are also random due to the inherent variability in the PSD and RDS from which they are drawn. Therefore, the lengthy amounts of data analyzed can be segmented into assumed independent random samples -- the segmenting discussed previously to produce RDT segments satisfying a trigger or the segmenting in the generation of the PSD. Each segment, itself a random sample, can be subjected to the same bootstrapping methodology, as it is assumed to have been drawn randomly. It takes

a number of hours of measured response data to obtain a single, reasonable estimate of the system's damping by RDT or SA, yielding a large amount of data for which the empirical distribution of the sampled population is indeed approaching the true PDF.

As the generalities of bootstrapping have been discussed, the actual bootstrapping scheme for this application is proposed in Figure A.2. As implemented in Vandermeulen et al. (2000) and in Chapter 2 of this work, the N_s raw spectra and the N_r time-history segments that satisfy the RDT trigger condition form the sample population. From this population, N_s or N_r samples are drawn with replacement to form one bootstrap sample. Each bootstrap sample is then averaged to form a smooth PSD estimate or stable RDS and form a bootstrap replicate. This is repeated B times to form B replicates. These bootstrap replicates can be plotted atop one another to create variance envelopes, shown by the thick outline in Figure A.3, enveloping the plug-in estimates of the random decrement signature and power spectral density, i.e. those that would be obtained from the procedures in Section 2.2.1 and 2.2.2 without resampling. Significant deviations from the estimated PSD and RDS (shown in black) highlight the areas of highest variance. Each of these B replicates is then used to determine the system's dynamic properties and make statistical inferences on the reliability of the estimate via calculations of the standard errors of these values. The ideal estimate of the standard error of these replicate estimates is obtained by (Efron & Tibshirani, 1993)

$$\sigma_B = \left\{ \sum_{b=1}^B [\hat{\theta}^*(b) - \hat{\theta}^*(\cdot)]^2 / (B-1) \right\}^{1/2} \quad (\text{A.1})$$

where

$$\hat{\theta}^*(\cdot) = \sum_{b=1}^B \hat{\theta}^*(b) / B. \quad (\text{A.2})$$

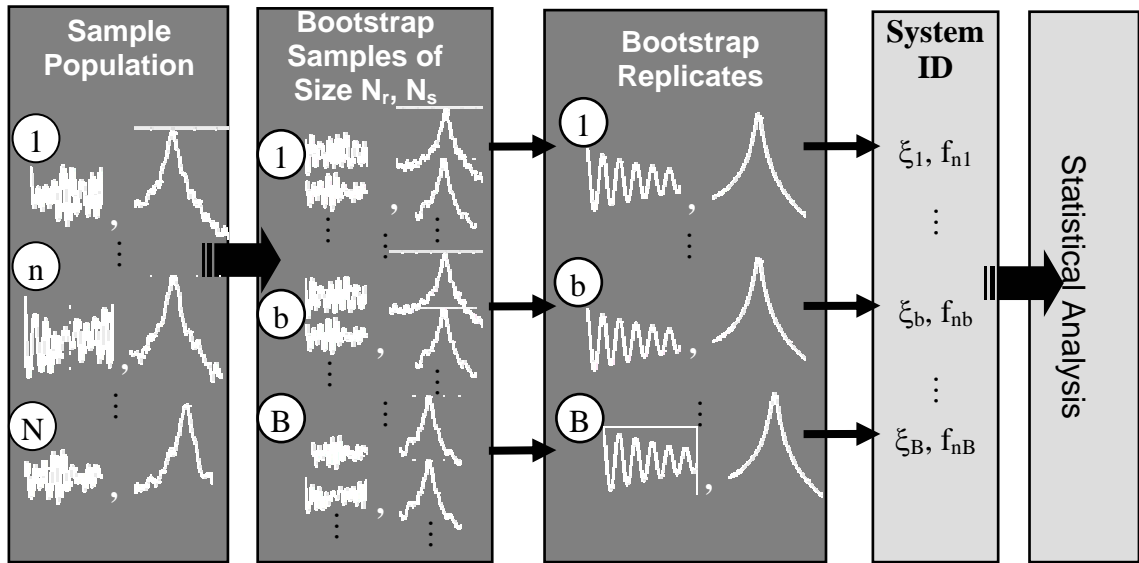


FIGURE A.2. Bootstrapping scheme for system identification

Equation A.2 can be viewed as the bootstrap mean, with the accuracy of Equation A.1 enhanced as $B \rightarrow \infty$. Discussions on the practical values of B are provided in (Efron & Tibshirani, 1993).

Understandably, for this approach to work, it must be assumed that the sample population, represented by the measured time history, is representative of the actual process. If the data is drawn from periods of extremes, it may not be indicative of typical behavior. So it is vital that the samples drawn are sufficient to make inferences about the total process behavior. This is a critical consideration. In cases where data are of poor quality, accurate estimates and information cannot be provided by any approach, even the bootstrap. The bootstrap cannot repair sampled data, but can merely make inferences about its various statistics. Even with this in mind, it is hoped that the introduction of

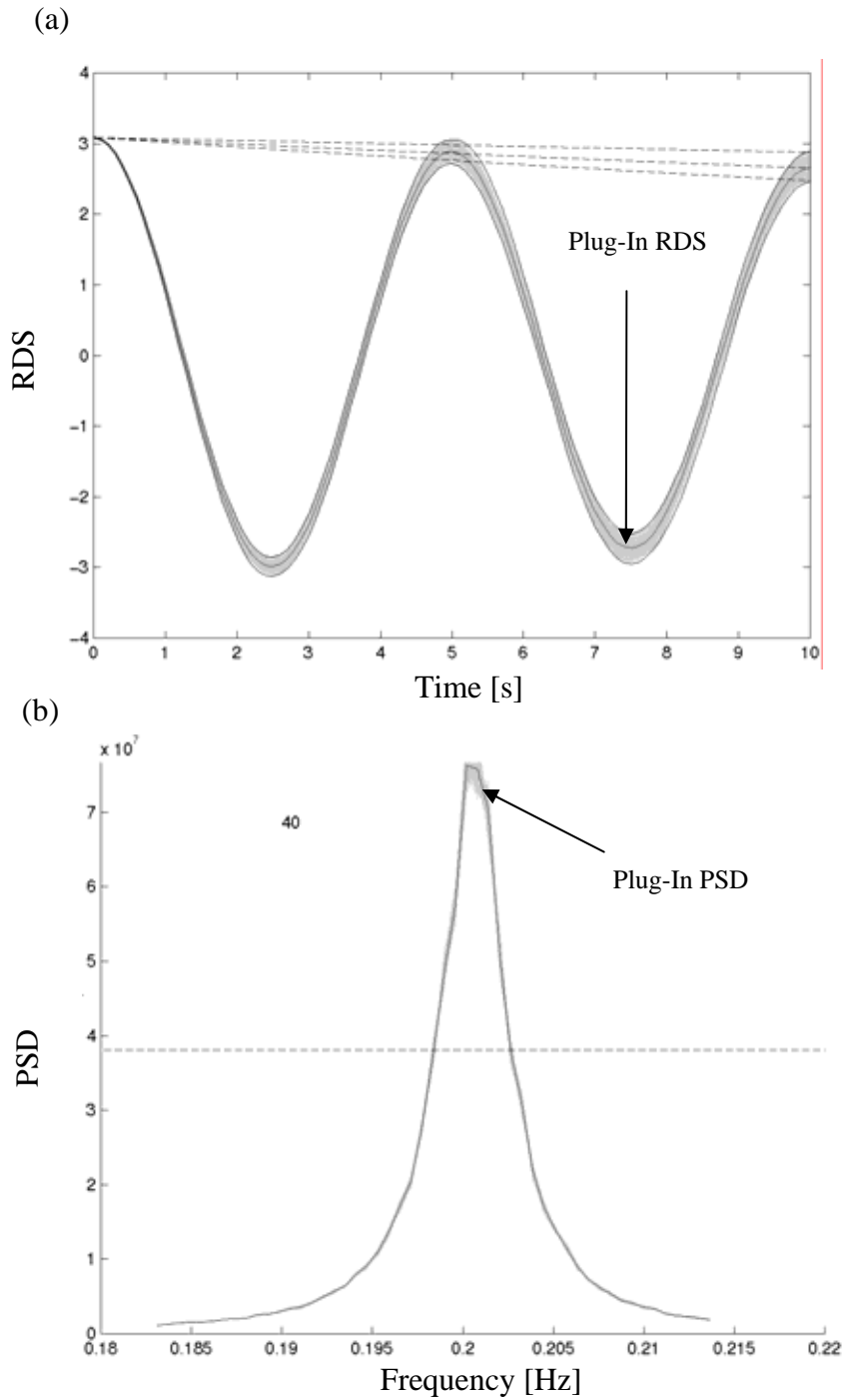


FIGURE A.3. Variance envelopes for (a) RDT and (b) PSD. Grey lines indicate variance envelope; black line indicates traditional RDT and PSD estimate; dotted lines indicate RDS decay and HPBW

such a scheme will provide researchers with a simple means by which to estimate the variance of the frequency and damping estimated from power spectra and random decrement signatures, which currently lack such reliability measures. Before doing so, it should be noted that this concept has also been applied for identification of confidence intervals for instantaneous frequency estimates, which also previously lacked the interval estimates (Zoubir et al., 1994).

WORKS CITED

- Abdelrazaq, A., Baker, W., Isyumov, N., Kareem, A., Kijewski, T. and R. Sinn (2000) "Studies to Correlate Actual and Expected Behavior of Tall Buildings Under Wind Action," In *Proceedings of Structures Congress 2000*, Philadelphia, May 8-10.
- Ashkenazi, V. and G.W. Roberts (1997) "Experimental Monitoring of the Humber Bridge Using GPS," *Civil Engineering*, Proceedings. Institution of Civil Engineers, **120**(11): 177-182.
- Axelrad, P., Comp, C.J. and P.E. Macdorran (1996) "SNR-Based Multipath Error Correction for GPS Differential Phase," *IEEE Transactions on Aerospace and Electronic Systems*, **32**(2): 650-659.
- Ballard, C.M. and S.S. Chen (1997) "An Internet Structural Monitoring System," *Intelligent Civil Engineering Materials and Structures*, ASCE: 229-242.
- Barnes, A.E. (1993) "Instantaneous Spectral Bandwidth and Dominant Frequency with Applications to Seismic Reflection Data," *Geophysics*, **58**(3): 419-428.
- Basu, B. and V.K. Gupta (1997) "Non-Stationary Seismic Response of MDOF Systems by Wavelet Transform," *Earthquake Engineering and Structural Dynamics*, **26**: 1243-1258.
- Basu, B. and V.K. Gupta (2000) "Stochastic Seismic Response of Single-Degree-of-Freedom Systems Through Wavelets," *Engineering Structures*, **22**: 1714-1722.
- Behr, J.A., Hudnut, K.W. and N.E. King (1998) "Monitoring Structural Deformation at Pacoima Dam, California Using Continuous GPS," In *ION GPS-98: Proceedings of the 11th International Technical Meeting of the Satellite Division of the Institute of Navigation*, Nashville, September 15-18: 59-68.
- Bendat, J. (1993) *Engineering Applications of Correlation and Spectral Analysis*. Wiley & Sons, New York.
- Bendat, J.S. and A.G. Piersol (1986) *Random Data: Analysis and Measurement Procedures*. 2nd Edition, Wiley & Sons, New York.
- Benuska, L., Ed. (1990) *Loma Prieta Earthquake Reconnaissance Report*. Supplement to *Earthquake Spectra*, EERI, **6**.

- Boashash, B. (1992a) "Estimating and Interpreting the Instantaneous Frequency of a Signal – Part 1: Fundamentals," *Proceedings of IEEE*, **80**(4): 520-538.
- Boashash, B. (1992b) "Estimating and Interpreting the Instantaneous Frequency of a Signal – Part 2: Algorithms and Applications," *Proceedings of IEEE*, **80**(4): 540-568.
- Breukelman, B., Dalgleish, A. and N. Isyumov (1993) "Estimates of Damping and Stiffness for Tall Buildings," In *Proceedings of the 7th U.S. National Conference on Wind Engineering*, Los Angeles, June.
- Brown, D. (2003) *Analysis of Wind Induced Acceleration and Pressure Data from an Eight Hundred Foot Tower*. Thesis, Department of Civil Engineering and Geological Sciences, University of Notre Dame, Notre Dame, IN.
- Butsch, F. (2002) "A Growing Concern: Radio Frequency Interference and GPS," *GPS World*, **13**(10): 40-50.
- Cao, H., Ellis, B.R. and J.D. Littler (1997) "The Use of Maximum Entropy Method for the Spectral Analysis of Wind-Induced Data Recorded on Buildings," *Journal of Wind Engineering and Industrial Aerodynamics*, **72**: 81-93.
- Carmona, R.A., Hwang, W.L. and B. Torresani (1997) "Characterization of Signals by the Ridges of Their Wavelet Transforms," *IEEE Transactions on Signal Processing*, **45**(10): 2586-2590.
- Carmona, R., Hwang, W.L. and B. Torresani (1998) *Practical Time-Frequency Analysis*. Academic Press, San Diego.
- Celebi, M. and E. Safak (1991) "Recorded Seismic Response of Transamerica Building. Part I: Data and Preliminary Analysis," *Journal of Structural Engineering*, ASCE.
- Celebi, M., Prescott, W., Stein, R., Hudnut, K., Behr, J. and S. Wilson (1999) "GPS Monitoring of Dynamic Behavior of Long-Period Structures," *Earthquake Spectra*, **15**(1): 55-66.
- Celebi, M. (2000) "GPS in Dynamic Monitoring of Long-Period Structures," *Soil Dynamics and Earthquake Engineering*, **20**: 477-483.
- Celebi, M. and A. Sanli (2002) "GPS in Pioneering Dynamic Monitoring of Long-Period Structures," *Earthquake Spectra*, **18**(1): 47-61.
- Chen, Y., Huang, D., Ding, X., Xu, Y. and J.M. Ko (2001) "Measurement of Vibrations of Tall Buildings: A Case Study," In *Proceedings of SPIE Conference on Non-Destructive Evaluation*, Newport Beach, CA, March: CD-ROM.
- Chui, C.K. (1992) *An Introduction to Wavelets*. Academic Press, San Diego.
- Clough, R. and J. Penzien (1993) *Dynamics of Structures*. McGraw-Hill, New York.

- Coca, D. and S.A. Billings (1997) "Continuous-Time System Identification for Linear and Nonlinear Systems Using Wavelet Decompositions," *International Journal of Bifurcation and Chaos*, 7(1): 87-96.
- Cohen, L. (1999) "Wavelet Moments and Time-Frequency Analysis," *Proceedings of SPIE*, **3807**: 434-445.
- Cohen, L. and C. Lee (1989) "Instantaneous Frequency and Time-Frequency Distributions," In *IEEE International Symposium on Circuits and Systems*, **2**: 1231-1234.
- Cohen, L. and C. Lee (1990) "Instantaneous Bandwidth for Signals and Spectrogram," In *ICASSP: IEEE International Conference on Acoustics, Speech and Signal Processing*, **5**, April 3-6: 2451-2454.
- Cole, H.A. (1973) *On-Line Failure Detection and Damping Measurement of Aerospace Structures by Random Decrement Signatures*. NASA CR-2205.
- Corbin, M., Hera, A. and Z. Hou (2000) "Locating Damage Regions using Wavelet Approach," In *Proceedings of 14th ASCE Engineering Mechanics Conference*, Austin, May 21-24: CD-ROM.
- Council on Tall Buildings in Urban Habitat (CTBUH) (1993) *Structural Systems for Tall Buildings*. McGraw-Hill, New York.
- Counselman, C.C. (1999) "Multipath-Rejecting GPS Antennas," *Proceedings of the IEEE*, **87**(1): 86-91.
- Daubechies, I. (1990), "Orthonormal Bases of Compactly Supported Wavelets II. Variations on a Theme," *SIAM J. of Mathematical Analysis*.
- Davenport, A.G. and Hill-Carroll (1986) "Damping in Tall Buildings: Its Variability and Treatment in Design," In *ASCE Spring Convention*, Seattle: 42-57.
- Davis, D.A. (2003) "Galileo Stuck in Political Traffic," *GPS World*, **14**(2): 10-12.
- Delprat, N., Escudie, B., Guillemain, P., Kronland-Martinet, R., Tchamitchian, P. and B. Torresani (1992) "Asymptotic Wavelet and Gabor Analysis: Extraction of Instantaneous Frequencies," *IEEE Transactions on Information Theory*, **38**(2): 644-664.
- Delaunay, D., Grillaud, G., Bietry, J. and C. Sacre (1999) "In-Situ Validations of Wind Design Studies for Long-Span Bridges," In *Proceedings of the 10th International Conference on Wind Engineering*, Copenhagen, June, **2**: 863-869.
- Desforges, M.J., Cooper, J.E., and J.R. Wright (1995) "Spectral and Modal Parameter Estimation from Output-Only Measurements," *Mechanical Systems and Signal Processing*, **9**(2): 169-186.

- Duffing, G. (1918) *Erzwungene Schwingungen Bei Veränderlicher Eigenfrequenz*. 1st Edn., Braunschweig: F. Vieweg u. Sohn (in German).
- Dunyak, J., Gilliam, X., Peterson, R. and D. Smith (1997) "Coherent Gust Detection by Wavelet Transform," In *Proceedings of 8th U.S. National Conference on Wind Engineering (8USCWE)*, Johns Hopkins University, Baltimore, June: CD-ROM.
- Durgin, F.H. and T. Gilbert (1994) *Data From a Full Scale Study of an 800 Foot Building in Boston*. Wright Brothers Facility, Department of Aeronautics and Astronautics, Massachusetts Institute of Technology, Internal Report WBWT-TR-1250.
- Durgin, F.H., Gilbert, T.J., and J.R. Macachor (1990) "Available Full-Scale On-Site Wind-Induced Data from a Major Tall Building," *Journal of Wind Engineering and Industrial Aerodynamics*, **36**: 1201-1215.
- Durgin, F.H. and R.J. Hansen (1987) "Full-Scale On-Site Wind-Induced Data from a Tall Building," In *ASCE Dynamics of Structures, Proceedings of Sessions at Structures Congress '87*, Orlando, FL.
- Efron, B. and R.J. Tibshirani (1993) *An Introduction to the Bootstrap*. Chapman & Hall, New York.
- Ellis, B.R. (1996) "Full-Scale Measurements of the Dynamic Characteristics of Buildings in the UK," *Journal of Wind Engineering and Industrial Aerodynamics*, **59**: 365-382.
- Ellis, B.R. (1998) "Damping and Non-Linear Behavior in Buildings," In *Proceedings of Structural Engineers World Congress*, San Francisco, July 19-23: CD-ROM T193-5.
- Enge, P. and P. Misra (1999) "Scanning the Issue/Technology: Special Issue on Global Positioning System," *Proceedings of the IEEE*, **87**(1): 3-15.
- Engineering Sciences Data Units (ESDU) (1983) *Damping of Structures, Part I: Tall Buildings*. ESDU, Item No. 83009, London.
- Evans, R.A. and B.E. Lee (1981) "The Assessment of Dynamic Wind Loads on a Tall Building: A Comparison of Model and Full Scale Results," In *Proceedings of 4th US National Conference on Wind Engineering Research*, University of Washington, Seattle, July.
- Fairweather, V. (1996) "Measuring Bridge Movement," *Civil Engineering*, **66**(6): 48.
- Farge, M. (1992) "Wavelet Transforms and Their Applications to Turbulence," *Annual Reviews of Fluid Mechanics*, **24**: 395-457.
- Feldman, M. (1994a) "Non-Linear System Vibration Analysis Using Hilbert Transform – I. Free Vibration Analysis Method 'Freevib'," *Mechanical Systems and Signal Processing*, **8**(2): 119-127.

- Feldman, M. (1994b) "Linear System Vibration Analysis Using Hilbert Transform – II. Forced Vibration Analysis Method 'Forcevib'," *Mechanical Systems and Signal Processing*, **8**(3): 309-318.
- Feldman, M. and S. Braun (1995) "Identification of Non-Linear System Parameters via the Instantaneous Frequency: Application of the Hilbert Transform and Wigner-Ville Techniques," In *Proceedings of 13th International Modal Analysis Conference*: 637-642.
- Fukuwa, N., Nishizaka, R., Yagi, S., Tanaka, K., and Y. Tamura (1996) "Field Measurements of Damping and Natural Frequency of an Actual, Steel-Framed Building over a Wide Range of Amplitudes," *Journal of Wind Engineering and Industrial Aerodynamics*, **59**: 325-347.
- Gabor, D. (1946) "Theory of Communication," *Proceedings of IEEE*, **93**(III): 429-457.
- Ghanem, R. and M. Shinozuka (1995), "Structural-System Identification I: Theory," *Journal of Engineering Mechanics*, **121**(2): 255-264.
- Ghanem, R. and F. Romeo (2000) "A Wavelet-Based Approach for the Identification of Time-Varying Dynamical Systems," *Journal of Sound and Vibration*, **234**(4): 555-576.
- Grossman, A. and J. Morlet (1984) "Decomposition of Hardy Functions into Square Integrable Wavelets of Constant Shape," *SIAM Journal of Mathematical Analysis*, **15**(4): 723-736.
- Gurley, K. (1993) *Global Response Analysis of A Tension Leg Platform: Validation of Theory with Experimental Data*. Thesis, University of Notre Dame, Notre Dame, IN.
- Gurley, K. and A. Kareem (1996) "Damping in Structures: Its Evaluation and Treatment of Uncertainty," *Journal of Wind Engineering and Industrial Aerodynamics*, **59**(2,3): 131-157.
- Gurley, K. and A. Kareem (1997a) "Analysis, Interpretation, Modeling and Simulation of Unsteady Wind and Pressure Data," *Journal of Wind Engineering and Industrial Aerodynamics*, **69-71**: 657-669.
- Gurley, K. and A. Kareem (1997b) "Modeling PDFs of Non-Gaussian System Response," In *7th International Conference on Structural Safety and Reliability (ICOSSAR)*, Kyoto, Japan, November.
- Gurley, K., Tognarelli, M. and A. Kareem (1997) "Analysis and Simulation Tools for Wind Engineering," *Probabilistic Engineering Mechanics*, **12**(1): 9-31.
- Gurley, K. and A. Kareem (1999) "Application of Wavelet Transforms in Earthquake, Wind, and Ocean Engineering," *Engineering Structures*, **21**: 149-167.

- Gurley, K., Kijewski, T. and A. Kareem (2003) "Higher-Order Correlation Detection in Nonlinear Aerodynamic Systems Using Wavelet Transforms," *Journal of Engineering Mechanics*, ASCE, **129**(2): 188-201.
- Guo, J. and S. Ge (1997) "Research of Displacement and Frequency of Tall Building under Wind Load Using GPS," *Proceedings of ION GPS*, **10**(2): 1385-1388.
- Hangan, H., Kopp, G.A., Vernet, A. and R. Martinuzzi (2001) "A Wavelet Pattern Recognition Technique for Identifying Flow Structures in Cylinder Generated Wakes," *Journal of Wind Engineering and Industrial Aerodynamics*, **89**: 1001-1015.
- Hans, S., Ibraim, E., Pernot, S., Boutin, C. and C.-H. Lamarque (2000) "Damping Identification in Multi-Degree-of-Freedom Systems via a Wavelet-Logarithmic Decrement – Part 2: Study of a Civil Engineering Building," *Journal of Sound and Vibration*, **235**(3): 375-403.
- Hansen, R.J., Vanmarcke, E.H., and J.W. Reed (1979) "Human Response to Wind-Induced Motion of Buildings," *Engineering Journal of American Institute of Steel Construction*, **16**(3): 66-74.
- Hart, G.C. and R. Vasudevan (1975) "Earthquake Design of Buildings: Damping," *Journal of Structures Division*, ASCE, **101**(ST1): 49-65.
- Hartin, J.R. (2001) "Application of a Wavelet Based FRF to the Analysis of a Bilinear Structure," In *Proceedings of International Modal Analysis Conference*, SEM, Orlando, FL, February 5-8: 1414-1419.
- Haviland, R. (1976) *A Study of the Uncertainties in the Fundamental Translational Period and Damping Values for Real Buildings*. Research Report No. 5, Pub. No. R76-12, Dept. of Civil Engineering, MIT, Cambridge, MA.
- Hjorth, J.S. (1994) *Computer Intensive Statistical Methods*. Chapman & Hall, New York.
- Huang, S.Y., Qi, G.Z. and J.C.S. Yang (1994) "Wavelet for System Identification," In *Proceedings of International Modal Analysis Conference*, Honolulu: 1162-1166.
- Huang, J., Higuchi, K. and A. Shabbar (1998) "The Relationship Between the North Atlantic Oscillation and El Nino-Southern Oscillation," *Geophysical Research Letters*, **25**(14): 2701-2710.
- Huang, N.E., Shen, Z., Long, S.R., Wu, M.C., Shih, H.H., Zheng, Q., Yen, N.-C., Tung, C.C. and H.H. Lu (1998) "The Empirical Mode Decomposition and the Hilbert Spectrum for Nonlinear and Non-stationary Time Series Analysis," *Proceedings of Royal Society of London*, **454**: 903-995.
- Huang, N.E., Shen, Z. and S.R. Long (1999) "A New View of Nonlinear Water Waves: the Hilbert Spectrum," *Annual Review of Fluid Mechanics*, **31**: 417-457.

- Hudgins, L., Friehe, C.A., and M.E. Mayer (1993) "Wavelet Transforms and Atmospheric Turbulence," *Physical Review Letters*, The American Physical Society, **71**(20): 3279-3282.
- Hudnut, K.W. and J. Behr (1998) "Continuous GPS Monitoring of Structural Deformation at Pacoima Dam, California," *Seismological Research Letters*, **69**(4): 299-308.
- Hudson, D.E. (1977), "Dynamic Tests of Full-Scale Structures," *Journal of Engineering Mechanics Division*, ASCE, **103**(EM6): 1141-1157.
- Hyzak, M., Leach, M. and K. Duff (1997) "Practical Application of GPS to Bridge Deformation Monitoring," In *New Thrusts for Surveyors, Proceedings of 64th FIG Permanent Committee Meeting and International Symposium*, Singapore, May 11-16.
- Ibrahim, S.R. (1977) "Random Decrement Technique for Modal Identification of Structures," *Journal of Spacecraft*, **14**(11): 696-700.
- Ibrahim, S.R. (2001) "Efficient Random Decrement Computation for Identification of Ambient Responses," In *Proceedings International Modal Analysis Conference*, SEM, Orlando, FL, Feb 5-8: CD-ROM.
- Inaba, S., Suzuki, T. and M. Kageyama, (1998) "Active Vibration Control System Installed in a High-Rise Building," In *Proceedings of Structural Engineering World Congress*, San Francisco, July 19-23: CD-ROM T198-1.
- Isyumov, N., Davenport, A.G., and J. Montbaliu (1984) "CN Tower, Toronto: Model and Full-Scale Response to Wind," In *Proceedings of International Association for Bridge and Structural Engineering (IABSE) 12th Congress*, Vancouver, September 30.
- Isyumov, N., and D.P. Morrish (1997) "Full-scale Measurements to Assure Performance and Quality of Buildings and Structures," In *Proceedings of ASCE Structures Congress '97*, Portland, OR, April 14-16.
- Jeary, A.P. and B.R. Ellis (1981) "Vibration Tests on Structures at Varied Amplitudes," In *Proceedings of ASCE/EMD Conference on Dynamic Structures*, Atlanta.
- Jeary, A.P. (1986) "Damping in Tall Buildings – A Mechanism and a Predictor," *Earthquake Engineering and Structural Dynamics*, **14**: 733-750.
- Jeary, A.P. (1992) "Establishing Non-Linear Damping Characteristics of Structures from Non-Stationary Response Time Histories," *The Structural Engineer*, **70**(4): 61-66.
- Jeary, A.P. (1996) "The Description and Measurement of Nonlinear Damping in Structures," *Journal of Wind Engineering and Industrial Aerodynamics*, **59**: 103-114.
- Jennings, P.C., Kanamori, H., Helmberger, D., Clayton, R., Singh, S., Mena, E. and L. Astiz (1989) "Estimation of Future Strong Ground Motions in Mexico City," In Bertero,

- V.V., Ed., *Lessons Learned from the Mexico City Earthquake*, EERI, El Cerrito, CA: 15-17.
- Jennings, P.C. and F.J. Sanchez-Sesma (1989) "Working Group Conclusions on Strong Ground Motion," In V.V. Bertero, V.V., Ed., *Lessons Learned from the Mexico City Earthquake*, EERI, El Cerrito, CA: 2-3.
- Jones, G. and B. Boashash (1990) "Instantaneous Frequency, Instantaneous Bandwidth and the Analysis of Multicomponent Signals," In *Proceedings of IEEE Conference on Acoustics, Speech, and Signal Processing*, April 3-6, **5**: 2467-2470.
- Jones, N.P. and C.A. Spartz (1990) "Structural Damping Estimates for Long-Span Bridges," *Journal of Engineering Mechanics*, **116**(11): 2414-2433.
- Kanda, J., and T. Ohkuma (1990) "Recent Developments in Full-Scale Wind Pressure Measurements in Japan," *Journal of Wind Engineering and Industrial Aerodynamics*, **33**: 243-252.
- Kareem, A. (1985) "Wind-Induced Response Analysis of Tension Leg Platforms," *Journal of Structural Engineering*, **111**(1): 37-55.
- Kareem, A. (1987) "Dynamic Response of Structures Under Stochastic Environmental Loads," *Journal of Structural Engineering*, **14**(1): 1-8.
- Kareem, A. (1992) "Serviceability Issues and Motion Control of Tall Buildings," *Proceedings of Structures Congress*, ASCE, San Antonio.
- Kareem, A. and K. Gurley (1996) "Damping in Structures: Its Evaluation and Treatment of Uncertainty," *Journal of Wind Engineering and Industrial Aerodynamics*, **59**(2,3): 131-157.
- Kareem, A., Tognarelli, M.A., Gurley, K.R., and T.L. Kijewski (1998) "Modeling of Nonlinear Ocean Systems," In Shlesinger, M.F. and T. Swean, Eds., *Stochastically Excited Nonlinear Ocean Structures*. World Scientific, River Edge, NJ: 79-104.
- Kareem, A., Kijewski, T., and Y. Tamura (1999) "Mitigation of Motion of Tall Buildings with Recent Applications," *Wind and Structures*, **2**(3): 201-251.
- Kashima, S., Okano, S., Takeguchi, M. and K. Mori (2000) "Monitoring System for the Akashi Kaikyo Bridge," In *Workshop on Research and Monitoring of Long Span Bridges*, Hong Kong, April.
- Katafygiotis, L.S. and K.-V. Yuen (2001) "Bayesian Spectral Density Approach for Modal Updating Using Ambient Data," *Earthquake Engineering and Structural Dynamics*, **30**: 1103-1123.
- Kijewski, T. and A. Kareem (1998) "Comparative Study of Provisions in Codes and Standards with Wind Tunnel Data," *Wind and Structures*, **1**(1): 77-109.

- Kijewski, T. and A. Kareem (1999) "Analysis of Full-Scale Data from a Tall Building in Boston: Damping Estimates," In *Proceedings of 10 International Conference on Wind Engineering*, Copenhagen, June.
- Kijewski, T. and A. Kareem (2000) *Estimation and Modeling of Damping and Engineering Auxiliary Damping Systems in Civil Engineering Structures: An Overview*. NatHaz Modeling Lab Report to ASCE Committee on Wind Effects, University of Notre Dame, Notre Dame, IN.
- Kijewski, T., Haan, F. and A. Kareem (2001) "Wind Induced Vibrations," In Braun, S.G., Ewins, D.J. and S.S. Rao, Eds., *Encyclopedia of Vibration*, Academic Press: 1578-1587.
- Kijewski, T., Kwon, D.K. and A. Kareem (2003a) "E-Technologies for Wind Effects on Structures," In *Proceedings of 11th International Conference on Wind Engineering*, Lubbock, TX, June 2-5.
- Kijewski, T., Kilpatrick, J., Williams, T., Kwon, D.K., Young, B., Abdelrazaq, A., Galsworthy, J., Morrish, D., Isyumov, N. and A. Kareem (2003b) "Full-Scale Validation of the Wind-Induced Response of Tall Buildings: Preliminary Results of Chicago Monitoring Project," In *Proceedings of 2003 Structures Congress*, ASCE, Seattle, May 29-June 1.
- Kitamura, H., Ohkuma, T., Kanda, J., Mataka, Y., and S. Kawabata (1988) "Chiba Port Tower: Full-Scale Measurement of Wind Actions (Pt. I) Organization, Measurement System, and Strong Wind Data," *Journal of Wind Engineering and Industrial Aerodynamics*, **36**: 401-410.
- Koike, Y., Tanida, K., Mutaguchi, M., Murata, T., Imazeki, M., Yamada, T., Kurokawa, Y., Ohrui, S. and Y. Suzuki (1998) "Application of V-Shaped Hybrid Mass Damper to High-Rise Buildings and Verification of Damper Performance," In *Proceedings of Structural Engineering World Congress*, San Francisco, July 19-23: CD-ROM T198-4.
- Kyprianou, A. and W.J. Staszewski (1999) "On the Cross Wavelet Analysis of Duffing Oscillator," *Journal of Sound and Vibration*, **228**(1): 199-210.
- Lagomarsino, S. (1993) "Forecast Models for Damping and Vibration Periods of Buildings," *Journal of Wind Engineering and Industrial Aerodynamics*, **48**: 221-239.
- Lagomarsino, S. and L.C. Pagnini (1995) *Criteria for Modeling and Predicting Dynamic Parameters of Buildings*. Istituto di Scienza Delle Costruzioni, Universita di Genova – Facolta di Ingegneria, Pubblicazione Serie II n. 1.
- Lamarque, C.-H., Pernot, S. and A. Cuet (2000) "Damping Identification in Multi-Degree-of-Freedom Systems via a Wavelet-Logarithmic Decrement – Part 1: Theory," *Journal of Sound and Vibration*, **235**(3): 361-374.

- Lee, J.K. and Y.S. Park (1994) "The Complex Envelope Signal and An Application to Structural Modal Parameter Estimation," *Mechanical Systems and Signal Processing*, **8**(2): 129-144.
- Leica (1999) *Introduction to GPS (Global Positioning System) v. 1.0*. Leica Geosystems, Heerbrugg, Switzerland.
- Leica (2000) *Getting Started with SKI-Pro: User Manual v. 2.0*. Leica Geosystems, Heerbrugg, Switzerland.
- Lewalle, J. (1998) "Applications of Continuous Wavelets to Data Analysis, Part I: Wavelets Without Lemmas," In Von Karman Institute for Fluid Dynamics, Lecture Series 1998-06, *Advanced Measurement Techniques*, April 6-9.
- Li, Y. and A. Kareem (1993a) "Simulation of Multi-Variate Random Processes: Hybrid DFT and Digital Filtering Approach," *Journal of Engineering Mechanics*, ASCE: **119**(5): 1078-1098.
- Li, Y. and A. Kareem (1993b) "Parametric Modeling of Stochastic Wave Effects on Offshore Platforms," *Applied Ocean Research*, **15**(2): 63-83.
- Li., Q.S., Fang, J.Q., Jeary, A.P. and C.K. Wong (1998) "Full Scale Measurements of Wind Effects on Tall Buildings," *Journal of Wind Engineering and Industrial Aerodynamics*, **74-76**: 741-750.
- Little, J.D. (1991) *The Response of a Tall Building to Wind Loading*. Thesis, University of London.
- Little, J.D. (1995) "An Assessment of Some of the Different Methods for Estimating Damping from Full-Scale Testing," *Journal of Wind Engineering and Industrial Aerodynamics*, **57**: 179-189.
- Liu, P.C. (1994) "Wavelet Spectrum Analysis and Ocean Wind Waves" in Foufoula-Georgiou, E. and P. Kumar, Eds., *Wavelets in Geophysics*. Academic Press, San Diego: 151-166.
- Lockyer, R. (2000) "A Sonic Anemometer for General Meteorology," *Vaisala News*, **152**: 6-8.
- Lovse, J.W., Teskey, W.F., Lachapelle, G. and M.E. Cannon (1995) "Dynamic Deformation Monitoring of Tall Structure Using GPS Technology," *Journal of Surveying Engineering*, **121**(1): 35-40.
- Mahmoud, M., Abe, M. and Y. Fujino (2001) "Analysis of Suspension Bridge by Ambient Vibration Measurement Using Time Domain Methods and Its Application to Health Monitoring," In *Proceedings of International Modal Analysis Conference XIX*, SEM, Orlando, FL, Feb 5-8: CD-ROM.

- Mallat, S. (1998) *A Wavelet Tour of Signal Processing*. Academic Press, San Diego.
- Meyers, S.D., Kelly, B.G. and J.J. O'Brien (1993) "An Introduction to Wavelet Analysis in Oceanography and Meteorology: With Application to the Dispersion of Yanai Waves," *Monthly Weather Review*, **121**: 2858-2866.
- Miyashita, K., Itoh, M., Fujii, K., Yamashita, J., and T. Takahashi (1998) "Full-Scale Measurements of Wind-Induced Responses on the Hamamatsu ACT Tower," *Journal of Wind Engineering and Industrial Aerodynamics*, **74-76**: 943-953.
- Montpellier, P.R. (1996) *The Maximum Likelihood Method of Estimating Dynamic Properties of Structures*. Thesis, University of Western Ontario, London, Ontario: 63-97.
- Montpellier, P., Isyumov, N., and D. Morrish (1998) "Reliable Damping Estimates for Full-Scale Buildings and Structures," In *Proceedings of Structural Engineering World Congress*, San Francisco, July 19-23: CD-ROM T193-3.
- Nakamura, S. (2000) "GPS Measurements of Wind-Induced Suspension Bridge Girder Displacements," *Journal of Structural Engineering*, **126**(12): 1413-1419.
- Ohkuma, T., Marukawa, H., Niihori, Y., and N. Kato (1991) "Full-Scale Measurement of Wind Pressures and Response Accelerations of a High-Rise Building," *Journal of Wind Engineering and Industrial Aerodynamics*, **38**: 185-186.
- Ohkuma, T. (1996) *Japanese Experience with Motions of Tall Buildings*. Report to Committee 36 Motion Perception and Tolerance of CTBUH, February 29.
- Peng, Z., Chu, F. and Y. He (2002) "Vibration Signal Analysis and Feature Extraction Based on Reassigned Wavelet Scalogram," *Journal of Sound and Vibration*, **253**(5): 1087-1100.
- Perrier, V., Philipovitch, T. and C. Basdevant (1995) "Wavelet Spectra Compared to Fourier Spectra," *Journal of Mathematical Physics*, **36**(3): 1506-1519.
- Politis, D.N. (1998) "Computer-Intensive Methods in Statistical Analysis," *IEEE Signal Processing Magazine*, January: 39-76.
- Porterfield, M.L. and N.P. Jones (1999) "Full-Scale Measurements on a Low-Rise Structure," In *Proceedings of the 10th International Conference on Wind Engineering*, Copenhagen, June, **3**: 1839-1846.
- Powers, E.J., Park, S.I., Mehta, S. and E.J. Yi (1997) "Higher-Order Statistics and Extreme Waves," In *IEEE Signal Processing Workshop on Higher Order Statistics*, Alberta, Canada, July 21-23: 98-102.
- Priestly, M.B. (1988) *Non-Linear and Non-Stationary Time Series Analysis*. Academic Press, New York.

- Raggett, J.D. (1975) "Estimating Damping of Real Structures," *Journal of Structures Division*, ASCE, **101**(ST9): 1823-1835.
- Rihaczek, A. (1966) "Hilbert Transforms and the Complex Representation of Signals," *Proceedings of IEEE*, **54**, 434-435.
- Ristic, B. and B. Boashash (1996) "On Estimation of Instantaneous Bandwidth," In *Proceedings of IEEE-SP International Symposium on Time-Frequency and Time Scale Analysis*, Paris, June 18-21: 197-200.
- Roberson, A.N., Park, K.C., and K.F. Alvin (1998a) "Extraction of Impulse Response Data via Wavelet Transform for Structural System Identification," *Transactions of the ASME*, **120**: 252-260.
- Roberson, A.N., Park, K.C., and K.F. Alvin (1998b) "Identification of Structural Dynamics Models Using Wavelet-Generated Impulse Response Data," *Transactions of the ASME*, **120**: 261-266.
- Roberts, G.W., Dodson, A.H. and V. Ashkenazi (1999) "Twist & Deflect: Monitoring Motion of the Humber Bridge," *GPS World*, **10**(10): 24-35.
- Ruzzene, M., Fasana, A., Garibalidi, L. and B. Piombo (1997) "Natural Frequencies and Dampings Identification Using Wavelet Transform: Application to Real Data," *Mechanical Systems and Signal Processing*, **11**(2): 207-218.
- Schwartz, M., Bennett, W.R. and S. Stein (1966) *Communications Systems and Techniques*. McGraw-Hill, New York.
- Seeber, G. (1993) *Satellite Geodesy – Foundations, Methods and Applications*. Walter de Gruyter & Co., Berlin: 209-355.
- Seybert A.F. (1981) "Estimation of Damping from Response Spectra," *Journal of Sound and Vibration*, **75**(2): 199-206.
- Shin, Y.J., Powers, E.J. and E.J. Yi (1999) "Comparison of Time-Frequency Representations of Random Wave Elevation Data," In *Proceedings of 9th International Offshore and Polar Engineering Conference*, Brest, France, May 30-June 4: 34-40.
- Simiu, E. and R.H. Scanlan (1996) *Wind Effects on Structures*. 3rd Edn., Wiley & Sons, New York.
- Singh, S.K., Mena, E. and R. Castro (1989) "Some Aspects of Source Characteristics of the 19 September 1985 Michoacan Earthquake and Ground Motion Amplification in and near Mexico City from Strong Motion Data (Abstract)", In V.V. Bertero, Ed., *Lessons Learned from the Mexico City Earthquake*, EERI, El Cerrito, CA: 39-40.
- Slepian, D., Landau, H., and H. Pollak (1961) "Prolate Spheroidal with Functions – Fourier analysis and uncertainty, I, II and III," *Systems Technology Journal*, **40**(1): 43-84.

- Solari, G. and A. Kareem (1998) "On the Formulation of ASCE 7-95 Gust Effect Factor," *Journal of Wind Engineering and Industrial Aerodynamics*, **77-78**: 673-684.
- Spanos, P.D. and B.A. Zeldin (1996) "Efficient Iterative ARMA Approximation of Multivariate Random Processes for Structural Dynamics Applications," *Earthquake Engineering and Structural Dynamics*, **25**: 497-507.
- Spanos, P.D. and B.A. Zeldin (1998) "Generalized Random Decrement Method for Analysis of Vibration Data," *Transactions of the ASME*, **120**: 806-813.
- Staszewski, W.J. (1997) "Identification of Damping in MDOF Systems Using Time-Scale Decomposition," *Journal of Sound and Vibration*, **203**(2): 283-305.
- Staszewski, W.J. (1998) "Identification of Non-Linear Systems Using Multi-Scale Ridges and Skeletons of the Wavelet Transform," *Journal of Sound and Vibration*, **214**(4): 639-658.
- Staszewski, W.J. and J. Giacomini (1997) "Application of the Wavelet Based FRFs to the Analysis of Nonstationary Vehicle Data," In *Proceedings of 15th International Modal Analysis Conference*: 425-431.
- Stein, R.S., Hudnut, K.W., Satalich, J. and K.M. Hodgekinson (1997) "Monitoring Seismic Damage to Bridges and Highways with GPS: Insights from the 1994 Northridge Earthquake," In *Proceedings of National Seismic Conference on Bridges and Highways: Progress in Research and Practice*, Sacramento, CA, July 8-11: 347-360.
- Stoker, J.J. (1966) *Nonlinear Vibrations in Mechanical and Electrical Systems*, 2nd Edn., Interscience Publishers (Division of Wiley & Sons), New York: 116-117.
- Surry, D. (1991) "Pressure Measurements on the Texas Tech Building: Wind Tunnel Measurements and Comparisons with Full Scale," *Journal of Wind Engineering and Industrial Aerodynamics*, **38**: 235-247.
- Tamura, Y., Sasaki, A., Sato, T., and R. Kousaka (1992) "Evaluation of Damping Ratios of Buildings During Gusty Wind Using the Random Decrement Technique," In *Proceedings of 12th Wind Engineering Symposium*.
- Tamura, Y., Shimada, K. and H. Kazuki (1993) "Wind Response of a Tower (Typhoon Observation at the Nagasaki Huis Ten Bosch Domtoren)," *Journal of Wind Engineering and Industrial Aerodynamics*, **50**: 309-318.
- Tamura, Y., Yamada, M., and H. Yokota (1994) "Estimation of Structural Damping of Buildings," In *Proceedings of ASCE Structures Congress and IASS International Symposium*, Atlanta, **2**: 1012-1017.
- Tamura, Y., Shimada, K., Sasaki, A., Kohsaka, R., and K. Fuji (1995) "Variation of Structural Damping Ratios and Natural Frequencies of Tall Buildings During Strong

Winds,” In *Proceedings of the 9th International Conference on Wind Engineering*, New Delhi.

Tamura, Y. (chairman), Arakawa, T., Morita, K., Ono, J., Sasaki, A., Satake, N. and K. Suda (1996) *Database of Dynamic Properties of Buildings and Structures in Japan*. Report by Research Committee on Damping Evaluation, Architectural Institute of Japan.

Tamura, Y. and S.-Y. Suganuma (1996) “Evaluation of Amplitude-Dependent Damping and Natural Frequency of Buildings During Strong Winds,” *Journal of Wind Engineering and Industrial Aerodynamics*, **59**(2,3): 115-130.

Tamura, Y. (1997) “Japanese Damping Database,” In *Proceedings of Structures Congress XV*, ASCE, **2**: 1064-1067.

Tamura, Y. (1998) “Damping in Buildings in Japan,” *Proceedings of Structural Engineering World Congress*, San Francisco, July 19-23: CD-ROM T193-2.

Tamura, Y., Matsui, M., Pagnini, L.-C. and A. Yoshida (2001) “Measurement of Wind-Induced Response of Buildings Using RTK-GPS,” In *Proceedings of 5th Asia-Pacific Conference on Wind Engineering*, Kyoto, Oct. 21-24.

Tamura, Y. (2002) “Dynamic Monitoring Response of Structures Using GPS,” In *Proceedings of ASCE Structures Congress 2002*, Denver, April 4-6.

Taoka, G.T., Hogan, M., Khan, F. and R.H. Scanlan (1975) “Ambient Response Analysis of Some Tall Structures,” *Journal of Structural Engineering*, **101**(ST1): 49-65.

Teague, E.H., How, J.P., Lawson, L.G. and B.W. Parkinson (1995) “GPS as a Structural Deformation Sensor,” In *Proceedings of AIAA Guidance, Navigation and Control Conference*, Baltimore, August 7-10: 787-795.

Tieleman, H.W., Surry, D. and K.C. Mehta (1996) “Full/Model Scale Comparison of Surface Pressures on the Texas Tech Experimental Building,” *Journal of Wind Engineering and Industrial Aerodynamics*, **61**: 1-23.

Toriumi, R., Katsuchi, H. and N. Furuya (2000) “A Study on Spatial Correlation of Natural Wind,” *Journal of Wind Engineering and Industrial Aerodynamics*, **87**: 203-216.

Torrence, C. and G.P. Compo (1998) “A Practical Guide to Wavelet Analysis,” *Bulletin of the American Meteorological Society*, **79**(1): 61-78.

Tranquilla, J.M., Carr, J.P. and H.M. Al-Rizzo (1994) “Analysis of a Choke Ring Groundplane for Multipath Control in Global Positioning System (GPS) Applications,” *IEEE Transactions on Antennas and Propagation*, **42**(7): 905-911.

Trifunac, M.D. (1972) “Comparisons Between Ambient and Forced Vibration,” *Earthquake Engineering and Structural Dynamics*, **1**: 133-150.

- Turner, L. (2002) "What's Shaking? Earthquake Trials Test Networked RTK," *GPS World*, **13**(4): 16-22.
- Vandermeulen, R., Kijewski, T. and A. Kareem (2000) "Bootstrap Method for Estimation of Spectral Bandwidth with Limited Observations," In *Proceedings of Probabilistic Mechanics Conference 2000*, University of Notre Dame, July: CD-ROM.
- Vandiver, J.K., Dunwoody, A.B., Campbell, R.B. and M.F. Cook (1982) "A Mathematical Basis for Random Decrement Vibration Signature Analysis Technique," *Journal of Mechanical Design*, **104**: 307-313.
- Van Nee, R. D. J. (1995) *Multipath and Multi-Transmitter Interference in Spread-Spectrum Communication and Navigation Systems*. Thesis, Delft University of Technology, Delft University Press.
- Ville, J. (1948) "Theorie et Application de la Notion de Signal Analytical," *Cables et Transmissions*, **2A**(1): 61-74 [Translated into English by I. Selin, RAND Corp. Report T-92, Santa Monica, CA (August 1958)].
- Wang, D. and A. Haldar (1997) "System Identification with Limited Observations and Without Input," *Journal of Engineering Mechanics*, **123**(5): 504-511.
- Wang, W.J. (2001) "Wavelets for Detecting Mechanical Faults with High Sensitivity," *Mechanical Systems and Signal Processing*, **15**(4): 685-696.
- Wigner, E.P. (1932) "On the Quantum Corrections for the Thermodynamic Equilibrium," *Physical Review*, **40**: 749-759.
- Wong, K.-Y., Man, K.-L. and Chan, W.-Y. (2001) "Monitoring Hong Kong's Bridges Real-Time Kinematic Spans the Gap," *GPS World*, **12**(7).
- Woodhouse, J. (1999) "Linear Damping Models for Structural Vibration," *Journal of Sound and Vibration*, **215**(5): 547-569.
- Wooh, S.-C. and K. Veroy (2001) "Spectrotemporal Analysis of Guided-Wave Pulse-Echo Signals: Part 1. Dispersive Systems," *Experimental Mechanics*, **41**(4): 332-342.
- Wu, F., Sarkar, P.P. and K.C. Mehta (1999) "Understanding the Conical Vortex Flow in Roofs," In *Proceedings of 10th International Conference on Wind Engineering*, Copenhagen, June, **3**: 1867-1873.
- Xu, Y.L. and S. Zhan (2001) "Field Measurements of Di Wang Tower During Typhoon York," *Journal of Wind Engineering and Industrial Aerodynamics*, **89**: 73-93.
- Xu, L., Guo, J.J. and J.J. Jiang (2002) "Time-Frequency Analysis of a Suspension Bridge Based on GPS," *Journal of Sound and Vibration*, **245**(1): 105-116.

- Yalla, S.K. and A. Kareem (2001) "Beat Phenomenon in Combined Structure-Liquid Damper Systems," *Engineering Structures*, **23**: 622-630.
- Yamamoto, M., Higashino, M., Toyama, K. and S. Aizawa (1998) "Five Years of Wind and Earthquake Observation Results from a Building with Active Mass Dampers," In *Proceedings of Structural Engineering World Congress*, San Francisco, July 19-23: CD-ROM T198-2.
- Yang, J.C.S., Dagalakis, N.G., Everstine, G.C., and Y.F. Wang (1983) "Measurement of Structural Damping Using the Random Decrement Technique," *Shock and Vibration Bulletin*, **53**(4): 63-71.
- Yang, J.N., Kagoo, P.K. and Y. Lei (2000) "Parametric Identification of Tall Buildings Using Ambient Wind Vibration Data," In *ASCE Specialty Conference on Probabilistic Mechanics and Structural Reliability*, University of Notre Dame, July 24-26: CD-ROM PMC2000-076.
- Yokoo, Y. and H. Akiyama (1972) "Lateral Vibration and Damping Due to Wind and Earthquake Effects," In *Proceedings of International Conference On Planning and Design of Tall Buildings*, II-17, ASCE, New York.
- Zheng, H., Li, Z. and X. Chen (2002) "Gear Fault Diagnosis Based on Continuous Wavelet Transform," *Mechanical Systems and Signal Processing*, **16**(2-3): 447-457.
- Zhou, Y., Kijewski, T. and A. Kareem (2002) "Alongwind Load Effects on Tall Buildings: A Comparative Study of Major International Codes and Standards," *Journal of Structural Engineering*, ASCE, **128**(6): 788-796.
- Zhou, Y., Kijewski, T. and A. Kareem (2003) "Aerodynamic Loads on Tall Buildings: An Interactive Database," *Journal of Structural Engineering*, ASCE, **129**(3).
- Zoubir, A.M., Iskander, D.R., Ristic, B., and B. Boashash (1994) "Bootstrapping Confidence Bands for the Instantaneous Frequency," *Advanced Signal Processing Algorithms, Architectures and Implementations*, **2296**: 176-190.